INVESTIGATION OF TROPOSPHERIC AEROSOLS BY MULTIWAVELENGTH MIE-RAMAN LIDAR

by

Mehmet Fatih Hüseyinoğlu

BA in Philosophy, Boğaziçi University, 1995

MSc in Environmental Sciences, Boğaziçi University, 1999

Submitted to the Institute of Environmental Sciences in partial fulfillment of

the requirements for the degree of

Doctor

of

Philosophy

Boğaziçi University

2010

INVESTIGATION OF TROPOSPHERIC AEROSOLS
BY MULTIWAVELENGTH MIE-RAMAN LIDAR

APPROVED BY:

Prof. Dr. Miray Bekbölet . . . . . .

(Thesis Co-Supervisor)

Prof. Dr. Kerim Allahverdi . . . . . .

(Thesis Co-Supervisor)

Prof. Dr. Barış Mater . . . . . .

Prof. Dr. Igor Veselovskii . . . . . .

Prof. Dr. Orhan Yenigün . . . . . .

DATE OF APPROVAL 03.12.2010

ACKNOWLEDGEMENTS

I would like to thank my co-advisors, Prof. Dr. Miray Bekbölet and Prof. Dr. Kerim Allahverdi for their endless support and help through the thesis; my jury members, Prof Dr. Orhan Yenigün, Prof. Dr. Barış Mater and Prof. Dr. Igor Veselovskii; TUBITAK MRC Materials Institute Director Assoc. Prof. Dr. Tarık Baykara, Deputy Directors Assoc. Prof. Dr. Emel Musluoğlu and Assoc. Prof. Dr. Volkan Günay for their encouragement and support for the last 3 years which covers the most important period of this thesis; my friends at Physics Instrumentation Center, Russian Academy of Sciences, Troitsk, Moscow Region, particularly Vadim, Mikhail and especially I. Alexandrovich for their hospitality and great help during my visits; my co-workers Dr. Zehra Allahverdi, Alper Seçgin and Nurullah Ağca for their help during the development, installation and measurements of lidar; my mother Muazzez Hüseyinoğlu, my father Sedat Hüseyinoğlu, my brother M. Kemal Hüseyinoğlu and my sister Ş. Hilal Hüseyinoğlu for supporting and encouraging me not only during the thesis, but all my life. I would like to specially thank my wife Valeriya for her support, kindness, patience, organizing my life and for the various loads of translations from Russian, English, Turkish to English and Turkish. Finally, I like to specially thank the State Planning Committee (DPT) for making this whole thing real.

INVESTIGATION OF TROPOSPHERIC AEROSOLS BY MULTIWAVELENGTH MIE-RAMAN LIDAR

Atmospheric aerosols affect the Earth’s radiation balance by absorbing or scattering the fluxes of solar or terrestrial radiation. This change leads to radiative forcing of the atmosphere. Scattering of the solar radiation by aerosols tends to cool the atmosphere and this is called the "aerosol direct effect". Aerosols modify the cloud properties effecting rainfall patterns and this is called the "aerosol indirect effect". Thus, aerosols cause global cooling. Aerosols also have negative effect on public health; inhaling aerosols results with chemicals entering the human body and deposited into lungs causing lung cancer, asthma, premature death and cardiovascular problems. Lidar is the acronym of "light detection and ranging", with a laser transmitter and a telescope receiver supplied with electronic and optical instruments. Aerosol optical and physical parameters and important atmospheric data about the clouds and water vapor can be calculated by analyzing aerosol extinction and backscattering coefficients which can be obtained by the remote sensing technology of lidars.

For the purpose of investigating the aerosols, a Multiwavelength Mie-Raman lidar has been designed, developed and operated between 2009 and 2010. By this lidar, extinction and backscattering at multiple wavelengths were measured and converted to microphysical properties of aerosols by mathematical methods. The retrieved data contains size distribution, effective radius, volume, surface area and number density, complex refractive index, volume and particle polarization, water vapor mixing ratio. The ash plums from the Iceland volcanic eruption were detected and characterized.

TROPOSFER AEROSOLLERİNİN ÇOKDALGABOYLU MIE-RAMAN LİDARI İLE İNCELENMESİ

Atmosfer aerosolleri, güneş ve karasal radyasyonun akışını soğurarak veya saçarak Dünya'nın ışınım dangesini değiştirmektedir. Bu değişiklik atmosfer ışınımsal zorlamasına yol açar. Aerosollerden güneş radyasyonunun saçılması, atmosferin soğuması eğilimi göstermektedir ve bu fenomen 'aerosol doğrudan etkisi' olarak bilinmektedir. Aerosollar, bulut özelliklerini değiştirerek yağış şekillerini değiştirmekte ve bu da 'aerosol dolaylı etkisi' olarak bilinmektedir. Bu yüzden aerosoller küresel soğumaya sebep olmaktadır. Ayrıca, aerosollar insan sağlığını olumsuz etkilemektedir; aerosollerin teneffüs edilmesi, vücuda kimyasalların akciğer yoluyla girmesi ve dolayısıyla akciğer kanseri, astım, erken ölüm ve kardiyovasküler sorunlar gibi komplikasyonlara neden olmaktadır. Lidar "ışıkla tespit ve mesafelendirme" kelimelerinin İngilizcesinden türetilmiş bir akronimdir ve bir lazer vericisi, bir teleskop alıcı ve çeşitli yardımcı elektronik ve optik aygıtlardan oluşmaktadır. Lidar uzaktan algılama teknolojisi yardımı ile elde edilen ışın azalımı ve geri saçılma katsayılarının analizi ile aerosollerin optik ve fiziksel özellikleri, bulutlar ve atmosferdeki su buharı hakkında önemli bilgiler hesaplanabilir hale gelmektedir.

Aerosollerin incelenmesi amacı ile, bir çokdalgaboylu Mie-Raman lidarı, tasarlanmış, geliştirilmiş ve 2009 ile 2010 arasında ölçümler alınmıştır. Bu lidar ile çeşitli dalgaboylarındaki ışıklardan elde edilen ışın azalımı ve geri saçılımı, matematiksel yöntemler ile aerosol mikrofiziksel özelliklerine dönüştürülmüştür. Elde edilen bilgiler, parçacık boyut dağılımı, etkin parçacık çapı, hacim, alan ve sayı yoğunluğu, kompleks kırılma indisi, hacim ve parçacık polarizasyonu ve su buharı karışım oranı gibi özellikleri içermektedir. İzlanda'daki volkanik patlamanın kül tozları tespit edilmiş ve karakterize edilmiştir.

TABLE OF CONTENTS

LIST OF FIGURES

LIST OF SYMBOLS

Symbol	Explanation	Units used
c	Speed of light	(ms^{-1})
H	Height	(m, km)
m	Complex refractive index	(-)
m_R	Real part of complex refractive index	(-)
m_i	Imaginary part of complex refractive index	(-)
N	Number density	(cm^{-3})
P	Power	(W)
R_{eff}	Effective radius	(μm)
R_{mean}	Mean radius	(μm)
S	Surface area density	($\mu m^2 cm^{-3}$)
V	Volume density	($\mu m^3 cm^{-3}$)
z	Distance	(m, km)
z_{ref}	Reference distance	(m, km)
α	Extinction coefficient	(km^{-1})
β	Backscattering coefficient	($km^{-1}sr^{-1}$)
λ	Wavelength	(nm, μm)

LIST OF ABBREVIATIONS

Abbreviation	Explanation
3-D	Three dimensional
APD	Avalanche photodiode
ATD	Analog-to-digital
CCN	Cloud Condensation Nuclei
CDNC	Cloud droplet number concentration
DIAL	Differential Absorption Lidar
DMS	Dimethyl sulfide
EC	Elemental carbon
EPA	Environmental Protection Agency (USA)
FOV	Field of view
HSRL	High spectral resolution lidar
IPCC	International Panel on Climate Change
Lidar	Light detection and ranging
MW	Multiwavelength
nss-SO_4^{2-}	Non-sea-salt sulphates
OC	Organic carbon
PBA	Primary biogenic aerosol
PBL	Planetary Boundary Layer
PCB	Polychlorinated biphenyl
PM_1	Particulate Matter less than 1 μm diameter
$PM_{2.5}$	Particulate Matter less than 2.5 μm diameter
PM_{10}	Particulate Matter less than 10 μm diameter
PM_{10}-$PM_{2.5}$	Particulate Matter with diameter between 2.5 - 10 μm
PMF	Positive matrix factorization
PSD	Particle Size Distribution
SO_2	Sulphur dioxide
TSP	Total suspended particle
UFP	Ultrafine particle (diameter less than 100 nm)

UV-B	Ultraviolet radiation between 290 - 320nm
VOC	Volatile organic compunds
WSOC	Water soluble organic carbon

1. INTRODUCTION

Aerosols are described as "small droplets or particles suspended in the atmosphere, typically containing sulfur. They are usually emitted naturally (e.g. in volcanic eruptions) and as the result of anthropogenic (human) activities such as burning fossil fuels". In the International Panel on Climate Change (IPCC) Glossary, they are described as "a collection of airborne solid or liquid particles, with a typical size between 0.01 and 10 μm and residing in the atmosphere for at least several hours. Aerosols may be of either natural or anthropogenic origin. Aerosols may influence climate in two ways: directly through scattering and absorbing radiation, and indirectly through acting as condensation nuclei for cloud formation or modifying the optical properties and lifetime of clouds" (Houghton et al., 2001).

Aerosols have various effects on the earth on different levels. Locally, they contribute to air pollution by reducing the airspace visibility. Moreover, they are a hazard to human health, such that while larger aerosols are generally filtered by the various mechanisms in the nose and throat, small aerosols can reach the bronchia and alveoli in the lungs to cause diseases like lung cancer and asthma. They might also be the cause of cardiovascular diseases and premature deaths. Aerosols may also act as carriers of various viruses or bacteria which can worsen the effects on human health. On the regional scale, aerosols are contributors to acid deposition, affecting forests and lakes. They also contribute to eutrophication, by settling on large amounts to certain regions, thus affecting water quality. They might as well influence photochemistry and ozone production. On the global scale, aerosols reflect solar light and hence influence climatic change (Solomon et al., 2007). Even though the effects of aerosols on the world are countless and highly variable on several levels, the main direction of the investigation throughout this thesis will be towards the radiative properties of aerosols.

Aerosols are described as suspended in the atmosphere, but they are also susceptible to atmospheric movements like winds, gravitational movements and

precipitations, and since they are particles with a volume and mass, they absorp or scatter the unique incoming energy of the Earth, the solar radiation. Eventhough they are considerably and relatively small in size, they measurably effect the global energy from solar radiation. These phenomena are named as aerosol direct and indirect effects in the scientific literature. The direct effect is basically the absorption and reflection of the incoming solar radiation by the particles both in movement and in suspense. An increase in the number of aerosols means the increase of the reflectivity of the atmophere and the cloud albedo, which results with atmospheric and surface cooling. However, the indirect effects, which are probably trickier to comprehend and measure, can only be understood through a continous remote sensing database. Aerosol indirect effect is simply described as the effects of aerosols on cloud microphysical properties. First, aerosols are responsibles and servers for cloud formation, acting as Cloud Condensation Nuclei (CCN). Water vapor evoporating from the surface of the Earth, attaches itself onto a surface of a hydrophyllic aerosol and increases radius of the aerosol. More water vapor attaching to more hydrophyllic aerosols, form the cloud. When the cloud is saturated with more water that it can carry, rain starts to form.

Therefore a better understanding of the aerosol microphysical parameters and their spatial and temporal dynamics is also very crucial for precipitation patterns, and henceforth, this phenomenon is called the “Aerosol First Indirect Effect”. When more aerosol acting as CCN are present, for a certain amount of water vapor, the water vapor is shared among a larger number of CCN, and therefore the droplets that form are smaller. A consequence of this can be a decreased likelihood of precipitation, which implies longer cloud lifetimes and this is called as the “Aerosol Second Indirect Effect”.

Since subjects like atmospheric and surface cooling, alterations of precipitation regimes and cloud albedo change are mentioned, global climate change is the issue and must be taken very well into consideration in this dissertation, especially in the introduction section. The main difficulty in the measurement of aerosol indirect effect is the fact that aerosols, unlike greenhouse gases that become well-mixed in the atmosphere, are not uniformly distributed and their concentrations change quickly with time. Also some aerosols are more effective CCN than others, depending on their hygroscopicity. In fact,

not all aeosols get activated into cloud droplets, activation being a process which depends on both the level of supersaturation and the aerosol hygroscopicity (Solomon et al., 2007; Russo, 2007).

Although climate response is followed by radiative forcing, it is generally not the case that it can be calculated directly, because so many other phenomena are involved in between, because of the uncertainity of how climate responses to the perturbations (Solomon et al., 2007). Figure 1.1 illustrates the pathway from the emergence of emissions to climate response and the phenomena involved in between.

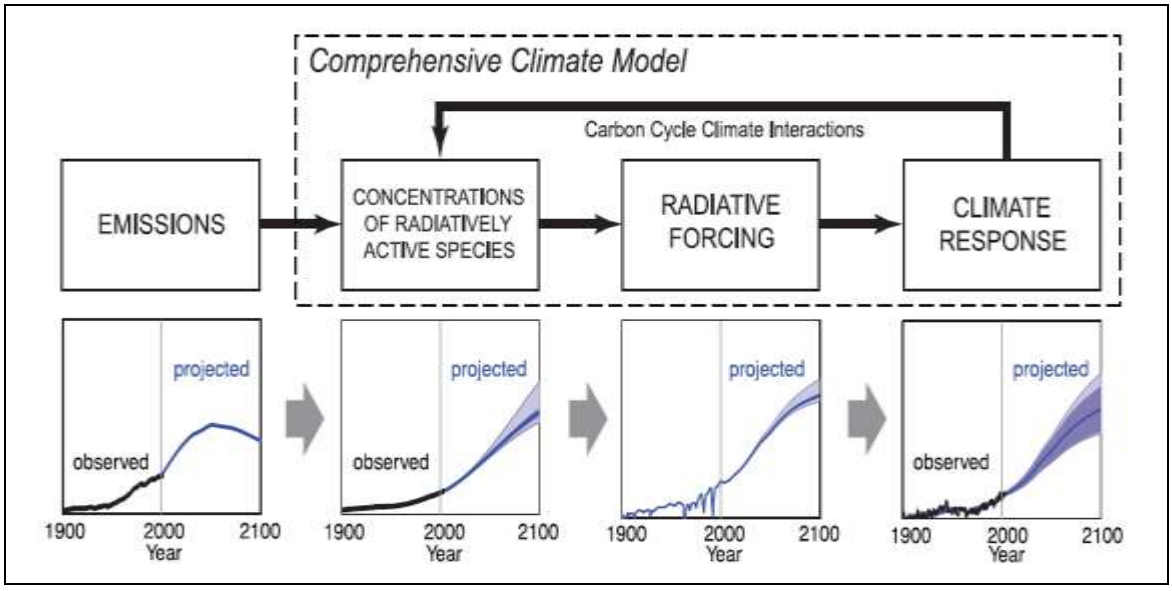

Figure 1.1. The comprehensive climate model (Solomon et al., 2007).

There have been observable increase in the amounts of emissions and concentrations of radiatively active species among these emissions. Especially radiatively active species like carbonaceous aerosols and desert dust cause radiative forcing, and this is followed by the climate response, which in return effects the concentrations of radiatively active species through carbon cycle climate interactions. Figure 1.1 illustrates this model within the framework of a comprehensive climate model (Solomon et al., 2007)

Global climate change has been a very popular subject during the last couple decades both in the public view and in the related fields of science such as climatology, meteorology and atmospheric science. Global warming has been a hot issue and although the list can be populated to a greater length, to show the extent, it can be stated that the ex-vice president of the United States of America, Al Gore, has won the Academy Awards for Best Documentary Feature in 2006 with "An Inconvenient Truth" which is a full-length documentary film about the extent and emergency of the global warming, adapted from Al Gore's book with the same name and presented by him in the picture. He was also the Nobel Peace Prize leurate in 2007 "for his efforts to build up and disseminate greater knowledge about man-made climate change, and to lay the foundations for the measures that are needed to counteract such change" (Nobel Foundation Official web site, 2008). On the other hand, although being unable to find significant support from the scientific community, global cooling is also mentioned worldwide.

Nevertheless, one thing which is valid without question, is there is an observable and demonstratable change in Global climate. There is great concern about whether and to what extent, Global changes in weather and climate are due to human-related factors. However, measuring this is not an easy task which can be achieved by a single dicipline, but rather by a multi-disciplinary view. It was recorded that 11 among the last 14 years were the highest Global temperatures as far as the global records were held since the emergence of the Industrial Revolution in the 19th century, and Figure 1.2 illustrates the global differences in surface temperatures since 1901 (Kiehl and Trenbeth, 1997; Solomon et al, 2007).

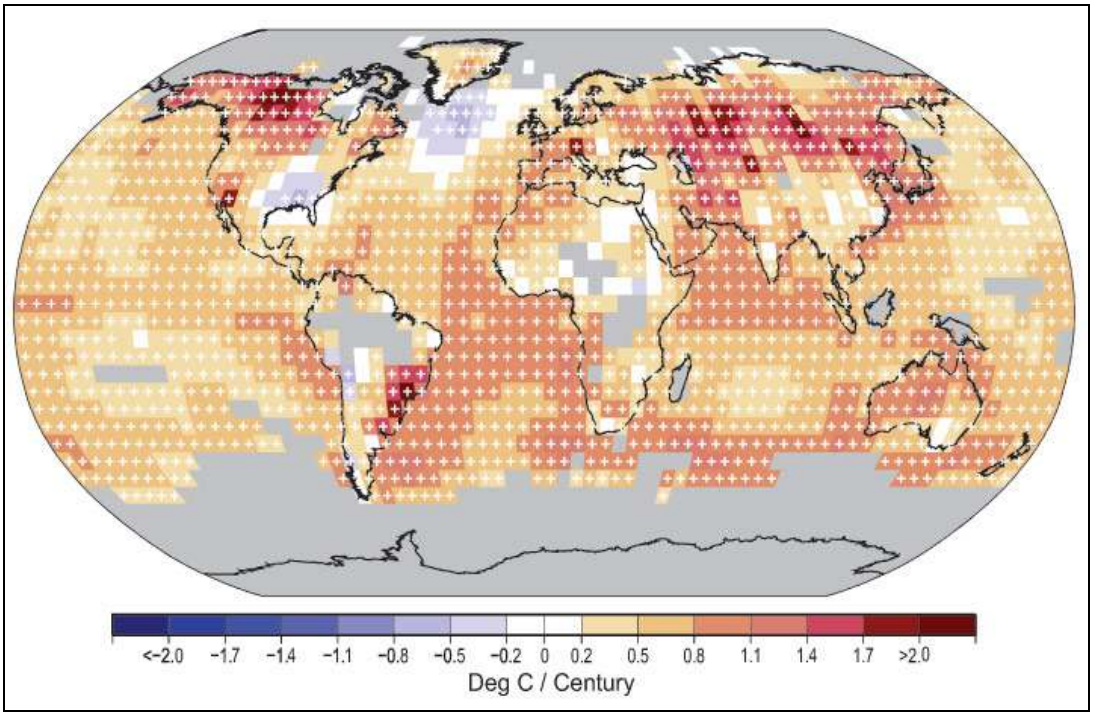

Figure 1.2. Linear trend of annual temperatures for 1901-2005.

According to the report from the Intergovernmental Panel for Climate Change (IPCC) Working Group I, the seven of the last 12 years (1995-2006) are among the warmest years in the instrumental record of global surface temperatures since 1850. From the reports, it is self-evident that there is a definite warming of the surface air. Local heat sources from the urban sites have a negligible effect for the increase in the values, therefore a broad and better comprehension of the whole climate system is necessary to be able to understand the changes within it. Figure 1.2 illustrates the surface temperature increases which are strikingly marked with red. Areas in grey have insufficient data to produce reliable trends. Trends significant at the 5% level are indicated by white + marks (Solomon et al., 2007).

Aerosols, which were investigated in this study, are one of the uncertainities of the factors responsible for the Global climate change. Atmosphere is definetely one of the most difficult components of the Earth system to investigate and measure with in situ sampling, remote-sensing, modelling and other methods. If there is an observable global

warming, there should be a global atmospheric warming and vice versa. But complex interactions of physical basis in the atmosphere are not generally so easy to conceive and the effects are usually not followed by a sudden observable subsequent response, therefore this study deals with what is observable in a certain amount of period rather than a global, intemporal and interdiciplinary comparable integration of data.

With the help of the proposed lidar technology, which will be explained in detail within later chapters, it is possible to retrieve the microphysical parameters of aerosols. For this reason, through this brief introduction, the types and sources of the aerosols present in the lower atmosphere, as well as present lidar networks in the world will be mentioned. The physical basis for the study of the effects of aerosols on the atmosphere, scattering theories related with aerosols and aerosol effects on the Global radiative forcing which are direct and indirect, will be introduced in this chapter. The aerosol microphysical parameters will be introduced in this chapter, but the retrieval methods will be described in Methodology and Results.

1.1. Aerosol Sources and Effects on the Atmosphere

Aerosols are one of the most important parts of the atmosphere. Aerosols act as cloud condensation nuclei, without aerosols, the formation of clouds and therefore precipitation patterns would be highly affected. In this chapter aerosols will be briefly described. Their sources can be either natural or anthropogenic, the latter of which is about 10% of the total, will also be discussed here. Representative pictures of aerosol types can be found in the Appendix A. The descriptions of their microphysical properties such as mean radius, effective radius, volume, surface area and number densities, complex refractive index and various related phenomena such as volume and particle polarization by aerosols, particle size distribution (PSD), and water vapor mixing ratio will be briefly mentioned.

The origin of aerosols is the most convenient approach about their classification and this is how it is done in this chapter, although naturally, they are found as a mixture from different sources in the atmosphere. Considering the complex chemical formation

processes and atmospherical transport mechanisms, it will also be a more convenient approach to accept the origins (which are either natural or anthropogenic) of the aerosols for classifying them.

The concept of a "source strength" is much more difficult to define for aerosols than for most greenhouse gases. First, many aerosol species (e.g., sulphates and secondary organics) are not directly emitted, but rather formed in the atmosphere from precursors in the gaseous form. Second, some aerosol types (e.g., from soil dust and sea salt) consist of particles whose properties, such as size distribution and refractive index, have wide variations in ranges. Since the atmospheric lifetimes and radiative effects of particles strongly depend on these properties, it makes little sense to provide a single value for the source strength of such aerosols. Third, aerosol species often combine to form mixed particles with optical properties and atmospheric lifetimes, different from those of their components. Finally, clouds effect aerosols in a very complex way by scavenging aerosols, by adding mass through liquid phase chemistry, and through the formation of new aerosol particles in and near clouds (Dubovik et al., 2001; Solomon et al., 2007).

1.1.1. Soil Dust

Soil dust is a general term to explain the dust which is elevated either naturally or anthropogenically from the vegetationally cleared parts of Earth. It is mainly originated from the large deserts of the World, like Sahara and other large deserts such as Gobi and Taklimakan, but Saharan dust is so big of a contributor that soil dust is usually referred as Sahara dust in scientific literature. Dust originating from the great deserts of the continents of Africa and Asia, consists primarily of clay soil minerals such as illite, quartz, kaolinite, chlorite, microcline, plagioclase, and calcite, all of which may undergo chemical change during aerosol transport. Some elements (e.g. manganese, iron, scandium, cobalt) occur on African dust particles in concentrations similar to average crustal abundance, whereas other elements (e.g., mercury, selenium, lead) accumulate, via scavenging, at concentrations three orders of magnitude greater than mean crustal abundance (Garrison et al., 2003).

Soil dust is a major contributor to aerosol loading and optical thickness, especially in subtropical and tropical regions, travelling to long distances with atmospheric transportation before gravitation takes its course and settles it to various parts of the World, known to cause euthrophications, mineral deposits and other various phenomena. Estimates of its global source strength range from 1,000 to 5,000 Mt/yr (Duce et al., 1995) and 1000 to 2000 Mt/yr (Jickells et al., 2005) with very high spatial and temporal variability. Dust source regions are mainly deserts, dry lake beds, and semi-arid desert fringes, but also areas in drier regions where vegetation has been reduced naturally or soil surfaces have been disturbed by human activities, therefore it is sometimes difficult to interpret soil dust as anthropegenic or natural. As it was mentioned before, the major contributors of soil dust are the deserts, and Figure 1.3 illustrates the major sources of soil dust in the world.

Figure 1.3. The major sources of desert dust. (Source: U.S. National Center for Biotechnology Information web site, 2007).

Major dust sources are found in the desert regions of the Northern Hemisphere, while dust emissions in the Southern Hemisphere are relatively small since the land areas in the Southern Hemisphere is relatively small. In Figure 1.3, the greatest arid areas of the world are shown: 1) the Salton Sea, 2) Patagonia, 3) the Altipläno, 4) the Sahel region, 5) the Sahara Desert, 6) the Namibian desert lands, 7) the Indus Valley, 8) the Taklimakan

Desert, 9) the Gobi Desert, and 10) the Lake Eyre basin (USNCBI web site, 2007). Dust deflation occurs in a source region when the surface wind speed exceeds a threshold velocity. It is a function of various parameters like surface roughness elements, grain size, and soil moisture like crusting of soil surfaces and limitation of particle availability, which can reduce the dust release from the source region.

On the other hand, the disturbance of such surfaces by human activities can strongly enhance dust mobilisation. By earlier research it has been estimated that up to 50% of the current atmospheric dust load originates from disturbed soil surfaces, and should therefore be considered anthropogenic in origin (Tegen and Fung, 1995), but this estimate must be considered highly uncertain (Tegen et al., 2004). Furthermore, dust deflation can change in response to naturally occurring climate modes. For example, Saharan dust transport to Barbados increases during El Niño years (Prospero and Nees, 1986; Cane, 2005), and dust export to the Mediterranean and the North Atlantic is correlated with the North Atlantic Oscillation (Moulin et al., 1997; Ginoux et al., 2004). Analysis of dust storm records shows regions with both increases and decreases in dust storm frequency over the last several decades (Goudie and Middleton, 1992; Qian et al., 2001; McTainsh et al., 2005).

1.1.2. Sea Salt

Sea salt aerosols are generated by various physical processes, especially the bursting of entrained air bubbles during whitecap formation in marine waves resulting in a strong dependence on different factors like current and wind speed. This type of aerosol may be the dominant contributor to both light scattering and the formation of cloud nuclei in those regions of the marine atmosphere where wind speeds are high and/or other aerosol sources are weak because the main source of aerosols are basically the desert dust (Houghton et al., 2001). Sea salt particles are very efficient cloud condensation nuclei (CCN), and therefore characterization of their surface production is of major importance for aerosol indirect effects. Research, showed that in concentrations of one particle per litre, giant salt particles are able to modify strato-cumulus drizzle production and cloud albedo significantly (Feingold et al., 1999; O'Down et al., 2004).

Marine sourced aerosols account for the majority of the global natural aerosol flux and consequently, have an important impact on the Earth's radiative budget and biogeochemical cycling. Sea salt particles effect the radiative balance of the atmosphere by absorbing and scattering incoming solar radiation (direct effect) and by affecting the microphysical properties of clouds (indirect effect), and the indirect effect is a significant source of uncertainty due to the complexity of the atmospheric interactions involved, as well as the wide range of scales on which these interactions occur (Fuentes et al., 2010).

Sea salt aerosols participate in atmospheric chemistry by interacting with atmospheric pollutants. For example, sodium chloride in polluted areas (e.g. cities or areas with dense ship routes) reacts with sulfuric and nitric acid producing sodium sulfate and nitrate together with hydrochloric acid gas. The timescale of these reactions with coarse sea salt aerosols can be several hours and leads to a chloride deficit in the sea salt aerosols. As sea salt particles are transported inland during periods with onshore winds, they compete with the fine aerosol particles for sulfuric and nitric acid changing both the concentration and size distribution of the corresponding sulfate, nitrate and chloride salts. Sea salt particles cover a wide size range (about 0.05 to 10 mm diameter), and have a correspondingly wide range of atmospheric lifetimes. Thus, as for dust, it is necessary to analyze their emissions and atmospheric distribution in a size-resolved model. (Tegen et al., 1997; Athanasopoulou et al., 2008).

1.1.3. Sulphates

Sulphate aerosols are produced by chemical reactions in the atmosphere from gaseous precursors (with the exception of sea salt sulphate and gypsum dust particles). The key controlling variables for the production of sulphate aerosol from its precursors are the source strength of the precursor substances, the fraction of the precursors removed before conversion to sulphate, and the chemical transformation rates along with the gas-phase and aqueous chemical pathways for sulphate formation from SO_2. The atmospheric burden of the sulphate aerosol is then regulated by the interplay of production, transport and deposition (wet and dry). The two main sulphate precursors are SO_2 from anthropogenic sources and volcanoes, and dimethyl sulfide (DMS) from biogenic sources, especially

marine plankton. Since SO_2 emissions are mostly related to fossil fuel burning, the source distribution and magnitude for this trace gas are fairly well-known and studied. Sulphate in aerosol particles is present as sulphuric acid, ammonium sulphate, and intermediate compounds, depending on the availability of gaseous ammonia to neutralize the sulphuric acid formed from SO_2 (Houghton et al., 2001).

1.1.4. Nitrates

Aerosol nitrate is closely tied to the relative abundances of ammonium and sulphate. If ammonia is available in excess of the amount required to neutralise sulphuric acid, nitrate can form small, radiatively efficient aerosols. In the presence of accumulation mode sulphuric acid containing aerosols, however, nitric acid deposits on larger, alkaline mineral or salt particles, because coarse mode particles are less efficient per unit mass at scattering light, this process reduces the radiative impact of nitrate. Until recently, nitrate has not been considered in assessments of the radiative effects of aerosols (Li-Jones and Prospero, 1998; Gard et al., 1998; Haywood and Boucher, 2000).

1.1.5. Carbonaceous Aerosols (Organic and Black Carbon)

Carbonaceous compounds are a large group of aerosols however they are highly variable. Quantitative and qualitative analysis of organic aerosols poses substantial challenges for field measurements (Fuzzi et al., 2006) because of their small size and chemical complexity. They are also the largest single component of biomass burning aerosol. Organic carbon (OC) scatters light while black carbon absorbs it. OC dominates the submicron aerosol mass in many geographical locations, particularly downwind of urban sites (Zhang et al., 2007), regions with large biogenic OC sources (Geron, 2009), and areas affected by biomass burning (Reid et al., 2005a).

A large fraction of the OC from both anthropogenic and biogenic sources is thought to be low volatility condensed phase species that arise from photochemical oxidation of gas-phase precursors (Robinson et al., 2007). Of particular importance for the direct effect is the light-absorbing character of some carbonaceous species, such as soot and tarry

substances. Modelling studies suggest that the abundance of black carbon relative to non-absorbing constituents has a strong influence on the magnitude of the direct effect (Penner et al., 1998).

The main sources for carbonaceous aerosols are biomass and fossil fuel burning, and the atmospheric oxidation of biogenic and anthropogenic volatile organic compounds. The Global emission from biomass and fossil fuel burning has been estimated at 45 to 80 and 10 to 30 Tg/yr, respectively. Combustion processes are the dominant source for black carbon; estimates place the Global emissions from biomass burning at 6 to 9 Tg/yr and from fossil fuel burning at 6 to 8 Tg/yr (Scholes and Andreae, 2000).

1.1.6. Volcanoes

Volcanoes are a very important contributor of atmospheric aerosols to the extent that it is not a regular source which can be measured annually, however, when one of these rare occurences takes place, the extracted amount can be very large that it can be measured directly. However, volcanic emissions sufficiently cataclysmic to penetrate the stratosphere are rare. Nevertheless, the associated transient climatic effects are large and trends in the frequency of volcanic eruptions could lead to important trends in average surface temperature.

Volcanoes represent one of the most important natural sources of pollutants to the atmosphere, both during and between eruptions (Robock, 2002). Despite the lower source strength of volcanic emissions compared with anthropogenic sources like SO_2, volcanogenic sulfur species may have at least as large an effect on the Earth's radiative budget as anthropogenic sulfur (Graf et al., 1998). This is due primarily to the comparative altitude of these sources: many volcanoes degas into the free troposphere, whereas anthropogenic emissions are generally entrained in the planetary boundary layer where species lifetimes are reduced (Stevenson et al., 2003).

Tropospheric volcanic aerosols can also effect terrestrial ecosystems and human health on local to regional scales. However, the stratospheric lifetime of these coarse particles is only about 1 to 2 months, due to the efficient removal by settling. Recent volcano eruptions are mapped in Figure 1.4.

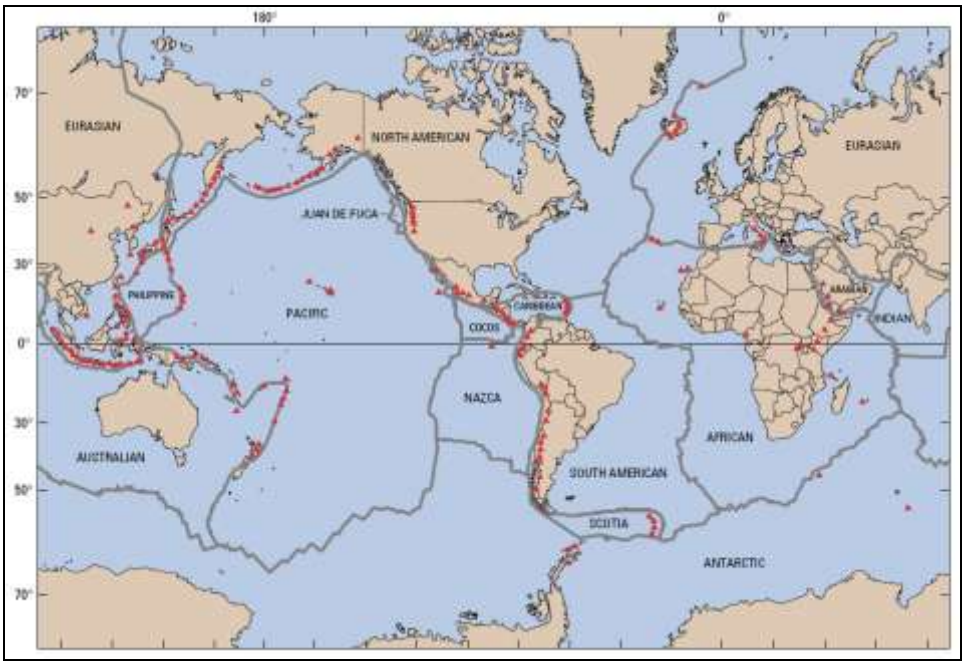

Figure 1.4. Recent volcano eruptions. (Source: USGC web site, 2009).

Figure 1.4 shows the recent volcanic eruptions in the World marked as red triangles. Ridges are drawn in grey. The historical record of SO_2 emissions by erupting volcanoes shows that over 100 teragrams of SO_2 can be emitted in a single event, such as the Tambora volcano eruption of 1815. Such large eruptions have led to strong transient cooling effects (-0.14 to -0.31°C for eruptions in the 19th and 20th centuries), but historical and instrumental observations do not indicate any significant trend in the frequency of highly explosive volcanoes (Robertson et al., 2001). Thus, while variations in volcanic activity may have influenced climate at decadal and shorter scales, it seems unlikely that trends in volcanic emissions could have played any role in establishing a longer-term temperature trend (Houghton et al., 2001).

1.1.7. Primary Biogenic Aerosols

Primary biogenic aerosol consists of all kinds of small sized biological entites like plant debris (cuticular waxes, leaf fragments, branch chips, etc.), humic matter, and microbial particles such as bacteria, fungi, viruses, algae, pollen, spores, etc. Although the occurrence and dispersion of microorganisms and spores in the air have been discussed and investigated very early in the history of aerosol science (Ehrenberg, 1830; Pasteur, 1860), unfortunately, little information is available that would allow a reliable estimate of the contribution of primary biogenic particles to the atmospheric aerosols.

Biogenic aerosols are ubiquitous in the Earth's atmosphere and they influence atmospheric chemistry and physics, the biosphere, climate, and public health. They play an important role in the spreading of biological organisms and reproductive materials, and they can cause or enhance human, animal, and plant diseases in addition to the fact that they influence Earth's radiation budget. Contribution of fungi to biogenic aerosols can initiate the formation of clouds and precipitation as cloud condensation and ice nuclei. However, enough research has not been carried on the extent of their variability in the atmosphere to understand the temporal and spatial distribution.

Primary biogenic aerosol (PBA) particles and components are emitted directly from the biosphere to the atmosphere (Elbert et al., 2007). The presence of humic-like substances makes this aerosol light-absorbing, especially in the UV-B region (Havers et al., 1998). They are important for both direct and indirect effects, but not enough is known at the present time to assess their role with any confidence.

1.1.8. Natural or Anthropogenic Forest and Grassland Fires

Although they are a very large contributor to the total load of atmospheric aerosol load, it would be difficult to address the forest and grassland fires as a natural or an anthropogenic source because although their anthropogenicity has an increasing trend, forest and grassland fires are in fact natural processes. Aerosol particle emissions from vegetation fires have large impacts on both climate and air quality. During burning periods,

the visibility in effected areas can be heavily reduced, and the health effects on the local populations can be substantial. Biomass burning particles are efficient cloud condensation nuclei (CCN) and can influence the formation of clouds and precipitation.

There is a growing interest in the indirect aerosol effect in climate models, but to fully represent the effect of aerosol emissions on cloud properties, improved particle number emission factors are needed. Currently, emission factors are mainly related to fuel types, but as the understanding of the fire process increases, the emission factors are not just treated as pure averages over the fire but can be related to fire properties as well. In this way, changes in the fire process due to meteorological effects can also be taken into account in the models.

Particle emissions from biomass burning are dominated by an accumulation mode, with a count median diameter of 100–150 nm, together with two smaller modes; a coarse mode, and occasionally also a nucleation mode (Janhall et al., 2010). The composition of the particles depends both on the fuel type and on the process of burning. The coarse mode particles consist of dust, carbon aggregates, ash and unburned parts, while the accumulation mode consists mostly of organic matter, with soot carbon and inorganic species making up 10% each. Of the organic matter 40–80% is water soluble and 20–40% consists of acids, while alcohols, sugars, levoglucosan, make up less than 5% of the organic matter (Reid et al., 2005b).

1.1.9. Industry

Transportation, coal combustion, cement manufacturing, metallurgy, and waste incineration are among the industrial and technical activities that produce primary aerosol particles. These aerosol sources are responsible for the most conspicuous impact of anthropogenic aerosols on environmental quality, and have been widely monitored and regulated. Thus, the emission of industrial dust aerosols has been reduced significantly, especially in developed countries. Considering the source strength and the fact that much industrial dust is present in a size fraction that is not optically very active (>1 mm diameter), it is probably not of climatic importance at present (Solomon et al., 2007).

1.1.10. Aerosol Direct Effect

Atmospheric aerosols originating either naturally from sources as diverse as sea salt, desert dust, volcano eruptions, natural grassland or forest fires, or generated from anthropogenic activities like fossil fuel burning or industrial activities, affect the Earth's radiation balance by absorbing or scattering the fluxes of either solar or terrestrial radiation. This change leads to radiative forcing. Scattering and absorption tend to cool the atmosphere and it is called the aerosol direct effect, i.e. the effect of aerosols on the radiative forcing is direct, they prevent the incoming solar radiation to reach the Earth's surface. With the advance of human activity, anthropogenic aerosols have increased since the preindustrial era similarly to carbon dioxide and may have had a significant influence on Earth's climate. It has been recognized that the aerosol direct effect caused by scattering and absorbing radiation may offset part of the greenhouse warming, but it is difficult to precisely determine the effect because of complexities in the aerosol transport process and in the chemical and optical properties of the aerosols (Sekiguchi et al., 2003).

1.1.11. Aerosol Indirect Effect

The aerosol indirect effect is defined as the effect of aerosols on cloud microphysics, such that aerosols modify the cloud properties by both altering the cloud albedo and changing cloud reflectivity or by affecting rainfall patterns by means of changing cloud inner structures to delay droplet formation.

Aerosols influence the atmospheric radiative balance not only by directly absorbing or scattering the radiation (direct effect), but by changing cloud reflectivity and lifetime. In fact, an excess of aerosols in the atmosphere can cause a larger number of aerosols to act as CCN for cloud droplets, increasing the cloud reflectivity and therefore influencing the planetary albedo, an important quantity in the calculation of the atmospheric radiative balance. This effect is called the first indirect effect, to distinguish it from the so-called second indirect effect which represents the influence that aerosols have on cloud lifetimes. In the presence of an increased number of CCN, for a certain amount of water vapor, the water will be shared among a larger number of nuclei, and therefore this will make droplets

that form to be smaller in size. This will cause a decreased likelihood of precipitation. Cloud lifetimes will increase and precipitation rate will decrease eventhough there's enough amount of water vapor to form rain (Seinfeld and Pandis, 2006; Russo, 2007). In Figure 1.5, direct and indirect effects of aerosols are illustrated.

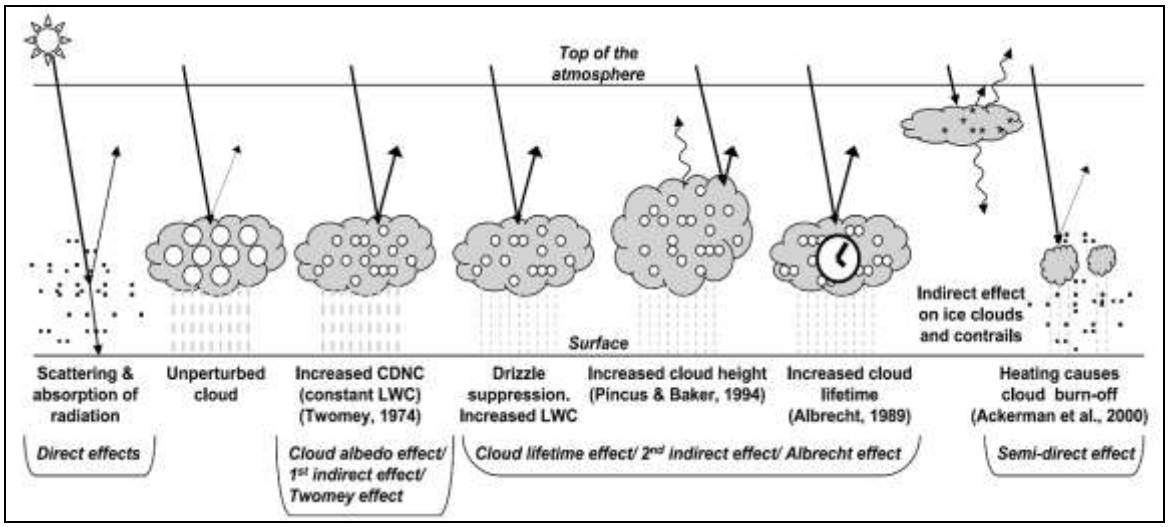

Figure 1.5. Schematic diagram of aerosol effects

Figure 1.5 shows the various radiative mechanisms associated with cloud effects that have been identified as significant in relation to aerosols. Small black dots represent aerosols and the larger open circles represent cloud droplets. Straight lines are the incident and reflected solar radiation and wavy lines represent terrestrial radiation. The filled white circles indicate cloud droplet number concentration (CDNC). The perturbed cloud contains larger drops as only natural aerosols are available as CCN, while the perturbed cloud contains a greater number of smaller cloud drops as both natural and anthropogenic aerosols are available as CCN. The vertical grey dashes represent rainfall and LWC refers to liquid water content (Solomon et al., 2007). Since the effect on the radiative forcing is not immediately followed by a change in the climate, there is a major uncertainty with the predictions. In the report of the Intergovernmental Panel on Climate Change (IPCC), it was stated that aerosol indirect effect is the most important source of error in climate modeling which is illustrated in Figure 1.6 (Houghton et al., 2001).

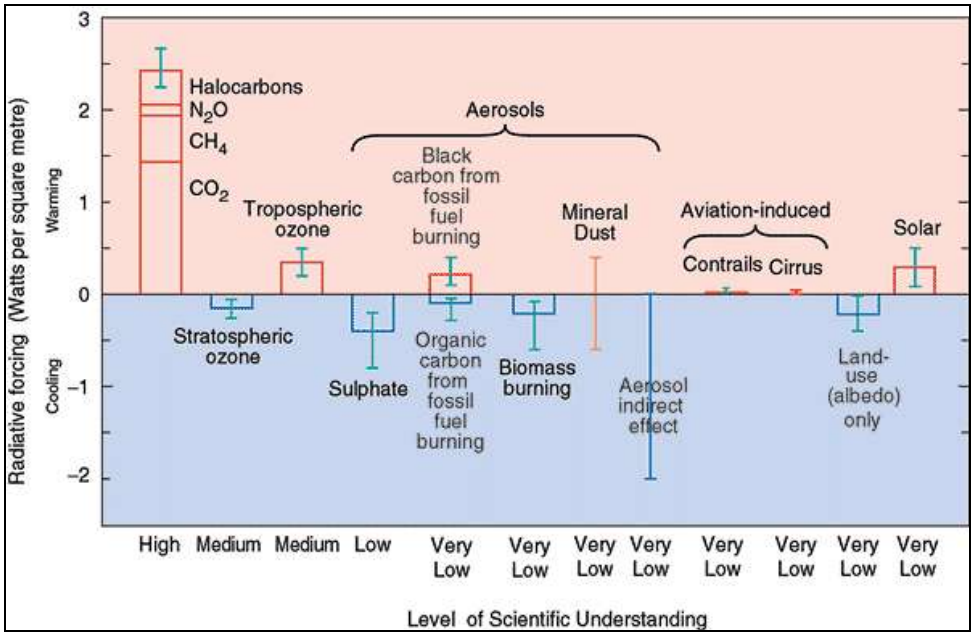

Figure 1.6. Global mean radiative forcing of the climate system for the year 2000, relative to to 1750.

In Figure 1.6, atmospheric constituents and their negative or positive effects on Global radiative forcing are illustrated. It can be deducted that the Level of Sceintific Understanding for Aerosol Indirect Effect on Radiative Forcing is very low and the variance is maximum (Houghton et al., 2001). In a recent study (Russo, 2007), it is stated that the main difficulty in the measurement of the aerosol indirect effect is because aerosols, unlike greenhouse gases that become well-mixed in the atmosphere, are not uniformly distributed in the atmosphere and their concentration can change quickly with time. Also some aerosols are more effective as CCN than others depending on their hygroscopicity. In fact not all the aerosols get "activated" into cloud droplets, activation being a process which depends on both the level of supersaturation and the aerosol hygroscopicity.

1.1.12. Health Impacts Related with Aerosols

The lungs, skin and the intestinal tract of human body are in direct contact with the environment being likely to be the first ports of entry into the body. Epidemiological studies showed a positive correlation between increases in atmospheric particle concentrations and the short-term increases in morbidity and mortality (Yang et al, 2008). Inhalation is the most significant exposure route for atmospheric aerosols through the two functional parts of the respiratory system: the airways (trachea, bronchi and bronchioles) and the alveoli. The location, extent and efficiency of the deposition of the particles depend on three factors: (i) particle size, density, surface properties and shape, (ii) anatomy of the airways and alveolar structure, and (iii) ventilatory parameters, breath pattern, flow rates and tidal volume (Gronenberg et al, 2003). For the particle to successfully reach deep into the lung, it has to be small enough to avoid deposition by inertial impaction on upper airways and can pass through lower airways, and also large enough to aviod exhalation. The optimal size for achieving delivery deep into the alveolar region is between 1 and 3 μm aerodynamic diameter, however this is a bimodal process and ultrafine particles (diameter smaller than 100 nm) also succesfully settle the alveolar region (Gill et al., 2007).

Anthropogenic particle emissions have massively increased since preindustrialized times and account for a major fraction of particulate matter especially in polluted urban environments as well as in the global atmosphere. Although numerous studies have shown that both natural and anthropogenic aerosols have a strong impact on human health, due to the limited knowledge of aerosol sources, composition and properties, the actual effects of aerosols are still far from being fully understood and quantified. Numerous epidemiological studies show that fine air particulate matter and traffic related air pollution are correlated with severe health effects, including enhanced mortality, cardiovascular, respiratory, and allergic diseases. Moreover, toxicological investigations in vivo and in vitro have demonstrated substantial pulmonary toxicity of model and real environmental aerosol particles, but the biochemical mechanisms and molecular processes that cause the toxicological effects such as oxidative stress and inflammatory response have not yet been

resolved. Among the parameters and components potentially relevant for aerosol health effects are the specific surface, transition metals, and organic compounds (Pöschl, 2005).

Particularly little is known about the relations between allergic diseases and air quality. Nevertheless, traffic-related air pollution with high concentration levels of fine air particulate matter, nitrogen oxides, and ozone is one of the prime suspects besides non-natural nutrition and excessive hygiene practices, which may be responsible for the strong increase of allergies in industrialized countries over the past decades. The most prominent group of airborne allergens are protein molecules, which account for up to 5% of urban air particulate matter. They are not only contained in coarse biological particles such as pollen grains (diameter >10 mm) but also in the fine fraction of air particulate matter, which can be explained by fine fragments of pollen, microorganisms, or plant debris and by mixing of proteins dissolved in rain water with fine soil and road dust particles (Bernstein et al., 2004).

A molecular rationale for the promotion of allergies by traffic-related air pollution has been proposed and it was who found that proteins including birch pollen allergen Bet v1 are efficiently nitrated by polluted urban air. The nitration reaction converts the natural aromatic amino acid tyrosine into nitrotyrosine and proceeds particularly fast at elevated concentrations of photosmwho og, most likely involving nitrate radicals as reactive intermediates. From biomedical and immunological research it is known that protein nitration occurs upon inflammation of biological tissue, where it may serve to mark foreign proteins and guide the immune system (Franze et al., 2003; Franze et al., 2005).

Moreover, conjugates of proteins and peptides with nitroaromatic compounds were found to evade immune tolerance and boost immune responses, and posttranslational modifications generally appear to enhance the allergenicity of proteins. Thus, the inhalation of aerosols containing nitrated proteins or nitrating reagents, is likely to trigger immune reactions, promote the genesis of allergies, and enhance the intensity of allergic diseases and airway inflammations. This hypothesis is supported by first results of ongoing biochemical experiments with nitrated proteins (Franze et al., 2003; Franze et al., 2004; Franze et al., 2005).

For efficient elucidation and abatement of adverse aerosol health effects, the knowledge of atmospheric and biomedical aerosol research should be integrated to formulate plausible hypotheses that specify potentially hazardous chemical substances and reactions on a molecular level. These hypotheses have to be tested in appropriate biochemical and medical studies to identify the most relevant species and mechanisms of interaction and to establish the corresponding dose response relationships. Ultimately, the identification and characterization of hazardous aerosol components and their sources and sinks (emission, transformation, deposition) should allow the optimization of air-pollution control and medical treatment of aerosol effects on human health (Pöschl, 2005).

1.2. Investigation of Aerosols by Lidar

In this section, basic topics about lidars and the investigation process will be briefly described. The history of lidar technology will be mentioned and the working principles will be explained. Scattering theories behind lidar systems like Mie, Rayleigh and Raman scattering will be explained and the physical events about light scattering like polarization will be explained also in this section. The aerosol microphysical parameters will be briefly defined. There are two sections of the literature review about lidar applications on aerosol studies and of the aerosol research in Turkey. This is section and the Introduction chapter end with the existing lidar networks in the World.

1.2.1. Lidar Basics

The history of lidar extends back to 1930's even before the invention of the first maser in 1954 and the first ruby laser in 1960, although today all lidars use lasers as the transmitting unit. The first attempts to measure air density profiles in the atmosphere were realized in the 1930's, by determining the backscatter intensity from a continous wave searchlight beam. In 1937, Hulbert could photograph the searchlight beam up to 10 kilometers height. In 1938, pulses of light were used for the first time to measure cloud base heights. The generation of light pulses by electric sparks and flashlamps allowed the replacement of the bistatic configuration by a monostatic setup, i.e., a setup in which transmitter and receiver are collocated and the height information is actively deduced from

a measurement of the round-trip time between pulse emission and signal detection. The acronym of lidar for these kind of measurements was first introduced by Middleton and Spilhaus (1953). After the invention of laser in 1960 and the production of the giant-pulse (Q-switched) technique, Fiacco and Smulin (1963) used lasers for the study of upper atmosphere and Ligda (1963) investigated the first laser transmitter lidar investigation in the troposphere. Consequently, the first textbook on lidar edited by Hinkley appeared in 1976. Ever since, success in lidar development was strongly connected with progress in optical and electronic technology, in particular laser technology. Lidar researchers have always been involved in laser development. Many instruments use lasers specifically designed for lidar to meet the high requirements of certain lidar techniques on laser power, wavelengths, pulse width, beam shape, and spectral purity often not fulfilled by commercial products. In addition to lasers, optical filters with high transmissivity, narrow bandwidth, steep spectral slopes and/or high out-of-band suppression, efficient detectors for broad wavelength regions, data acquisition systems with a dynamic range of several orders of magnitude, and computers that can process large amounts of data with high repetition rate belong to the devices needed for advanced lidar systems. Lidar has therefore always been both a source and a beneficiary of technological innovation (Weitkamp, 2002).

The first application of lidar was the detection of atmospheric aerosols and density. Basically, it is to know whether there are aerosols/density in the regions and how much, however, the composition of atmosphere could not be determined, because only the scattering intensity was detected but nothing about the spectra. An important advance in lidar techology was the recognition that the spectra of the detected radiation contained highly specific information related to the species, which could be used to determine the composition of the object region. The broad selection of laser wavelengths became available and some lasers could be precisely tuned to specific frequencies. All these advancements enhanced the effective spectral analysis of the returned radiation from objects. This ability added a new dimension to remote sensing and made possible an extraordinary variety of applications which range from groundbased probing of the trace-constituent distribution in the tenuous outer reaches of the atmosphere (upper atmosphere lidar), to lower atmosphere constituents (differential absorption lidar), to airborne

chlorophyll mapping of the oceans to establish rich fishing areas (fluorescence lidar)(University of Colorado at Boulder web site, 2008).

Today, lidar is a very useful instrument which is frequently used in aerosol science. Because of the nature of aerosols, it is not easy to study them. With in situ observations and sampling, the aerosols are disturbed therefore, the measured parameters no longer belong to that aerosol layer. Due to the fact that aerosols are difficult to access, by in situ sampling, only data from a certain location can be acquired, however with lidar, the data acquisition is range resolved, i.e. data can be acquired from all altitudes simultaneously. Also, lidar data is easy to obtain, once the system is set up, unlimited amount of data can easily be acquired allowing long term measurements for the investigation of seasonal and diurnal variations of the aerosol parameters.

Lidar works on the principle of sending laser light in the atmosphere to collect the backscattered portion inside a detector. The basic scheme of a lidar system is shown in Figure 1.7. Laser beam is sent into the atmosphere and it interacts with molecules and aerosols. The part of the beam which is scattered back is collected by a telescope and sent to an optical system, where the light is selected based on different wavelengths. The light that reaches each channel is collected by detectors and from there it is directed to a data acquisition system converting the voltage from the photomultipliers into electronic signals.

The light from the laser permits the acquisition of signal profiles as a function of range, which is the distance from the instrument to the scattering volume. A typical lidar has an overlap region which can be defined as the ranges for which the laser beam is not entirely included in the field-of-view (FOV) of the telescope. This implies that a correction needs to be applied for the data within the overlap region to be used for quantitative purposes. A light beam that travels in the atmosphere undergoes different types of interactions, namely scattering and absorption by molecules and aerosol particles. Scattering is the process by which a particle, with an index of refraction different from the surrounding medium, abstracts energy from the incident wave and re-radiates that energy into the total solid angle centered on the particle. Depending on the size of the particle, the

spatial distribution of the scattered light changes (Russo, 2007). A simplified scheme of the lidar system is demonstrated in the following figure (1.7).

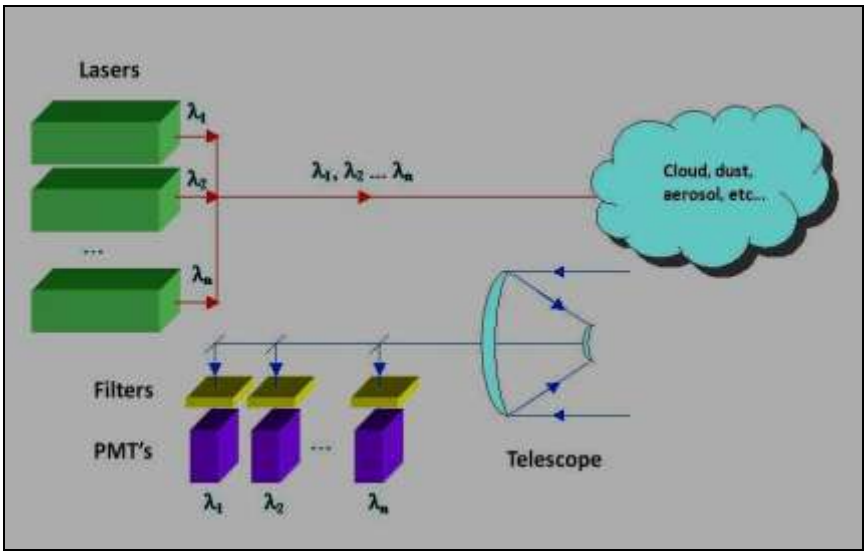

Figure 1.7. Simple scheme of a lidar system.

Here in this simplified scheme of a lidar system in Figure 1.7, green boxes represent emission of wavelengths of lasers transmitted simultaneously and coaxially. The lasers hit the target (cloud, dust, aerosol, etc) and the backscattered light is collected by the telescope, and then to directed into the photo multiplying tubes (PMT). The process of lidar system flow will be further discussed in the Methodology chapter.

1.2.2. Light Scattering by Atmospheric Aerosols

For the study of the atmospheric aerosols by lidar technology, some optical theories must be known prior to the detailed explanation of the atmospheric phenomena. When light interacts with the particles in the atmosphere, the source of which is either the sun, or a transmitted laser beam in the case of lidar technology, some optical events occur, which will be the basis of the measurements which have been carried throughout this dissertation. These processes of emission, scattering and absorption were named

respectively as the birth of photons, the life of photons and the death of photons (Bohren and Clothiaux, 2006).

When a photon interacts with the particle, it may reflect from the surface with any angle in the 3-D space. If it reflects with 180^0 degrees, the process will be called "backscattering" through the thesis. If the energy of the incident photon is either absorbed by the molecules of the particle or scattered in any direction except 180^0 degrees, it will be called "extinction". Extinction can also be described as how fast the intensity of an initial radiation drops down during the propagation through a medium. In our case, radiation is the laser beam and medium is the atmosphere. However, the energy of the incident photon can either be conserved or changed and usually both. So when the incident light is reflected with the same frequency it is called to be scattered "elastically", and if the wavelength of the incident radiation shifts to another special wavelength which is the fingerprint of the particle, it is called to scatter "inelastically". So when the photons from the incident laser beam hits the atmospheric particles, the light is scattered both elastically and inelastically. The elastically scattered portion is many orders of magnitude more intense than the inelastically scattered portion. This phenomenon is called Raman scattering and it is a signature for the material on which the light scatters (Seinfeld and Pandis, 2006).

Another phenomenon which is directly related with lidar study is polarization. Light travels as a tranverse wave and has two vectors, electric and magnetic and these two vectors are always perpendicular to each other. When the incident light is reflected from the surface of a particle, the polarization changes according to the shape of the particle. If the particle has a spherical shape, the polarization will not change, but if the particle is irregularly shaped, then the polarization will change.

The scattering of light by gases was first treated quantitatively by Lord Rayleigh in 1871 in an effort to explain the blue color of the sky and the red color of the sunset. There are numerous ways of arriving at the equation which governs Rayleigh scattering. Classical electromagnetic theory can be employed using the far-field solution while retaining only the dipole term. Rayleigh scattering can be studied considering the particle (or molecule in this case since the radius is considered to be much smaller that the wavelength of the

incident radiation) as a dipole that vibrates when it interacts with electromagnetic radiation. The oscillating dipole is then a source of emission of electromagnetic radiation, at the same wavelength as the incident light (Seinfeld and Pandis, 2006).

Mie scattering occurs when the particle size is of the same order of magnitude as the wavelength of the incident radiation. In its original formulation, Mie scattering assumed a homogeneous, isotropic and optically linear material irradiated by an infinite plane wave. This formulation can be extended to particles of smaller sizes, giving a spatial distribution for the scattered light consistent with what is found using Rayleigh scattering theory. In other words the small particle limit of the Mie formulation is Rayleigh scattering (Seinfeld and Pandis, 2006).

The interaction between a molecule and electromagnetic radiation can excite both rotational and vibrational transitions in the molecule and then re-emit the radiation in the decaying process. If the incident radiation is monochromatic and of certain frequency, the scattered radiation by a molecule will contain not only radiation of the same frequency (Rayleigh scattering) but also weaker radiation of another wavelength due to either rotational or vibrational Raman scattering. The scattered spectrum will then have Raman lines on each side of the Cabannes line. The Cabannes line, named after one of Lord Rayleigh's students, is the portion of the Rayleigh scattering spectrum that is commonly described as elastic. In fact most in the lidar field include rotational Raman scattering in their definition of elastic scattering although this is not a completely correct definition since approximately 3% of the Rayleigh signal is due to inelastic rotational Raman scattering. The Rayleigh spectrum includes the Cabannes line and the pure rotational Raman lines. The frequency difference between the scattered and incident radiation is characteristic of the allowed transitions in the scattering molecule. The number of transitions possible is quantized and described by quantum mechanics. Rotational and vibrational transitions are allowed in molecules and therefore rotational and vibrational Raman scattering can both occur. The shift in wavelength that is a characteristic of Raman scattering depends on the molecule being sensed. This permits measurement of the scattering by a particular molecule in the atmosphere with a lidar by collecting the scattered radiation at the appropriate wavelength (Seinfeld and Pandis, 2006; Russo, 2007).

Mathematical background for the retrieval and interpretation of the lidar data will be provided later in the Methodology section, however some introductory notes is given here. Lidar equation is a quantitative approach to relate the received light intensity, or the photon counts with the initially transmitted laser intensity, propagation of the light in the atmosphere, physical interactions between the light and the particles, and the efficiency and geometry of the lidar system. When light propogates in the atmosphere, it is scattered and absorbed by molecules and particles, therefore there is a loss during the propagation. Lidar measures extinction and backscatter coefficients, and through the inversion of this data, particle microphysical parameters are obtained which will be described in detail in the Methodology section.

1.2.3. Aerosol Microphysical Parameters

Due to these events of scattering, absorption and polarization, the microphysical parameters of aerosols can be calculated from the data acquired by the multiwavelength Mie-Raman lidar. The parameters which will be discussed in detail in the Results chapter, can be listed as, complex refractive index, surface area density, volume density, effective radius. The related phenomena, particle size distribution (PSD), particle and volume depolarization and water vapor mixing ratio and the brief descriptions will be discussed here within.

Complex refractive index is one of the most important microphysical parameters of atmospheric particles. Refractive index is like the fingerprint of a material, and therefore interpretation is possible by means of the retrieval of this parameter. So, the refractive index of a medium, in our case this medium is the particle, can be defined as the ratio of the speed of the incoming laser light in a reference medium, which is the atmosphere itself, to the phase speed of the light wave in the medium. However, in the real world, this situation needs the introduction of some extra concepts, therefore complex refractive index is used for aerosol parameters. Complex refractive index is a function which consists of real and imaginary parts, and the values of these parts help to specify aerosols. By the help of the custom programmed software, refractive index can be retrieved. Number density (N) of aerosols is the number of aerosols in a unit volume, and volume density (V) is the

volume of aerosols in a unit volume. Surface area density (S) is the total surface area of aerosols in a unit volume. Mean radius is the average of the sizes of aerosols in a unit volume, however, for a better understanding, effective radius, which is the area weighted mean of aerosols, is often used in aerosol size, because aerosol size distribution generally has two modes. These parameters are important for the particle size distribution (PSD). PSD can be defined as the list of values or a mathematical function that defines the relative amounts of particles present, sorted according to size within a unit volume.

1.2.4. Review of Lidar Applications for Aerosol Studies

Dust aerosols play an important role in the Earth's radiation budget (Sokolik et al., 2001) therefore their continuous monitoring carries outmost importance. Dust intrusions can modify the temperature, dynamics and chemical composition of the atmosphere via heterogeneous reactions. To estimate the corresponding radiative forcing, the quantification of size-dependent optical properties of the dust particles is required. Information about the vertical distribution of dust particles both close to a major source region as well as during intrusion episodes has been gained during the last decade by means of elastic-backscatter (Liu et al., 2008), Raman and high spectral resolution lidars (HSRL) (De Tomasi et al., 2003; Perrone et al., 2004; Mona et al., 2006; Xie et al., 2008). Raman and HSRL lidars allow an independent calculation of aerosol extinction and backscattering coefficients (Ansmann et al., 1992), together with particle depolarization ratio and are widely used to characterize dust particle properties. For example, much information about dust particle properties was obtained during the Saharan Mineral Dust Experiment (SAMUM) (Heintzenberg et al., 2009, Ansmann et al., 2009; Esselborn et al., 2009; Freudenthaler et al., 2009; Tesche et al., 2009; Wiegner et al., 2009) using a unique "lidar-park", including Raman and HSRL systems.

The retrieval capabilities of Raman lidars are improved when the measurements are performed at multiple wavelengths. With this information, microphysical properties of aerosols can be retrieved through mathematical inversion (Müller et al., 1999; Veselovskii et al., 2002; Veselovskii et al., 2004). However an application of these multi-wavelength (MW) algorithms to dust measurements must overcome certain obstacles. For example, all

existing lidar algorithms model aerosols as an ensemble of spherical particles even though it is well established that backscattering by of irregularly shaped particles is weaker than that predicted by the Mie theory for spheres of equivalent volume. Moreover, lidar backscatter from dust particles is strongly depolarized. The spectral dependence of the particle depolarization ratio contains information about particle parameters, but in the framework of the Mie theory this information cannot be exploited in the retrieval. Therefore, the importance of accounting for particle non-sphericity in lidar retrievals is currently well recognized. However, until now this effect remains under-accounted for in all existing lidar algorithms.

Furthermore, accounting for the effects of particle shape in light scattering is not an issue inherent in lidar techniques only. It is a fundamentally difficult problem that imposes significant limitations on the accuracy of estimates of desert dust aerosol properties with most remote sensing techniques (Mishchenko et al., 2000; Dubovik et al., 2006; Yang et al., 2007). The development of a light scattering model for the retrieval of desert dust properties meets serious obstacles because of the complex nature of the formalism describing light scattering. In situ and laboratory measurements also have issues with sampling of unperturbed aerosols, which complicates the characterization of the particles (Haywood et al., 2003; Reid et al., 2003a; Reid et al., 2003b; Tanré et al., 2003). The optical properties of particles with diverse geometrical shapes and morphologies have been studied for a number of years, but exact solutions describing the interaction of the electromagnetic field with a single particle exist only for several specific geometrical shapes (Mishchenko et al., 2000; Mishchenko et al., 2002). Existing numerical methods, such as the discrete dipole approximation (Draine and Flatau, 1994) and finite-difference time-domain technique (Yang et al., 2000), are more flexible in general, but are very time consuming and in practice can be applied only to particle sizes comparable to and smaller than the wavelength.

To overcome these problems, to model natural non-spherical aerosol with a mixture of polydisperse, randomly oriented spheroids started to be used, and this approach demonstrated that to reproduce adequately the phase functions measured in the laboratory for desert dust (Mishchenko et al., 1995; Mischenko et al., 1997). Subsequently, this

concept has been widely employed in numerous applications to account for light scattering effects caused by deviations of particle shapes from that of a sphere. The operational retrieval algorithm employed by the AERONET (**AE**rosol **RO**botic **NET**work) network of ground-based sunphotometers is, perhaps, one of the most vivid examples of using the model of spheroids for the interpretation of aerosol remote sensing observations (Holben et al., 1998). First, the spheroid model to identify and evaluate the retrieval errors caused by neglecting the effect of particle non-sphericity on AERONET retrievals was used (Dubovik et al., 2002a; Dubovik et al., 2002b). More recently, Dubovik et al. (2006) have developed an approach which allows fast and accurate computations of spheroid ensemble scattering based on pre-calculated look-up-tables of scattering kernels and included the spheroid model in the AERONET retrieval algorithm developed earlier by Dubovik and King (2000) in order to account for the shape effects.

More than five years of experience with this AERONET code have demonstrated essential improvements in the retrieval of dust properties. The same concept for the incorporation of a spheroidal model into the lidar retrieval of aerosol physical properties is also adopted. Following the positive experience with the AERONET retrieval development, morphologically complex aerosols as a mixture of spherical and non-spherical components were modeled the non-spherical component being an ensemble of randomly oriented spheroids with a size-independent shape distribution. This algorithm is a generalization of previously published approach (Veselovskii et al., 2002; Veselovskii et al., 2004; Veselovskii et al., 2009) to the retrieval of particle parameters from multi-wavelength lidar data.

One of the most important key factors influencing the properties of scattering of the aerosols is their hygroscopicity. As the relative humidity (RH) rises, uptake of water vapor by hygroscopic aerosols increases the particle size, which generally leads to an increase in light-scattering (Hanel, 1976). Many experimental studies of the relationship between scattering of aerosols and relative humidity have been performed in the laboratory with aerosols of known chemical composition (Kumar et al., 2003; Svenningsson et al., 2006; Kreidenweis et al., 2006). In-situ experiments in the natural environment have also been performed using nephelometers (Carrico, 2003) and differential mobility analyzers

(Swietlicki et al., 2008) in tandem with humidity control systems. Under the right conditions, a lidar may provide another tool for studying aerosol hygroscopicity. The advantage of using a lidar (as opposed to laboratory or most in-situ studies) is that it can provide relatively continuous altitude-resolved measurements of aerosol properties without perturbing the aerosol or its surroundings, which is really the biggest advantage of remotely studying aerosols. The obvious disadvantage is that, because the aerosol sampled by the lidar is not controlled in any way (e.g., source, state, chemical composition, etc), lidar studies of aerosol hygroscopicity need to be limited to occasions when the same aerosol type exists in at least a portion of a profile that is characterized by widely changing RH so that observed differences in aerosol properties can be attributed primarily to water uptake as RH increases.

The enhancement of lidar backscatter due to particle swelling was first considered more than four decades ago (MacKinnon, 1969). Since then numerous studies have investigated the relationship between aerosol backscattering and relative humidity (Feingold and Morley 2003; Pahlow et al., 2006; Raut and Chazette, 2007, Cuesta et al., 2008). The water vapor mixing ratio in these more recent studies was derived from either lidar measurements, Raman (Pahlow et al., 2006) and differential absorption (Wulfmeyer and Feingold, 2000), or was calculated under a boundary layer cloud deck suggesting a well-mixed boundary layer (Feingold and Morley, 2003). If the boundary layer is well mixed, then any change in backscattering in the vertical column is considered to be due to uptake of water vapor by the particles. Assuming that the atmosphere is saturated at cloud base and assuming that the potential temperature is constant with height, the relative humidity profile can be calculated (Pahlow et al., 2006; Wulfmeyer and Feingold, 2000; Feingold and Morley, 2003). Using single-wavelength backscatter lidar data combined with thermodynamic assumptions of the mixing state of the atmosphere allows for the determination of the hygroscopic growth factor f (RH) for relative humidity close to saturation. The growth factor is calculated in terms of backscattering at a given RH, relative to some lower reference RH. The application of the multi-wavelength Raman lidar technique has an advantage over single-wavelength measurements, because it increases the amount of available information allowing derivation of the particle size distribution and other physical properties along with the water vapor mixing ratio.

The possibility of using the multi-wavelength lidar method for the study of cloud condensation nuclei (CCN) was considered earlier (Feingold and Grund, 1994), but experimental implementation of this method is relatively more recent. The increase of particle size and extinction coefficient near the PBL top derived from multi-wavelength lidar measurements during the ACE 2 (Aerosol Characterization Experiment) field campaign has been reported (Müller et al., 2002; Ansmann et al., 2002). As inversion routines and retrievals improve and additional aerosol products become available (for example, particle size distribution (PSD), and refractive index), the use of multi-wavelength lidar to investigate aerosol hygroscopicity may provide new insights into the aerosol microphysical properties relevant for climate forcing in the atmosphere.

The regularization technique was successfully used during the last decade to invert the aerosol backscattering and extinction coefficients measured by a multiwavelength (MW) Raman lidar to particle microphysical properties (Müller et al., 1999; Veselovskii et al., 2002). However the regularization approach is time-consuming and is characterized by high sensitivity to the noise in the input optical data. Meanwhile, the integral particle properties such as volume (V), surface (S) density, effective radius (R_{eff}) can be retrieved with the principal component analysis technique (PCA) (Donovan et al., 1997; De Graaf et al., 2008; De Graaf et al., 2009). In such an approach the bulk particle parameters are represented as a linear combination of input optical data (β, α), which makes the retrieval extremely fast. In addition, PCA is more tolerant to the noise in the input data.

1.2.5. Aerosols Studies in Turkey

Although there are a number of in situ studies of aerosols which have been carried in Turkey in the last decade, remote sensing data is scarce. Few studies using passive remote sensing instruments were made, which were summarized here. Aerosol measurements are mostly done by in situ sampling. Karakas and Tuncel (1998) collected aerosol samples daily at a rural mountainous site of northwestern Anatolia during September 1993–April 1994. Concentrations of SO_4^{2-}, NO_3^-, Cl^{-1}, NH_4^+, Na^+, K^+, Ca^{2+} and Mg^{2+} have been determined. Sulfate made up the 30% analyzed aerosol mass with a 2.14 μm^{-3} average concentration. Measured concentrations were comparable with other

rural area data except Ca^{2+} which was higher with an average concentration of 1.12 μgm^{-3} Monthly concentrations of major ions fluctuated depending on meteorological factors, seasons and source strengths. Saharan dust storms affected the sampling site especially in autumn and spring seasons. Wind sector analysis indicated that the most important source regions were located both to the south and north of the station. However, air masses from south at which a power plant is located have been concluded to bring the greatest amount of anthropogenic pollutants to the sampling site (Karakas and Tuncel, 1998).

Yatin et al. (2000) studied fine and coarse aerosols by sampling using stack filter unit in Ankara, Turkey, between February and June 1993. Collected samples were analyzed for approximately 40 trace elements and major ions using a combination of instrumental neutron activation analysis, atomic absorption spectrometry and ion chromatography. Particle sizing characteristics were tested against dichotomous sampler. Fossil fuel combustion was found to be the main source of anthropogenic elements in aerosols, including the ones with well-known industrial sources. Atmospheric loading and seasonal variations in the concentrations of crustal elements were determined by the variations in wind speed and moisture of the soil. Short-term episodes in the concentrations of all elements were governed by local meteorology, particularly by the wind speed and mixing height. Concentrations of elements with anthropogenic origin had fairly similar concentrations in all wind sectors as they are distributed uniformly over the city and its suburbs due to low annual average wind speed. Changes in the concentrations of anthropogenic elements in Ankara atmosphere were consistent with the history of regulatory actions taken to reduce air pollution. Moreover, an unexpected decrease in the concentrations of crustal elements between 1975 and 1993 is related to reduction in exposed earth surface due to rapid urban development (Yatin et al., 2000).

Samura et al. (2003) studied the concentrations of heavy, trace elements and major ions measured in the Uludag and Bursa aerosols to investigate to assess size distributions, spatial and temporal variability, sources and source regions affecting the composition of aerosols. 81 samples were collected in two sites, one in Bursa city and another in the Uludag Mountain during two sampling campaigns. Daily samples were collected using a high volume sampler on Whatman 41 cellulose filters in Uludag, while three days interval

samples were collected in Bursa using an automatic dichotomous sampler on PTFE Teflon filters. Samples were analyzed for 15 trace and heavy metals and 4 major ions using ICP-AES, GFAAS, HPLC and UV/VIS Spectrophotometer, respectively. In general, concentrations of the metals measured in Uludag aerosols were lower than those in Bursa. The concentrations of crustal elements were higher in summer than winter, while anthropogenic elements had higher concentrations in winter than summer. Most of the mass of crustal elements was concentrated in the coarse mode while the mass of the heavy metals was concentrated in the fine mode. Factor analysis revealed four factors with sources including crustal, industrial and combustion. Back trajectory calculations were used to determine long range contributions. These calculations showed that contributions were mostly from European countries, former Soviet Union countries, Black Sea and North Africa (Samura et al., 2003).

Karaca et al. (2005) studied the statistical characterization of particulate matter concentrations by monitoring PM_{10} at several stations. Information about fine fraction aerosols ($PM_{2.5}$) in Istanbul atmosphere was not reported. 86 daily aerosol samples were collected between July 2002 and July 2003. The PM_{10} annual arithmetic mean value of 47.1 μgm^{-3}, was lower than the Turkish air quality standard of 60 μgm^{-3}. On the other hand, this value was found to be higher than the annual European Union air quality PM_{10} standard of 40 μgm^{-3}. The annual mean concentration of $PM_{2.5}$ 20.8 μgm^{-3} was found higher than The United States EPA standard of 15 μgm^{-3}. The statistics and relationships of fine, coarse, and inhalable particles were studied. Cyclic behavior of the monthly average concentrations of PM_{10} and $PM_{2.5}$ data were investigated. Several frequency distribution functions were used to fit the measured data. According to *Chi*-squared and Kolmogorov–Smirnov tests, the frequency distributions of $PM_{2.5}$ and PM_{10} data were found to fit Log-logistic functions (Karaca et al., 2005).

Another study (Tasdemir and Kural, 2005) dealed with trace element dry deposition fluxes, measured using a smooth, greased, knife-edge surrogate surface holding greased Mylar strips in Bursa, Turkey. Sampling program was conducted between October 2002 and June 2003 and 46 dry deposition samples were collected. The average fluxes of crustal metals (Mg, Ca, and Fe) were one to four orders of magnitude higher than the fluxes of

anthropogenic metals. Trace element fluxes ranged from 3 (Cd) to 24 230 (Ca) μg m^{-2} d^{-1}. The average trace element dry deposition fluxes measured in this study were similar to those measured in other urban areas. In addition, ambient air samples were also collected simultaneously with flux samples and concentrations of trace elements, collected with a TSP sampler, were between 0.7 and 4900 ng m^{-3} for Cd and Ca, respectively. The overall trace element dry deposition velocities, calculated by dividing the fluxes to the particle phase concentrations ranged from 2.3±1.7 cm s^{-1} (Pb) to 11.1±6.4 cm s^{-1} (Ni). These values are in good agreement with the values calculated using similar techniques. The anthropogenic and crustal contributions were estimated by employing enrichment factors calculated relative to the average crustal composition. Low enrichment factors for dry deposition samples were calculated (Tasdemir and Kural, 2005).

Kindap et al. (2006) aimed to study the transport of air pollutants from Europe to Northwestern Turkey to identify and analyze the contribution of long-range aerosol transport to air pollution in the city of Istanbul. Meteorological modeling provided the wind fields that were first used in a trajectory analysis and then, along with other meteorological data, input to an advanced air quality model. Backward trajectories suggested that when the prevailing wind direction is westerly or northwesterly, such as in the case of the episode studied, a significant fraction of the pollutants emitted from Europe may be transported to and deposited in Turkey. An emission processing module was developed to prepare the emission inputs required by the air quality modeling system. The long-range aerosol transport simulations demonstrated and quantified the source/receptor relationships between Europe and Turkey. For the selected episode, it has been found through model simulations that the responses of Istanbul background PM_{10} levels to the emissions of individual European countries can range from 0.5 to 13%. The response of Istanbul background PM_{10} concentrations can be as much as 26% according to the sensitivity analysis results, when anthropogenic emissions throughout Europe are changed by 50%. Result suggested that trans-boundary sources may be responsible for as much as half of the background PM_{10} in Istanbul (Kindap et al., 2006).

In another study (Vrekoussis et al., 2005), aerosol optical properties (scattering and absorption coefficients) were investigated by passive remote sensing devices at two remote

locations in the Eastern Mediterranean in conjunction with aerosol ion composition measurements: Finokalia in the Crete Island in Greece (March 2001–June 2002) and Erdemli in Turkey (July 1999–June 2000). Ambient light-scattering coefficient at Finokalia had a mean value of 50±23 Mm^{-1} while at Erdemli this value was calculated as 90±160 Mm^{-1}, due to a severe dust event that occurred from 17 to 19 April 2000. Scattering coefficients up to 5000 Mm^{-1} were encountered during the transition periods (Spring and Autumn) and were associated with dust storm events. During these events significant correlations were observed between dust and scattering coefficients and mass scattering efficiencies of 0.21 and 0.96 m^2g^{-1} were calculated for dust for Finokalia and Erdemli, respectively. Significant correlations were also observed at both locations between non-sea-salt sulphate (nss-SO_4^{2-}); scattering coefficients and mass scattering efficiencies of 5.9±1.8 and 5.7±1.4 m^2g^{-1} were calculated for the nss-SO_4^{2-} at Finokalia and Erdemli, respectively. Maxima of absorption coefficient were associated with two distinct meteorological situations indicative of pollution transported from northern Europe and Saharan dust events. Saharan dust can therefore significantly contribute to both scattering and absorption of solar radiation, the latter due to its hematite content. Based on scattering and absorption measurements, an annual mean single-scattering albedo adjusted at 550 nm of 0.89±0.04 was calculated for Finokalia. Finally, radiative forcing efficiency over the sea at 550 nm induced by aerosols has been calculated for Finokalia. Radiative forcing efficiency follows a clear seasonal variation, with the lowest mean values during summer (−73W m^{-2}) and the highest during winter (−30W m^2). Using aerosol optical thickness measurements in the area, we obtain radiative forcing estimates at the top of the atmosphere ranging from −12.6 to −2.3 W m^2 for summer and winter, respectively. These values are up to five times higher than that induced by the greenhouse gases (2.4 Wm^{-2}) but opposite in sign (Vrekoussis et al., 2005).

Dry deposition and air concentration samples were collected from July 2004 to May 2005 at a suburban site in Turkey in an another study (Cindoruk and Tasdemir, 2007). A water surface sampler was used to measure directly the dry deposition flux of particulate polychlorinated biphenyls (PCBs) while a high volume air sampler was employed to collect air samples. Particulate PCB concentrations accounted for 15% of total PCBs (gas + particle phase) at the site. The overall particulate phase PCB flux ranged from 2 to

160 ng m^{-2} d^{-1} with an average of 46.3 ± 40.6 ng m^{-2} d^{-1}. Forty one PCB congeners were targeted in the samples while twenty one congeners were found to be higher than detection limits in deposition samples. Fluxes for homolog groups ranged between 0.9 (7-CBs) and 21.0 (3-CBs) ng m^{-2} d^{-1}. Measured dry deposition fluxes were lower than the ones usually reported for urban sites. Average PCB dry deposition velocity, calculated using flux values and concurrently measured atmospheric concentrations, was 1.26 ± 1.86 cm s^{-1} depended on size distribution of particles, atmospheric PCB concentrations and meteorological conditions (Cindoruk and Tasdemir, 2007).

Another study (Turkum et al., 2008) investigated the chemical composition of aerosol and rainwater samples. Samples were collected at four different locations in Turkey and were compared to investigate the relationship between aerosol and rainwater compositions. Results showed that aerosol composition could be reflected closely in rainwater composition if below-cloud processes dominate in-cloud processes. This was clearly observed for crustal elements at all stations and for most elements at the urban station. However, at rural stations there were differences in rain and aerosol that were attributed to significant contributions from in-cloud processes. Seasonal patterns observed in aerosol composition showed general agreement with the corresponding temporal variations observed in concentrations of elements in rainwater. These observations suggested that certain features of rainwater composition could be constructed if concentration data is available for aerosols. However, differences in the data observed at the different stations and among various elements or element groups showed that the composition of rainwater constructed from aerosol data could be only a crude effort. Similarities between rain and aerosol compositions were more pronounced at the urban station as compared to the rural stations. Scavenging ratios calculated using paired daily data were variable both among stations and within a single station. Long-term averaged data were found to be more reliable in calculating scavenging ratios of elements and ions at all stations (Turkum et al., 2008).

Bayraktar et al. (2010) studied the average mass concentrations of TSP, PM_{10} and $PM_{2.5}$ in Erzurum urban atmosphere at a sampling point from February 2005 to February 2006. During sampling, two low volume samplers were used and each sampling period

lasted approximately 24 hours. Kriging method was applied to the black smoke concentration data for winter seasons. Mass concentrations of TSP, PM_{10} and $PM_{2.5}$ of Erzurum urban atmosphere were measured. Meteorological factors, such as temperature, wind speed, wind direction and rainfall were typically found to be affecting PMs. Air temperature did not seem to be significantly affecting TSP and PM_{10} mass concentrations, but had a considerably negative induction on $PM_{2.5}$ mass concentrations. Combustion sourced $PM_{2.5}$ was usually diluted from the urban atmosphere by the speed of wind, soil sourced coarse mode particle concentrations were slightly affected by the speed of wind. Rainfall was found to be decreasing concentrations to 48% in all fractions and played an important role on dilution of the atmosphere. Fine mode fraction of PM showed significant daily and seasonal variations on mass concentrations. Coarse mode fractions revealed more steady variations. It was observed that fine mode fraction variations were affected by the heating in residences during winter seasons.

Kocak et al. (2010) measured water-soluble ions (Cl^-, NO_3^-, SO_4^{2-}, $C_2O_4^{2-}$, Na^+, NH_4^+, K^+, Mg^{2+},Ca^{2+}), water soluble organic carbon (WSOC), organic and elemental carbon (OC, EC) and trace metals (Al, Ca, Ti, V, Cr, Mn, Fe, Ni, Cu, Zn, Cd and Pb) in aerosol PM_{10} samples above Istanbul between November 2007 and June 2009. Source apportionment analysis using Positive Matrix Factorization (PMF) indicated that approximately 80% of the PM_{10} is anthropogenic in origin (secondary, refuse incineration, fuel oil and solid fuel combustion and traffic). Crustal and sea salt account for 10.2 and 7.5% of the observed mass, respectively. In general, anthropogenic (except secondary) aerosol showed higher concentrations and contributions in winter. Mean concentration and contribution of crustal source was found to be more important during the transitional period due to mineral dust transport from North Africa. During the sampling period, 42 events exceeding the limit value of 50 μg m^{-3} were identified. A significant percentage (91 %; n=38) of these exceedances was attributed to anthropogenic sources. Potential Source Contribution Function analysis highlights that Istanbul was affected from distant sources from Balkans and Western Europe during winter and from Eastern Europe during summer. On the other hand, Istanbul sources influenced western Black Sea and Eastern Europe during winter and Aegean and LevantineSea during summer (Kocak et al., 2010).

Another study (Theodosi et al., 2010) examined the chemical composition of aerosols over the Greater Istanbul Area. 325 (PM_{10}) aerosol samples were collected over Bosphorus from November 2007 to June 2009 and were analysed for the main ions, trace metals, water-soluble organic carbon, organic and elemental carbon. PM_{10} levels were found to be in good agreement with those measured by the Istanbul Municipality air quality network, indicating that the sampling site is representative of the Greater Istanbul Area. The main ions measured in the PM_{10} samples were Na^+, Ca^{2+} and non-sea-salt sulphates (nss-SO_4^{2-}). On average, 31% of Ca^{2+} was found to be associated with carbonates. Trace elements related to human activities (as Pb, V, Cd and Ni) obtained peak values during winter due to domestic heating, whereas natural origin elements like Al, Fe and Mn peaked during the spring period due to dust transport from Northern Africa. Organic carbon was found to be mostly primary and elemental carbon was strongly linked to fuel oil combustion and traffic. Both OC and EC concentrations increased during winter due to domestic heating, while the higher WSOC to OC ratio during summer can be mostly attributed to the presence of secondary, oxidized and more soluble organics. Factor analysis identified six components/sources for aerosol species in PM_{10}, namely traffic/industrial, crustal, sea-salt, fuel–oil combustion, secondary and ammonium sulfate.

1.2.6. Lidar Networks

It is very important to have a combinational global data of aerosols to be able to understand their temporal and spatial distribution, and the lidar networks are intended to serve this purpose. In the World, there are several networks of lidars, atmospheric observations and meteorological stations, whose objectives, approaches, missions and duties sometimes overlap or coincide, however, the number of successfully operating lidar networks are considerably low. The lidar networks show a trend to be grouped as regionally or politically. There is the plan to unite these networks under GALION (GAW (**G**lobal **A**tmosphere Watch) **LI**dar **O**bservation **N**etwork), which will be a network of contributing networks (Bösenberg and Hoff, 2008).

EARLINET's (**E**uropean **A**erosol **R**esearch **LI**dar **NET**work) goal is to create a quantitative dataset describing the aerosol vertical, horizontal, and temporal distribution,

including its variability on a continental scale to be used to validate and improve models that predict the future state of the atmosphere and its dependence on different scenarios describing economic development, including those actions taken to preserve the quality of the environment. EARLINET provides aerosol data with unbiased sampling, for important selected processes, and air-mass history, together with comprehensive analyses of these data. The objectives is reached by operating a network of stations distributed over most of Europe, using quantitative laser remote sensing to directly measure the vertical distribution of aerosols, supported by a suite of more conventional observations. A major part of the measurements is performed according to a fixed schedule to provide an unbiased statistically significant data set. Additional measurements are performed to specifically address important processes that are localised either in space or time like the Eyjafjallaöküll eruption and EARLINET provides valueable information on the eruption and the ash clouds that are spreading.

The stations of EARLINET are located in Tromsö, Norway; Athens, Thesseloniki, Oxylithos, Greece; Granada, Barcelona, Madrid, Spain; Belsk, Poland; Bilthoven, Cabauw, The Netherlands; Bucharest, Romania; Evora, Portugal; Garmisch-Partenkirschen, Maisach, Leipzig, Münschen, Hamburg, Germany; Ispra, L'Aquila, Potenza, Lecce, Napoli, Italy; Jungfraujoch, Neuchatel, Payerne, Switzerland; Liköping, Sweden; Minsk, Belarus; Sofia, Bulgaria, Palaiseau, Saint Michel, France.

EARLINET data include particle backscatter coefficient profiles (as a function of height above mean sea level) including their errors. Wavelengths include one or more out of 355 nm, 532 nm and 1064 nm. In case Raman lidars are operated, backscatter and extinction is provided, otherwise only backscatter. The latter applies for 1064 nm for all systems. Data are stored in Netcdf-Format (EARLINET web site, 2010).

MPLNET (**M**icro-**P**ulse **L**idar **NET**work) is a federated network of Micro-Pulse Lidar systems designed to measure aerosol and cloud vertical structure continuously. Long time periods required to contribute to climate change studies and provide ground validation for satellite sensors in the Earth Observing System (EOS) and related aerosol modeling efforts. Most MPLNET sites are co-located with sites in the NASA Aerosol Robotic

Network (AERONET). These joint super sites provide both column and vertically resolved aerosol and cloud data, such as: optical depth, single scatter albedo, size distribution, aerosol and cloud heights, planetary boundary layer (PBL) structure and evolution, and profiles of extinction and backscatter. MPLNET is a federated network, therefore principal investigators for individual sites may be from NASA, other US government agencies, universities, or foreign research groups. MPLNET is funded by the NASA Earth Observing System (EOS), and the NASA Radiation Sciences Program. In the past, additional funding for research cruises at sea was provided by the NASA SIMBIOS project (NASA MPLNET web site, 2010).

As it was mentioned before, in this section, EARLINET and MPLNET are the examples of succesful lidar networks which are really operational, however there are numerous other networks which can be listed to be expected to cooperate more operationally in the future: Asian Dust Network (AD-Net), The International Network for the Detection of Atmospheric Composition Change (NDACC), Commonwealth of Independent States Lidar Network (CIS-LiNET), American Lidar Network (ALINE), Regional East Aerosol Lidar Mesonet (REALM), and a geographical list of various lidar locations are mapped in Figure 1.8.

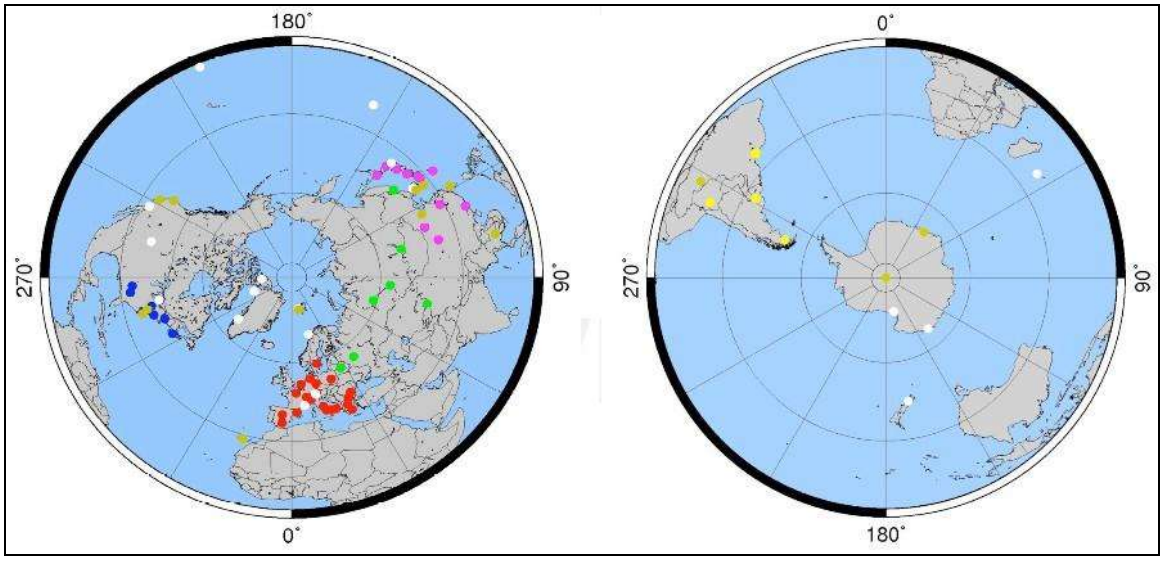

Figure 1.8. Worldwide distribution of observation networks and lidar stations.

In Figure 1.8, different lidar networks are indicated in colors: EARLINET (red, 25 stations), AD-NET (violet, 23 stations), ALINE (yellow, 7 stations), CISLiNet (green, 6 stations), MPLNET (brown, 14 stations), NDACC (white, 19 stations), REALM (blue, 7 stations) (Bösenberg and Hoff, 2008).

2. STATEMENT OF THE PROBLEM

Remote study of atmospheric aerosols is challenging because of their diversity and strong spatial and temporal variation. This makes them hard to trace, and experiment, especially with in situ techniques. Also, once the in situ sample is brought back to the laboratory from 10 kilometers of altitude, main characteristics change during the time consumed to bring it in, and the changes in temperature and pressure make that sample far different than what it was originally in its real atmospheric conditions, therefore lidar remote sensing technique is very useful. Scientifically, aerosols are one of the less known and poorly understood constituents of the atmosphere, but conversely their presence has many effects on Global climate change, through altering the radiative properties of the atmosphere. For a better and efficient study of the remote aerosols in the atmosphere, lidars have been used for a few decades, and the instrumentations for these studies have become extremely sophisticated for the last ten years.

Another important concern is, simply, it is a hazard for the human health to inhale aerosols. In the last decades, several epidemiological studies have linked adverse health effects of populations exposed to increased ambient fine (diameter < 2.5 μm) and ultrafine (diameter <180 nm) particle concentrations (Peters and Pope, 2002; Schulz et al., 2005). Particle size determines its deposition site and fraction in human lungs and its potential translocation to other target organs (Oberdorster, 2003; Kreyling et al., 2006).

Particle toxicity studies have also linked individual particle chemical components with different adverse health effects. Organics and transition metal PM components have been identified as capable of inducing proinflammatory effects in the lung due to their ability to produce oxidative stress (Saldiva et al., 2002). Polar organic compounds such as quinones can act as catalysts to produce reactive oxygen species (ROS) directly whereas polycyclic aromatic hydrocarbons (PAHs) can induce oxidative stress indirectly, through biotransformation to generate redox active quinones (Ning and Sioutas, 2009). One other concern about the aerosols is that they can carry bacteria and viruses, so depending on the

deposition site in the body, harmful organisms can reach, harbor and infect many vital organs.

Atmosphere over Turkey have not been studied well enough before, especially, to our knowledge, there is insufficient data about the aerosol parameters and water vapor content of the atmosphere over Turkey. However, through Europe and USA and in some Asian countries (Koreas, China, Japan, Russian Federation) there have been ongoing atmospherical studies and some lidar networks. The location of Turkey is very important because of being close to one of the major contributors of global dust load, Sahara Desert, therefore an investigation of the temporal and spatial distribution of aerosols and their microphysical properties carry outmost importance.

Gebze is chosen for the installation of this lidar for the study of natural and anthropogenic aerosols for two reasons: TUBITAK MRC is located in Gebze and also due to the fact that Gebze's location is perfect for the study of aerosols. First of all it is one of the most industrialized parts of Turkey, therefore large amounts of anthropogenic aerosols are present in the vicinity. Gebze is in Northwest Turkey and it is on the route of the Sahara dust which reaches Europe, therefore data from Turkey has great significance to the lidar networks especially of Europe, EARLINET.

Thus, the goal of presented study is development of the multiwavelength Mie-Raman lidar, to perform the regular lidar measurements in Turkey and to evaluate the vertical distribution of tropospheric particle parameters for different seasons and meteorological conditions. For the effectively retrieval of atmospheric particulate matter parameters, a lidar was designed, developed, installed and succesfully operated between May 2009 to June 2010. Three backscattering and two extinction coefficients ($3\beta + 2\alpha$) are needed for the retrieval in such a lidar system. One more difficulty was the programming of the custom made software for the complex mathematics behind the retrieval of particle parameters. For these tasks, a joint project between Materials Institute of TUBITAK Marmara Research Center and Physics Instrumentation Center (PIC) of Russian Academy of Sciences (RAS) was proposed, accepted, succesfully managed, and fruitful results were obtained.

3. METHODOLOGY

Lidar systems are highly sophisticated and each lidar is designed according to what it will measure. The designed systems are called by the methodology of their principle such as differential absorption lidar (DIAL), Raman lidar, fluorescence lidar, doppler lidar and etc.

In this Methodology chapter, first the mathematical background for lidar to study aerosols will be described. The solution of lidar equation to retrieve aerosol backscattering and extinction coefficients will be explained. There are two existing methods to achieve this task: Klett and Raman methods, and they will be both explained in detail here. To retrieve particle parameters, there are also two methods: Inversion with regularization and principle component analysis. Custom programmed softwares which are designed during this thesis to calculate these aerosol backscattering and extinction coefficients and aerosol microphysical parameters in an efficient way.

After the theoretical explanation of the lidar system, the experimental setup of the system which was designed, developed and operated at TUBITAK, MRC will be explained. The technical properties of the lidar system will be listed including the supplier companies from which the parts of the system were acquired. Also data treatment, noise elimination and the methodology of data timings will be explained in this Methodology chapter. Technical drawings of the lidar system, the telescope, the main mirror of the telescope and the spectrum analyzing system can be found in Appendix B.

3.1. Theoretical Background for Lidar Data

3.1.1. Solving Lidar Equation to Get Aerosol Backscattering and Extinction Coefficients

The measurement of the elastic backscatter signal at 355 nm and of the Nitrogen inelastic backscatter signal at 387 nm permit the determination of the extinction and backscatter coefficients independently of each other and thus, of the extinction to backscatter ratio, which is also called as lidar ratio. The particle extinction coefficient is determined from the inelastic backscatter signal profile, while the particle backscatter coefficient is derived from the ratio of the elastic backscatter to the Raman signal, as is usual in the combined lidar technique (Ansmann et al., 1992).

Thus, the basic lidar equation for elastic backscatter signal is as follows:

$$P_{\lambda_L}(z) = P_{0,\lambda_L} A_{\lambda_L} \frac{\beta^m_{\lambda_L}(z) + \beta^a_{\lambda_L}(z)}{z^2} \exp\left(-2\int_0^z \left(\alpha^m_{\lambda_L}(z') + \alpha^a_{\lambda_L}(z')\right) dz'\right) \qquad (3.1)$$

where P_{0,λ_L} is laser energy at wavelength λ_L, A_{λ_L} is the system constant at λ_L, $\beta^m_{\lambda_L}(z)$ is the backscattering for molecular atmosphere (N_2, O_2 and other gases), $\beta^a_{\lambda_L}(z)$ is aerosol backscattering, z is distance, $\alpha^m_{\lambda_L}(z)$ is the extinction for molecular atmosphere and $\alpha^a_{\lambda_L}(z)$ is the aerosol extinction.

For the inelastic Raman backscatter signal, the following equation can be given:

$$P_{\lambda_R}(z) = P_{0,\lambda_R} A_{\lambda_R} N(z) \frac{\sigma_{\pi,\lambda_R}}{z^2} \exp\left(-\int_0^z \begin{pmatrix} \alpha^m_{\lambda_R}(z') + \alpha^a_{\lambda_R}(z') \\ +\alpha^m_{\lambda_L}(z') + \alpha^a_{\lambda_L}(z') \end{pmatrix} dz'\right) \qquad (3.2)$$

where $\alpha^m_{\lambda_R}(z)$ is the extinction coefficient for molecular atmosphere at Raman wavelength λ_R, $N(z)$ is the concentration of molecular Nitrogen, σ_{π,λ_R} is the cross section at backward direction of molecular Nitrogen and Oxygen, $\alpha^m_{\lambda_R}(z)$ is the extinction coefficient for

molecular atmosphere at Raman wavelength λ_R, $\alpha^a_{\lambda_R}(z)$ is the extinction coefficient for aerosol at Raman wavelength λ_R, $\alpha^m_{\lambda}(z)$ is the extinction coefficient for molecular atmosphere at laser radiation wavelength, and $\alpha^a_{\lambda}(z)$ is the extinction coefficient for aerosol at laser radiation wavelength.

Angstrom equation allows the quick calculation of average particle size or the mean radius of the particles. Equation is as follows:

$$\alpha^a_{\lambda_R} = \alpha^a_{\lambda_L}\left(\frac{\lambda_L}{\lambda_R}\right)^k \tag{3.3}$$

where k is the angstrom coefficient. Typical values for k would be approximately 4 for small particles, 0 for large particles and minus values for clouds.

There are two suggested methods for the solution of lidar equation, Klett and Raman methods. Klett method (Klett, 1981) is based on the assumption of a constant lidar ratio:

$$\frac{\beta(z)}{\alpha(z)} = P \tag{3.4}$$

Klett solution of lidar equation in three steps is as follows:

$$P_{\lambda_L}(z) = P_{0,\lambda_L} A_{\lambda_L} \frac{\beta^m_{\lambda_L}(z) + \beta^a_{\lambda_L}(z)}{z^2} \exp\left(-2\int_0^z \left(\alpha^m_{\lambda_L}(z') + \alpha^a_{\lambda_L}(z')\right)dz'\right) \tag{3.5a}$$

$$z^2 P_{\lambda_L}(z) = P_{0,\lambda_L} A_{\lambda_L} \left(\beta^m_{\lambda_L}(z) + \beta^a_{\lambda_L}(z)\right) \exp\left(-2\int_0^z \left(\alpha^m_{\lambda_L}(z') + \alpha^a_{\lambda_L}(z')\right)dz'\right) \tag{3.5b}$$

$$\ln\left(z^2 P_{\lambda_L}(z)\right) = \ln\left(P_{0,\lambda_L} A_{\lambda_L} \left(\beta^m_{\lambda_L}(z) + \beta^a_{\lambda_L}(z)\right)\right) - 2\int_0^z \left(\alpha^m_{\lambda_L}(z') + \alpha^a_{\lambda_L}(z')\right)dz' \tag{3.5c}$$

So, the solution of equation (3.5) can be denoted as follows:

$$S(z) = \ln(z^2 P(z)) \tag{3.6}$$

This expression is the logarithm of lidar equation in a different notation and here, another notation $S = S(z)$ and $S_0 = S(z_{ref})$ where z_{ref} is reference distance or distance where

atmosphere contains only molecules and does not contain any aerosols. If the equation is rewritten and solved by combining the reference distance concept, it is as follows:

$$S - S_0 = \ln\left[\beta(z)/\beta(z_0)\right] - 2\int_{z_0}^{z} \alpha(z')dz' \tag{3.7}$$

$$\frac{dS}{dz} = \frac{1}{\beta(z)}\frac{d\beta(z)}{dz} - 2\alpha(z) \tag{3.8}$$

The differential equation (3.8) has the next solution:

$$\alpha(z) = \frac{\exp\left[(S - S_0)\right]}{\alpha_0^{-1} - 2\int_{z_0}^{z} \exp\left[(S - S_0)\right]dz'} \tag{3.9}$$

where $\alpha(z)$ is the aerosol extinction coefficient. If equation (3.9) is substituted in equation (3.4) equation for the backscattering coefficient can be obtained:

$$\beta(z) = P^m \alpha^m(z) + P^a \alpha^a(z) \tag{3.10}$$

where $\beta(z)$ is the backscattering coefficient, $P^m = \frac{3}{8\pi}$ is the molecular lidar ratio and P^a is aerosol lidar ratio.

Particle extinction coefficient can be obtained from the nitrogen Raman signal by the use of Raman method (Ansmann, 1992).

$$\alpha_{\lambda_L}^a(z) = \frac{\frac{d}{dz}\left(\ln\frac{N(z)}{P_{\lambda_R}(z)z^2}\right) - \alpha_{\lambda_R}^m(z) - \alpha_{\lambda_L}^m(z)}{1 + \left(\frac{\lambda_L}{\lambda_R}\right)^k} \tag{3.11}$$

where particle scattering is assumed to be proportional to:

$$\alpha_{\lambda_R}^a = \alpha_{\lambda_L}^a \left(\frac{\lambda_L}{\lambda_R}\right)^k \tag{3.12}$$

The particle backscatter coefficient $\beta^a_{\lambda_L}(z)$ can be determined by using both elastically and inelastically backscattered signals. Two measured signal pairs $P_{\lambda_L}(z)$ and $P_{\lambda_R}(z)$ at height z and at a reference height z_{ref} are needed.

$$\beta^a_{\lambda_L}(z) = -\beta^m_{\lambda_L}(z) + \frac{P_{\lambda_R}(z_{ref})P_{\lambda_L}(z)N(z)}{P_{\lambda_L}(z_{ref})P_{\lambda_R}(z)N(z_{ref})}\beta^m_{\lambda_L}(z_{ref}) \times \frac{\exp\left(-\int_{z_{ref}}^{z}\alpha^m_{\lambda_R}(z') + \alpha^a_{\lambda_R}(z')dz'\right)}{\exp\left(-\int_{z_{ref}}^{z}\alpha^m_{\lambda_L}(z') + \alpha^a_{\lambda_L}(z')dz'\right)} \quad (3.13)$$

where $P_{\lambda_R}(z_{ref})$ is the power of lidar signal at distance z_{ref} for the Raman wavelength, $P_{\lambda}(z_{ref})$ is the power of lidar signal at distance z_{ref} for the elastic wavelength and $N(z_{ref})$ is the concentration of molecular Nitrogen at distance z_{ref} for the Raman wavelength.

3.1.2. Solving the Inverse Problem to Retrieve Particle Microphysical Parameters

The inverse problem to retrieve the particle microphysical parameters from lidar data is formulated in the form of Fredholm integral equations (Veselovskii et al., 2002). The following equations give the aerosol backscatter and extinction coefficients:

$$\beta_i = \int_0^\infty K_\beta(m, r, \lambda_i) f(r)\, dr \quad (3.14)$$

$$\alpha_i = \int_0^\infty K_\alpha(m, r, \lambda_i) f(r)\, dr \quad (3.15)$$

where r is the particle radius, $m = m_R - im_I$ denotes the complex particle refractive index, and as a complex number with real part m_R and imaginary part m_I, λ_i is the wavelength, $K_\beta(m,r,\lambda_i)$ and $K_\alpha(m,r,\lambda_i)$ are the backscatter and extinction kernel functions, which can be calculated by means of Mie theory in the case of particles with spherical shape (Bohren and Huffmann, 1983). The term f(r) is the PSD expressed as the number of particles per unit volume between r and r + dr. So, formulas (3.14) and (3.15) can be written as a generalized integral equation:

$$g_j(\lambda_i) = \int_{r_{min}}^{r_{max}} K_j(m, r, \lambda_i)\, f(r)\, dr \tag{3.16}$$

where j is α or β (extinction or backscatter coefficients), $g_j(\lambda_i)$ are the optical data at wavelength λ_i, and r_{min} and r_{max} denote the lower and the upper limits of the particle radii (Veselovskii et al., 2002).

Equation (3.16) does not have any analytical solution, therefore detailed description of the following method of inversion with regularization is given in other studies (Twomey, 1977; Tikhonov and Arsenin, 1977). In this approach, equation (3.16) can be rewritten in the following form:

$$g_p^{\delta} = \int_{r_{min}}^{r_{max}} K_p(m, r)\, f^{\delta}(r)\, dr \tag{3.17}$$

where g^{δ}_p are the distorted optical data (α or β), $f^{\delta}(r)$ is the corresponding function that describes the PSD and p = j, λ. The integral of equation (3.17) can be approximated by a sum, which consists of the following superposition of base functions $B_j(r)$:

$$f^{\delta}(r) = \tilde{f}^{\delta}(r) + \varepsilon = \sum_j C_j B_j(r)\, dr + \varepsilon \tag{3.18}$$

The term $\tilde{f}^{\delta}(r)$ is an approximated solution of equation (3.18), ε is the error in the solution, and C_j are constants or so-called weight coefficients. $B_j(r)$ are B-spline functions, which in this case have a triangular shape (Veselovskii et al., 2002). Mentioned functions are given by the following expression:

$$B_j(r) = \begin{cases} 0 & ;\ r < r_{j-1} \\ 1 - \dfrac{r_j - r}{r_j - r_{j-1}} & ;\ r_{j-1} < r \le r_j \\ 1 - \dfrac{r - r_j}{r_{j+1} - r_j} & ;\ r_j < r \le r_{j+1} \\ 0 & ;\ r > r_{j+1} \end{cases} \qquad j = 1..N \tag{3.19}$$

where r_0 and r_{N+1} limit the range of the size within which the inversion is performed. In the following equation, this range is denoted as the inversion window. Additionally in equation (3.19), N is the number of B-spline functions and the points r_j are equally separated inside the interval $[r_0, r_{N+1}]$. In this algorithm N always coincides with the number of optical data (Veselovskii et al., 2002).

Using equations (3.18) and (3.19), the optical data can be rewritten as a linear combination:

$$g_p^{\delta} = \sum_{j=1}^{N} A_{pj}(m)\, C_j + \varepsilon^{\nabla}, \tag{3.20}$$

where A_{pj} and ε^{∇} are calculated from the kernel functions, the base functions, and the errors as:

$$A_{pj}(m) = \int_{r_{min}}^{r_{max}} K_p(m, r)\; B_j(r)\, dr \tag{3.21}$$

$$\varepsilon_p^{\nabla} = \int_{r_{min}}^{r_{max}} K_p(m, r)\; \varepsilon(r)\, dr \tag{3.22}$$

By writing the optical data as a vector $\bar{g}^{\delta} = [g_p^{\delta}]$, the weight coefficients as a vector $\bar{C} = [C_j]$, the errors as a vector $\bar{\varepsilon}^{\nabla} = [\varepsilon_p^{\nabla}]$, equation (3.20) can be rewritten as the following vector-matrix form:

$$\bar{g}^{\delta} = A\,\bar{C} + \bar{\varepsilon}^{\nabla}, \tag{3.23}$$

where the matrix $A = [A_{pj}]$ is the so-called weight matrix, the elements of which are calculated from equation (3.21) (Veselovskii et al., 2002).

The solution of equation (3.23) then gives the vector of weight coefficients as:

$$\bar{C} = A^{-1}\; \bar{g}^{\delta} + \bar{\varepsilon}, \tag{3.24}$$

where $\bar{\varepsilon} = -A^{-1}\; \bar{\varepsilon}^{\nabla}$ is the error vector and A^{-1} is the inverse of the matrix A. Therefore, the problem of inversion becomes a problem of determination of weight coefficients C_j.

Henceforth, in general, the simple solution of equation (3.24) is unstable. As a consequence, it is not possible to reconstruct the exact solution for f, so this instability may be suppressed by regularization. The idea behind it is illustrated by writing equation (3.14) as the following operator form (Twomey, 1977):

$$\hat{A}\ f\ =\ g \tag{3.25}$$

If instead the exact value of g the approximate value g^{δ} is known, which means that the norm in Euclidean space:

$$\left\| g - g^{\delta} \right\|_{E}\ \leq\ \delta \tag{3.26}$$

The essence of the regularization technique lies in the construction of an algorithm which determines the element $\tilde{f}^{\delta}$ appropriate to the pair (g^{δ}, δ), such that the convergence $\tilde{f}^{\delta} \xrightarrow{\delta \to 0} f$ is realized (Veselovskii et al., 2002).

According to Tikhonov (1977) the function $M^{\gamma}[f, g^{\delta}]$ is defined as:

$$M^{\gamma}[f, g^{\delta}] = \left\| \hat{A} f - g^{\delta} \right\|_{E}^{2} + \gamma \Gamma(f), \tag{3.27}$$

where $\rho' = \left\| \hat{A} f - g^{\delta} \right\|_{E}^{2}$ is the discrepancy, γ is a non-negative regularization parameter or so-called Lagrange multiplier and Γ (f) is a penalty term stabilizing the inverse problem.

The solution of equation (3.25) may then be found from the minimization of $M^{\gamma}[\tilde{f}_{\gamma}^{\delta}, g^{\delta}] \longrightarrow \min$. In matrix-vector form it is written as:

$$A^{T} A\ \overline{C} - A^{T} g^{\delta}\ + \gamma\ H = 0 \tag{3.28}$$

So finally the weight coefficients can be derived from the following relation:

$$\overline{C} = (A^{T} A + \gamma\ H)^{-1}\ A^{T}\ g^{\delta} \tag{3.29}$$

The main difference between equations (3.24) and (3.29) is the so-called smoothing matrix (Twomey, 1977), which describes the physical constraint that size distributions do not show large oscillations within small particle size ranges. The specific form of the matrix influences the maximum difference between the weight factors of successive base functions. This matrix describes the change of the weight factors of three successive base

functions, which is equivalent to smoothness of the solution in the second derivative (Dubovik et al., 2000).

The Lagrange multiplier γ, which can take values from 0 to ∞, determines the degree of smoothing, or the strength of the smoothing matrix. There are different methods for the choice of the Lagrange multiplier, the most common of which are the method of maximum likelihood, the Bayesian approach, the method of generalized cross-validation and the minimum discrepancy principle. Here, the method of minimum discrepancy is chosen, because this criteria is the most simple and natural one (Veselovskii et al., 2002). The main problem in the application of the method of minimum discrepancy is the necessity to know a priori the expected error in the data. Otherwise the smallest discrepancy is observed for $\gamma \to 0$, and in this case the solutions oscillate from $-\infty$ to $+\infty$. For this situation, this method can be modified because in fact, the solutions have to be positive. The possibility of non-negativity constraints was considered before (Dubovik et al., 2000). In the modified discrepancy ρ only modules $|f^{\delta}|$ for which $\rho = \|A|f^{\delta}| - g^{\delta}\|$ minimizes the function (3.23) are accepted as solutions. For small γ the modified discrepancy $\rho \to \infty$, with the increase of γ the value of ρ reduces and the solution $f^{\delta} \to f$. For large γ the modified discrepancy ρ coincides with the classical discrepancy ρ' introduced in (3.23) (Veselovskii et al., 2002).

In data analysis the most important is the relative error, so the discrepancy is normalized into the form:

$$\rho \equiv \frac{1}{N} \sum_i \frac{\left\| g_i^{\delta} - A\left|f^{\delta}\right| \right\|}{g_i^{\delta}} \tag{3.30}$$

The value of γ depends on the inversion interval $[r_{min}, r_{max}]$, the optical data errors δ, and the complex refractive index of the particles. The choice of solution in this approach includes the following steps:

- The values of r_{min}, r_{max} and the complex refractive index $m = m_R - im_I$ are varied in the intervals Δr_{min}, Δr_{max}, Δm_R, Δm_I. R_{min} ranges from 0.05 to 0.5 μm. R_{max} usually ranges from 0.1 to 1 μm, but for simulation of big particles retrieval this range could be

increased up to 10 μm. At the preliminary stage of calculation the step width of the variation of R_{min} and R_{max} is 0.05 and 0.1 μm, respectively. When the approximate locations of $R_{min.}$and R_{max} are established, the calculations are repeated with a step width of 0.01 - 0.02 μm within a smaller interval. Thus, usually several hundred inversion windows are considered. As a consequence a better resolution of the investigated particle size distribution compared to the rather limited set of 50 windows used earlier (Müller et al., 1999) is achieved. The real part m_R ranges from 1.1 to 1.8 and the imaginary part m_I from 0 to 0.1. After preliminary estimations the range is decreased and the calculations are performed with a step width of 0.01.

- For every value of r_{min}, r_{max}, m_R, m_I within the chosen intervals and for the set of γ, the program calculates the solution $\tilde{f}_{\gamma}^{\delta}$ with the use of Eq. (29) and Eq. (18). The set of γ is determined as $\gamma = 2^K 10^{-b}$, where K = 1, 2…25 is the calculation number. Parameter b is chosen between 20 and 28, to achieve the minimization of function inside the calculation interval. The integration step in equation (3.21) is usually chosen to be 0.002 μm.

- For every solution the discrepancy $\rho(\gamma)$ is determined. The $\tilde{f}_{\gamma}^{\delta}$ corresponding to the minimum of $\rho(\gamma)$ is considered to be the solution of equation (3.17).

The use of the modified discrepancy allows determining the Lagrange multiplier without initial guesses about data errors. If the Lagrange multiplier is chosen too large, the solution will be over smoothed, and for small γ it will oscillate. It should be mentioned also, that though for the calculation of modified discrepancy, only positive values $|f^{\delta}|$ are used, the solutions f^{δ} themselves may contain the negative oscillations (Veselovskii et al., 2002).

Basically, since the lidar system is the sole instrument to monitor the aerosol parameters in detail without a real contact, which can disturb the chemical and physical characteristics of the aforementioned particles, there is a need to construct such a system which can observe, spatially and temporally monitor and follow the aerosol parameters

with certainity. For this purpose, a multiwavelength Mie-Raman lidar was designed, developed, installed and operated for a certain amount of time to supply this need for the study of variations of tropospheric aerosols and their microphysical properties. This study covers a period starting from Spring 2009 to summer 2010, which actually is an important aerosol load period.

3.1.3. Retrieval of Particle Microphysical Parameters Using Principle Component Analysis

To be able to get the vertical profiles of the particle microphysical parameters from the aerosol backscattering and extinction coefficients measured by a Raman lidar at multiple wavelengths, inversion with regularization technique is used, however, principal component analysis (PCA) technique is a very new and efficient technique to retrieve the parameters. The below comparison of the two techniques demonstrates that the integral particle parameters, like volume density, effective radius and the complex refractive index retrieved with both techniques are in agreement. Meanwhile, PCA method is faster and more tolerant to the errors in input data, thus it may be preferable when large amounts of lidar data must be managed. The developed PCA algorithm was applied to the data acquired during measurements in the Summer of 2009. The 3β + 2α lidar data sets were inverted to evaluate the temporal variation of vertical profiles of the particle parameters.

The aerosol extinction (α) and backscattering coefficients (β) are related to the particle size distribution (PSD) $\frac{dV}{d\ln r}$ via integral equations as follows:

$$g_p = \int_{\ln r_{min}}^{\ln r_{max}} K_p(m,r)\frac{\partial V(r)}{\partial \ln r} d\ln r \quad p = (i,\lambda_k) = 1,..,N_0 \tag{3.31}$$

where index p labels the type of optical data (i) and wavelengths λ_k; $K_p(m,r)$ is the corresponding kernel depending on complex refractive index $m = m_R + i{\cdot}m_I$ and particle radius $r \in [r_{min}, r_{max}]$.

It can be shown that any particle integral property P (for example, volume and surface density), can be estimated as (Donovan and Carswell, 1997; De Graaf et al., 2008; De Graaf et al., 2009):

$$\mathrm{P} = \mathbf{w}^{\mathrm{T}}\mathbf{K}^{\mathrm{T}}\mathbf{C}^{-1}\mathbf{g} \tag{3.32}$$

where $\mathbf{K}$ is a matrix formed by volume kernels discretised at radii bins $r_{\min} = r_1, \ldots, r_{\mathrm{N}} = r_{\max}$ with elements $K_{pq} = K_p(m, r_q)$, $q = 1 \ldots \mathrm{N}$; $\mathbf{C} = \mathbf{K}\mathbf{K}^{\mathrm{T}}$ is covariance matrix and $\mathbf{K}^{\mathrm{T}}$ is the transposed matrix $\mathbf{K}$ The weighting vector $\mathbf{w}$ consists of the elements $w_q = 1$ for volume and $w_q = 3/r_q$ for surface density.

Equation (3.32) can be used if the refractive index of aerosol m is known. Unfortunately the tropospheric aerosols are characterized by high temporal and spatial variability of the refractive index, so it is desirable to get information about m from the lidar data themselves. The way to do it was suggested in (De Graaf et al., 2008; De Graaf et al., 2009).

Following that way, one optical data g_p (extinction or backscattering coefficient) is omitted and estimated as $\tilde{g}_p$ from the solution obtained with the rest of the kernels. Then the difference ε, or so called discrepancy, between measured and recomputed optical data is determined as:

$$\varepsilon = \frac{\sum_{p}^{N_0} \left| g_p - \tilde{g}_p \right|}{N_0} \tag{3.33}$$

Since there is no a priori knowledge about particle size and refractive index we find the discrepancy ε for all predefined values of $r_{\min}$, $r_{\max}$, m_{R} and m_{I} lying in respective intervals [0.05 μm, 0.15 μm], [0.5 μm, 10.0 μm], [1.33, 1.6] and [0.00, 0.02]. Usually total number of predefined combinations does not exceed $\mathrm{N_T} = 3000$. The solutions are ranged in accordance with their discrepancy from minimal to maximal To get the final solution normally 10-20 % of individual solutions are averaged.

3.2. Development, Installation and Operation of the Lidar

For the purpose of the investigation of the spatial and temporal distribution, and microphysical parameters of tropospheric aerosols, a multiwavelength Mie-Raman lidar was designed, developed and installed at TUBITAK Marmara Research Center, Materials Institute, K09 Laser Spectroscopy Laboratory during 2008-2009. Gebze was chosen as the site of measurements because of the location of TUBITAK MRC, and at the same time, the location proved to be a good site to observe both natural and anthropogenic aerosols present at the vicinity.

The lidar system was designed by a team of Turkish scientists, however various optical, electronic and mechanical parts were purchased from the international supplier companies, and some mechanical parts were built in TUBITAK MRC's Mechanical Workshop.

3.2.1. The Structure of the Lidar

According to the Turkish and Russian engineering designs, the telescope was built at TUBITAK MRC, and the optical components of 40 cm diameter main mirror and the elliptical mirror of the telescope, along with the off axis collimator mirrors, primary and secondary transmitting mirrors were manufactured in highly specialized Russian companies. The angle adjustable stand for the lidar system was designed, developed and built in Russia. The off-axis collimator for expanding and collimating the laser beam was built at TUBITAK MRC. The transmitting unit, QUANTEL BrilliantB Q-switched Nd:YAG laser emitting 855 / 400 / 240 mJ in a pulse at 1064 / 532 / 355 nm wavelengths was purchased from laser manufacturing company, QUANTEL of France. The spectrum analyzing unit was designed and built at TUBITAK MRC and the mirrors for the unit were purchased from various Russian companies. The lidar system contains 7 channels to receive optical data to be converted into electronic signal. The housing tubes for the PMT's were designed and built at TUBITAK MRC; the dichroid mirrors inside the 5 PMTs were purchased from Russia, and the Hamamatsu R194 analog-to-digital convertors (ADC) were purchased from the company HAMAMATSU in Japan. The remaining two channels

of the spectrum analyzer contain one Hamamatsu H7422 photo sensor module from HAMAMATSU and one NIR enhanced avalanche photodiode from LICEL, Germany. The PS310 high voltage power supplies for the PMT's were purchased from STANFORD Electronics Inc. in Florida, USA. The RG-174 coaxial signal cables connecting the spectrum analyzer to the optoelectronic data processing unit were purchased from Turkey. Data processing unit, transient recorder LICEL TR40-160 along with the necessary software was purchased from LICEL in Germany.

Laser beam is hazardous for human eye, so for the eye safety of the airplane and helicopter operators, a Furuno 1715 model radar was purchased and installed in the field of view of the telescope with plus and minus 25 degrees, so that if an aircraft enters into the air space near the laser beam, the laser shuts itself until the aircraft leaves the air space. A Tektronix TDS2002 oscilloscope was purchased from USA for testing various electronic components of the lidar system and for calibrating the laser beam.

The software which is necessary for the data treatment and interpretation for the lidar system data was developed by Russian and Turkish scientists during the project. Technical drawings of the lidar system can be found in Appendix B. The lidar in operation is illustrated in Figure 3.1.

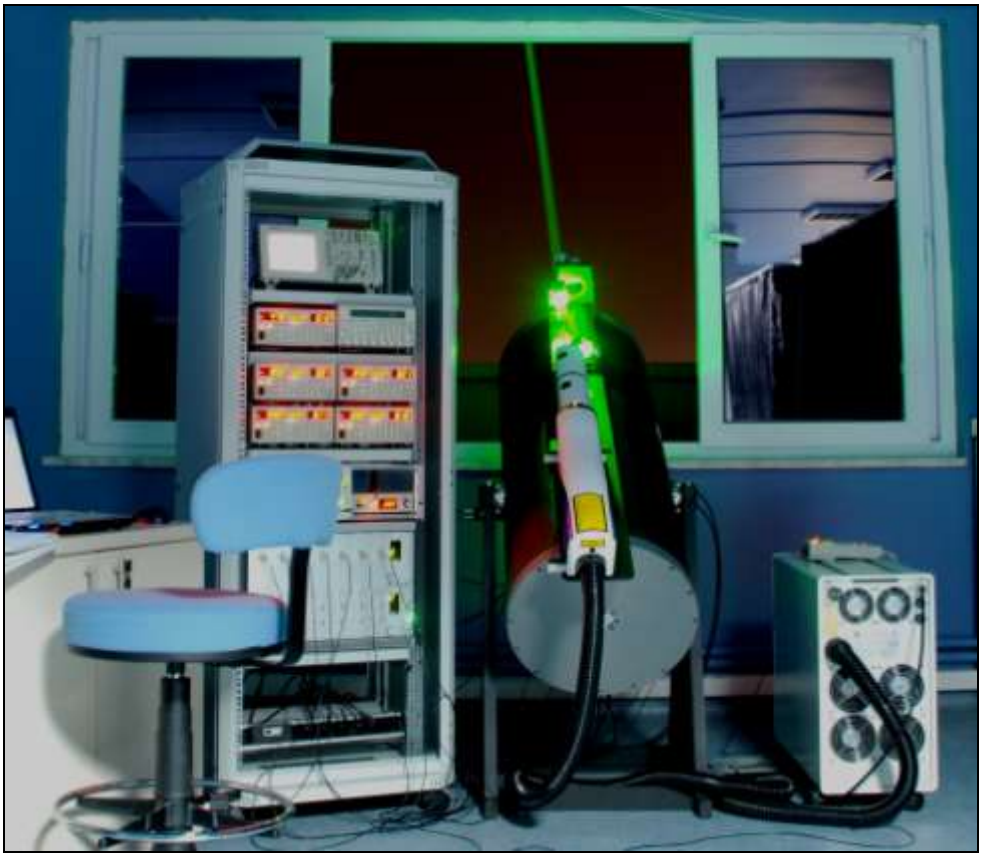

Figure 3.1. Lidar in operation.

In Figure 3.1, the lidar system can be seen in operation. From left to right, the operator seat and the computer, electronic components of the system mounted on a shelved electronic rack, laser mounted on the telescope and on the right bottom, the cooling unit and remote operating unit of the laser can be seen. Laser beam appears as green (532 nm) however, there are actually 2 more wavelengths (355 and 1064 nm) within this beam, which are ultraviolet and infrared respectively, therefore not visible.

When all the components were ready, the team of Turkish and Russian scientists started the challenging job of putting everything together. After the mirrors of the telescope were installed, it was connected to the stand. The laser was tested separately and then connected over the telescope and an additional stand needed to be cut for a stable connection. The off axis collimator was also fixed on the telescope and the laser beam was calibrated to pass through the various optical elements. Spectrum analyzer was installed on

the bottom part of the telescope and calibration was successfully perfected. PMT's were connected to the spectrum analyzer and their power supply cables and signal cables are connected to the power supply units and transient recorder, respectively. Transient recorder was connected to a computer and the triggering cable was connected to the laser. All the electronic equipment were installed in shelved rack for putting equipment together and for eliminating problems which might arise by dust.

The system was tested and operated and on May 13, 2009 at 20:55, the first laser beam in Turkey, for the study of atmospheric aerosols was sent by the lidar team of the K09 Laser Spectroscopy laboratory, into the atmosphere. The installation of the lidar at TUBITAK MRC was a tedious but a precise operation and the measurements of aerosol parameters were made possible after this task was successfully completed. The pictures from the installation process can be found in Appendix C.

3.2.2. Data Acquisition

The data saved by the computer sent by the Licel transient recorder, is raw data. Recorder obtains three extinction coefficients and two backscattering coefficients. However, it has high resolution that can be switched to 3.75 m, 7.5 m, 15 m, and 30 m resolution levels. This investigation deals with the tropospheric aerosols, therefore the most interesting part of the atmosphere which is the subject matter of this thesis is the first 10 km altitude which contains the desert dust and industrial aerosols. Especially at the planetary boundary layer (PBL), interesting aerosol and water vapor mixing events occur. For this reason, the lidar system was inclined with 22-30 degrees with the horizontal axis, so that the laser beam stays inside the troposphere for a longer time to obtain higher resolution data and more information. To be able to calculate the real height of the aerosol layers, following formula can be used:

$$H = d \, \mathrm{Sin}\theta + H_i \qquad (3.34)$$

where d is the distance from the lidar to the aerosol, θ is the sounding angle and H_i is the altitude of lidar sounding site which is about 223 m.

Starting from May 2009, through Summer and Autumn of 2009 and Spring 2010, many measurements were made. The measurements started approximately one hour before sunset and continued until one hour after sunrise, covering a 9 to 10 hours operation to have better averaged data. The measurements were carried through approximately 12 months on a twice per week basis, however, there were some disturbances. The meteorological conditions did not permit to complete the schedule, especially in Winter. Aerosol lidar principle depends on backscattering and extinction by aerosols, so if there are conditions which does not permit this, data could not be obtained, therefore on days with rain, fog, low clouds and mist, the obtained data is too noisy to process, thus on such days, no measurements could be made. Also, since laser applications carry a fire hazard and since safety is a significant issue in this instrument, an operator had to be nearby the lidar system while on operation.

One other problem that had to be dealt with, was the noise. Typically, in these kinds of multiwavelength lidar setups, there are two kinds of noise; electrical and atmospheric. Electrical noise can have various reasons. Lidar consists of mechanical and many electronical and optoelectronical parts, most of which have their own power supplies to be able to function. Also the signal is carried through coaxial signal cables and fiber optic cables. To eliminate the electronic noise, before and after the measurements which lasts for 9 -10 hours of lidar operation, the system was run for one minute by closing the spectrum analyzer of the telescope with a lid. Thus, the acquired one minute of data consists of only the noise but nothing from the atmosphere. Those one minute data before and after the measurements were averaged, and then subtracted from the whole data to be able to obtain data without electrical noise.

The other type of noise comes from the sky background, various reflections, scatters and equipment malfunction. To be able to eliminate this atmospheric noise, the signal that is coming from the altitudes between 50 to 60 kilometers are selected in the data set. There are no aerosols at that region of the atmosphere, but still there is a weak background signal. The intensity of the signal between those altitudes are selected, averaged and subtracted from the whole data set to obtain data without atmospheric noise. Thus, the developed lidar system was capable of calculating aerosol backscattering and

extinction coefficients to retrieve the particle microphysical parameters. During this research, first time in literature, the retrieval of temporal variations of aerosol microphysical parameters was achieved, and in the next chapter, these will be discussed in detail.

4. RESULTS AND DISCUSSION

This chapter includes the results obtained during this investigation of the spatial and temporal variations of aerosol backscattering and extinction coefficients and aerosol microphysical parameters. Custom programmed softwares compute the scattering coefficients from raw recorded Licel data and determine the aerosol microphysical parameters at selected heights from this data. Measurement of water vapor mixing ratio allowed to show the variation of this significant parameter. Another approach, new to literature, the retrieval of particle parameters using principle component analysis (PCA) is also used to compute the parameters in a time-series as three dimensional color maps. This so-called PCA approach proved to be very useful and in accordance with the regularization method. The ash particles from the eruption of the Iceland volcano, Eyjafjallaöküll in 2010 Spring were detected, and the parameters of the particles were retrieved and discussed as a case study towards the end of this chapter.

As it was mentioned earlier in the Methodology chapter of this thesis, the most important period to observe the aerosols for Gebze area is the late Spring and Summer months, from May through August. Therefore, the results in this thesis mostly cover this period, which started in May 2009 and continued until Summer 2010 with sporadical measurements on some certain events like dirt rains and dust fronts in all four seasons. However, in Winter, the number of measurements out of which fruitful results can be obtained is fairly low. Lidar consists of parts some of which are expensive and wear away in time, therefore to have a continuous monitoring of the atmosphere is not feasable at the moment. Figure 4.1 shows the first colormap, which is a three dimentional figure illustrating distance, time and signal intensity on a single picture, from the atmosphere over Turkey in literature.

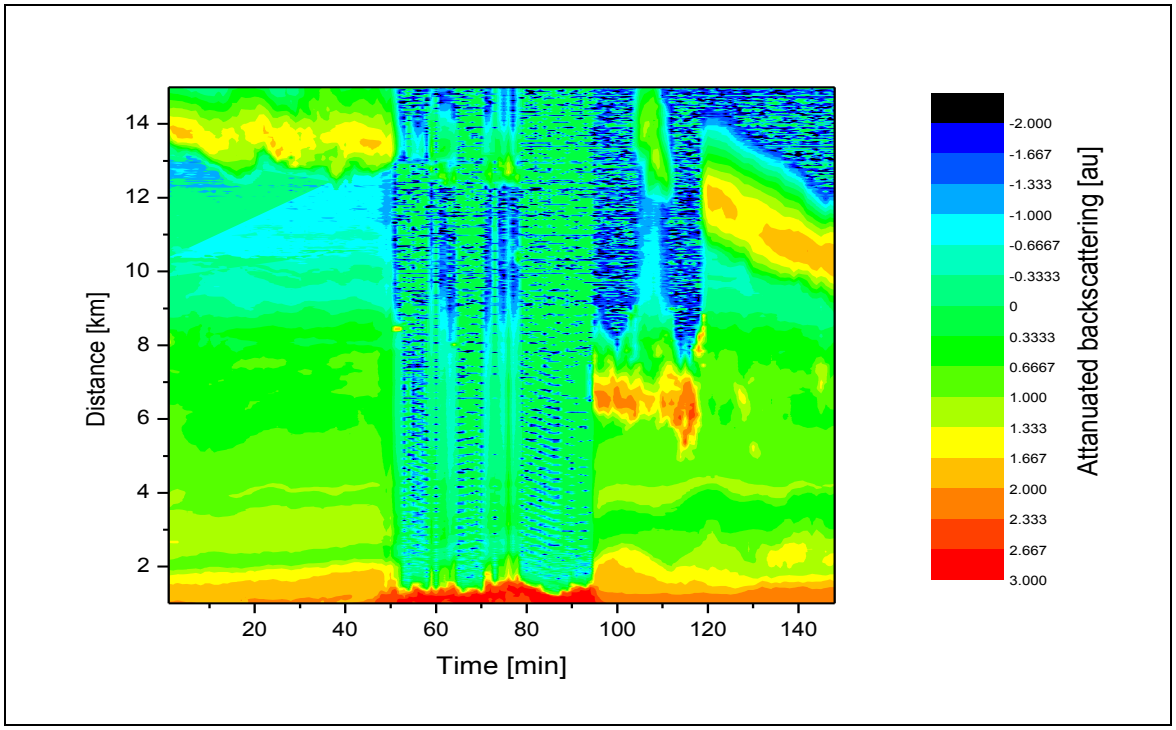

Figure 4.1. The first colormap from the atmosphere over Turkey.

Figure 4.1 shows the first color map obtained from the lidar measurements on 13 May 2009 starting at 20:55. This is a very important beginning in atmospheric aerosol science in Turkey. Colormaps are very useful, such that three parameters can be displayed in a single figure. The vertical axis to the left shows the distance of the signal from the lidar instrument. The altitude can be calculated by multiplying the sine of the measurement angle with the distance which is explained by equation (3.34) in the Methodology chapter. The horizontal axis denotes time, and the colors denote the signal intensity, which is scaled on the right vertical axis. Here, there is a cloud in the telescope field-of-view between the 50th to 95th minutes. Before the 95th minute a dust layer starts to appear which is captured by the lidar after the displacement of the cloud. The dust layer is measured until the 120th minute and then moves away from the field of view of the telescope. At higher altitudes, cirrus clouds can be seen in orange-yellow.

4.1. Experimental Measurements of Spatial and Temporal Variations of Aerosol Scattering Coefficients

In this section, the results obtained during Spring-Summer 2009 are used to test the capability of the system and the algorithms for the calculations of aerosol backscattering and extinction coefficients. The microphysical parameters of atmospheric aerosols are retrieved by complex methods of inversion with regularization and principle component analysis (PCA), both of which have been mentioned earlier in various sections of the thesis. Here, these parameters will be described as well as the variations in their values in various time periods will be demonstrated. Lidar instrument measures extinction and backscatter coefficients and a series of colormaps regarding these coefficients are given below for selected few days as an example. Each figure demonstrates the variation of backscattering and extinction in three wavelengths though a time series. The lidar measurements have been realized for 9 - 10 hour intervals starting at around sunset to sunrise taking into account the different atmospheric and meteorological conditions. In the color maps the signal intensity is scaled in colors with the given scale on the very right column, and on each colormap the intensity is scaled differently to be able to show the aerosol layers with a color contrast. The microphysical parameters of the altitudes are chosen at layers with high aerosol density. Aerosols over Gebze are mainly concentrated inside the PBL at 1000 to 1500 meters. Still some part of aerosols is in the layer above the PBL at about 2500 meters. Complete overlap of the laser beam and the telescope field-of-view (FOV) is achieved at approximately 500 meters altitude, this is why reasonable data starts at 500 meters because at low altitudes because of the lidar overlap, which is caused by the physical process, such that, the collimated laser beam does not completely enter the FOV of the telescope, so that part of the lidar signal can not be used for data processing and retrieval. Another fact which must be taken into account is the fact that the location of the lidar instrument is at approximately 250 m elevation. Measurements were performed at 22 - 30 degrees to the horizontal.

To be able to observe the spatial and temporal variations of aerosols, first the lidar signal needs to be displayed to be able to locate where the aerosol load is. This is illustrated in Figure 4.2.

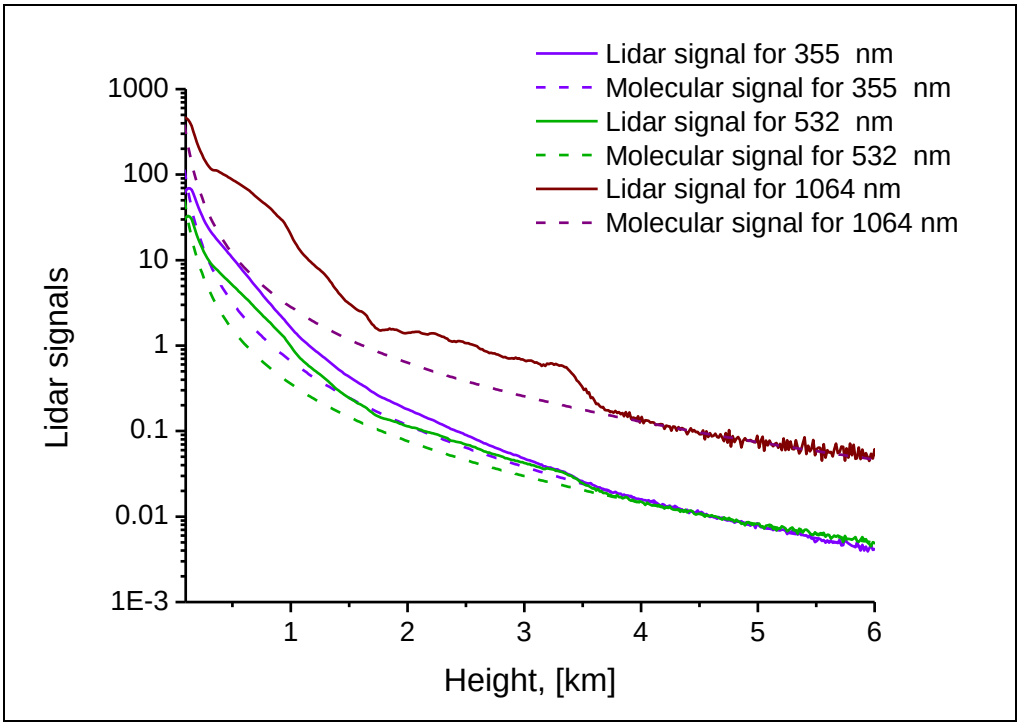

Figure 4.2. Averaged lidar signals, 30 June 2009.

In Figure 4.2 the averaged lidar signals at three (355, 532 and 1064 nm) wavelengths measured on 30 June 2009 are demonstrated. Here it can be seen that the top of the PBL is at around 3500 m, because above that height, scattering is pure molecular, therefore that height is used as a reference point to calibrate the lidar system. The noise signal is good enough to be able to process the data. Here, dashed lines represent the aerosol scattering from atmospheric molecules (Rayleigh scattering) and the solid lines represent the lidar signals which represent the total backscattering volumes. Therefore, the area between the solid curves and the dashed lines shows the aerosol backscattering. Here, 355 nm (ultraviolet wavelength) is demonstrated in violet, 532 nm (visible wavelength) is demonstrated in green and 1064 nm (infrared wavelength) is demonstrated in red. After the calibration of the lidar system to treat the data set, the next step is the demonstration of the averaged aerosol backscattering and extinction coefficients such as in Figure 4.3.

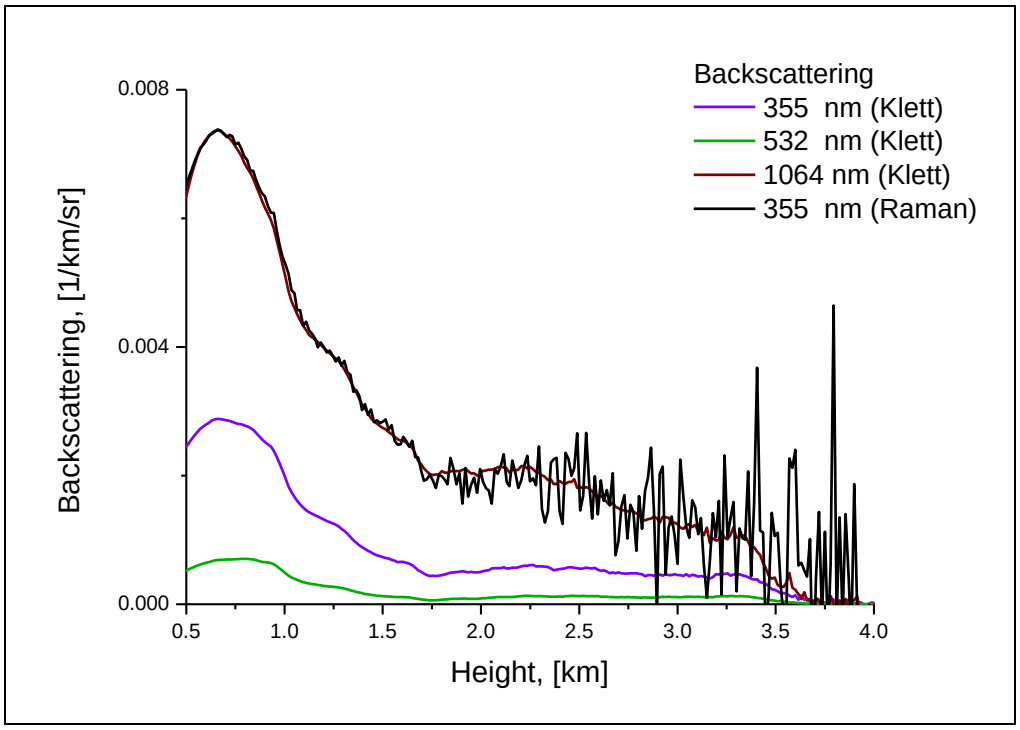

Figure 4.3. Averaged backscattering coefficients, 30 June 2009.

For calculating aerosol backscattering and extinction coefficients, both Klett and Raman methods were used. In Figure 4.3, comparison of the results of calculation is presented. For 355 nm wavelength, data was computed by both Klett and Raman methods. It can be seen that the profiles are very close but with Raman method, the calculation is very noisy especially after 2500 m. because Raman signal is much weaker than the elastic signal. Sounding date is 30 June 2009.

The next few pages contain the colormaps (Figures 4.4 to 4.11) of for the evolution of backscattering and extinction on several selected days in different months, in which a seasonal trend was displayed. These colormaps show the aerosol backscattering and extinction evolution in a three dimensional (distance - time - intensity) picture. The measurements cover approximately 9 hours of data taken during the night for 4 representative months with high aerosol load. For each representative monthly measurement, colormaps of backscattering and extinction coefficients for each day are illustrated.

Some explanations must be taken into account for a better comprehension of the following colormaps (Figures 4.4 to 4.11). It should be noted that the intensity scales are depicted on the right vertical axes, with higher intensity coded with red and lower intensity with blue, which allow visualizing the aerosol layers. The intensity axes on each color map are differently custom valued to be able to show the variations of temporal and spatial variations. It should also be noted that data from the low altitudes (around 500 m) is missing due to lidar overlap function which can be explained as the laser beam is not in the telescope FOV, therefore there is no obtained data lower than aforementioned altitude. The distance which is illustrated on the left vertical axes is the distance from the lidar to the target, and the real height can be calculated by using Equation (3.34) which was explained in the Methodology chapter.

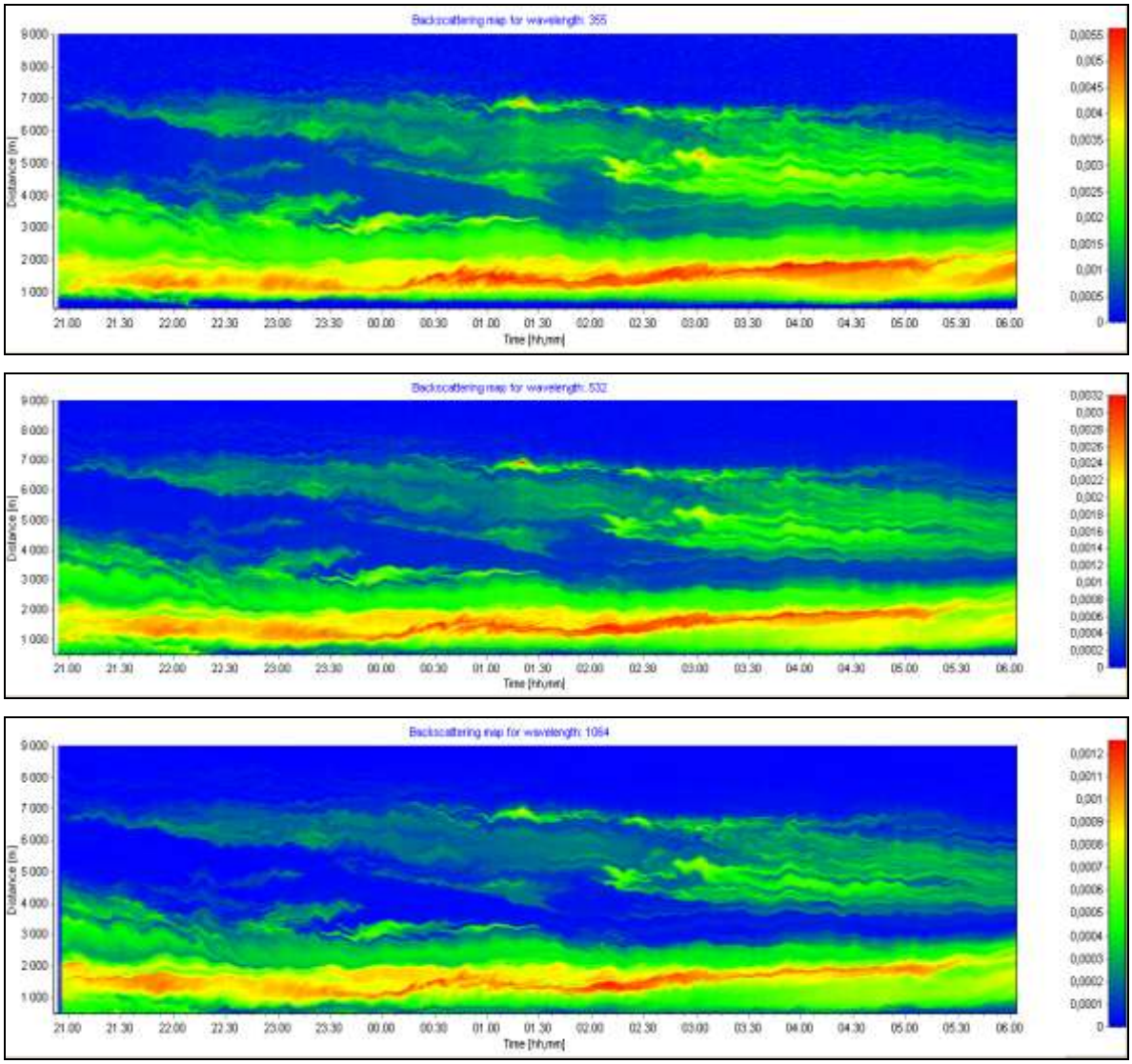

Figure 4.4. Backscattering colormaps of 355, 532 and 1064 nm, 30 June 2009.

Figure 4.4 demonstrates the evolution of aerosol backscattering during a 9 hour lidar measurement on 30 June 2009. The main aerosol load is in distance between 1000 to 2000 m. There is another weak layer of aerosols starting at 6500 m, evolving to develop between 4000 to 7000 m through the later hours, especially after 2 am.

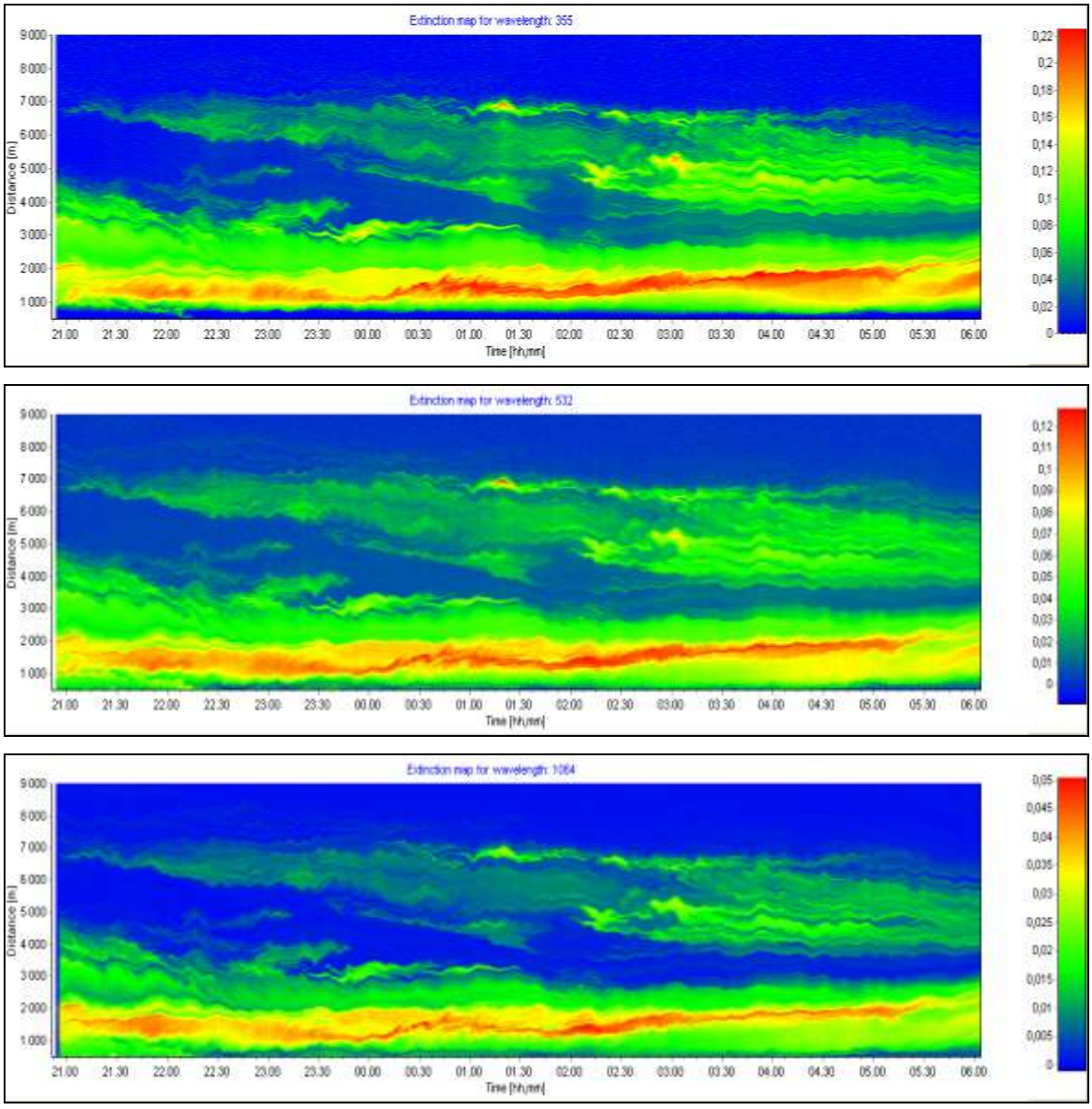

Figure 4.5. The extinction colormaps of 355, 532 and 1064 nm, 30 June 2009.

Figure 4.4 shows the evolution of aerosol extinction. Profiles are in accordance with backscattering, because Klett method was used to calculate the coefficients (Equations (3.3) to (3.10)). The measurement was carried out on 30 June 2009.

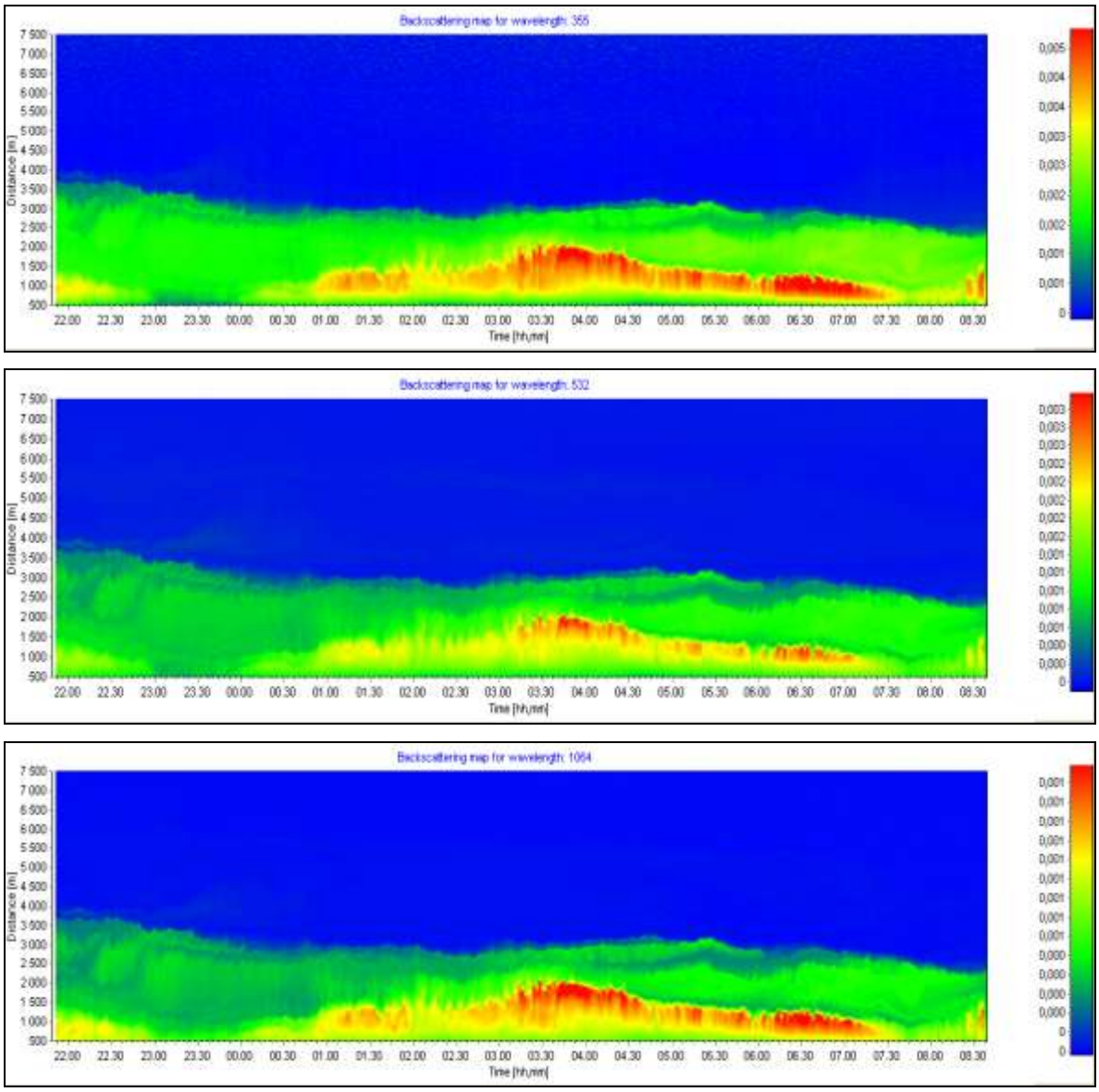

Figure 4.6. The backscattering colormaps at 355, 532 and 1064 nm, 22 July 2009.

Figure 4.6 depicts an aerosol load in the lower parts of the atmosphere, the aerosols are below 3500 m distance (1750 m altitude). There is a dense layer developing at around 1500 m starting at 1 am.

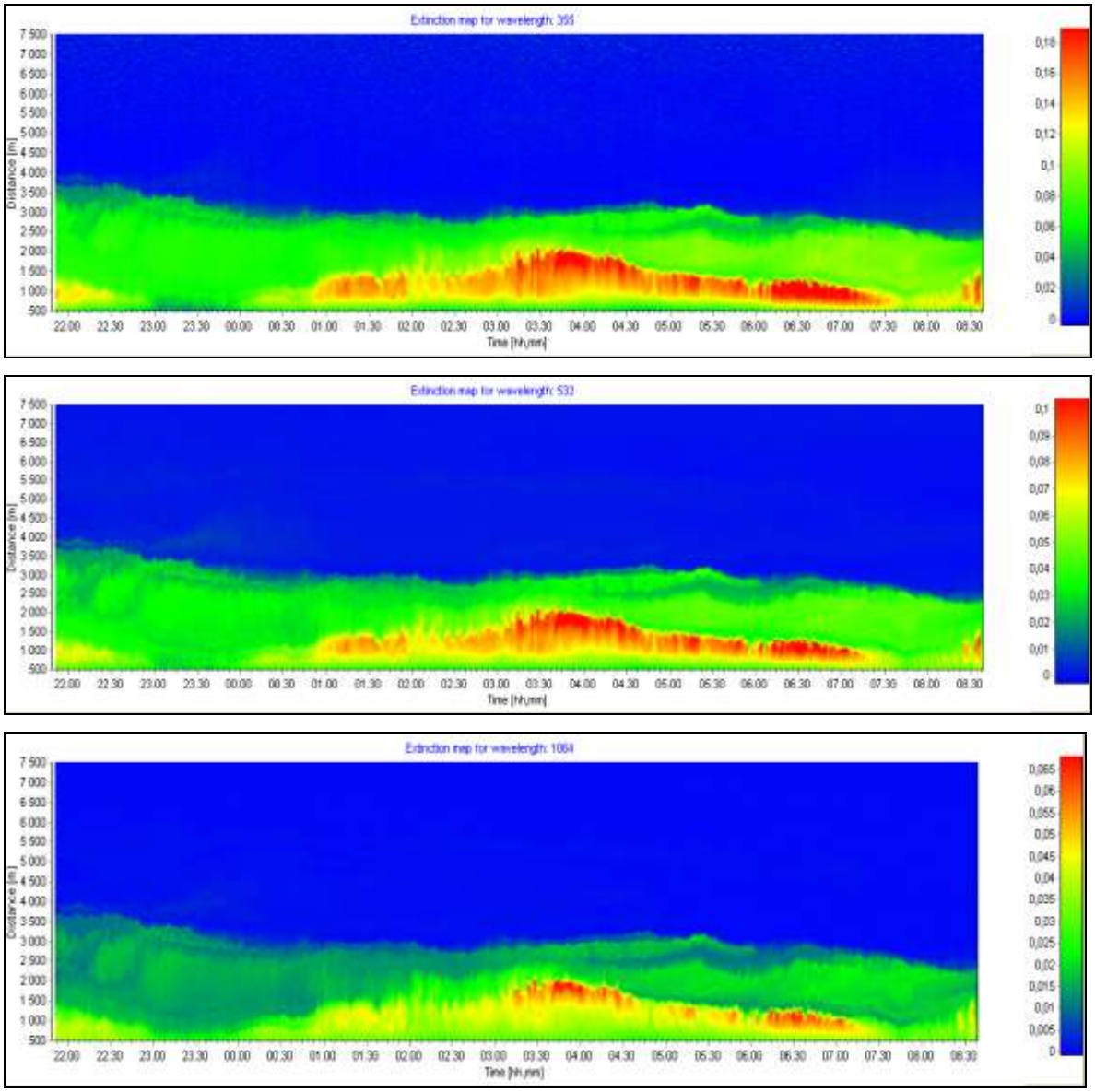

Figure 4.7. The extinction colormaps of aerosols at 355, 532 and 1064 nm, 22 July 2009.

Aerosol extinction profiles are demonstrated in Figure 4.7. Results are in accordance with the aerosol backscattering.

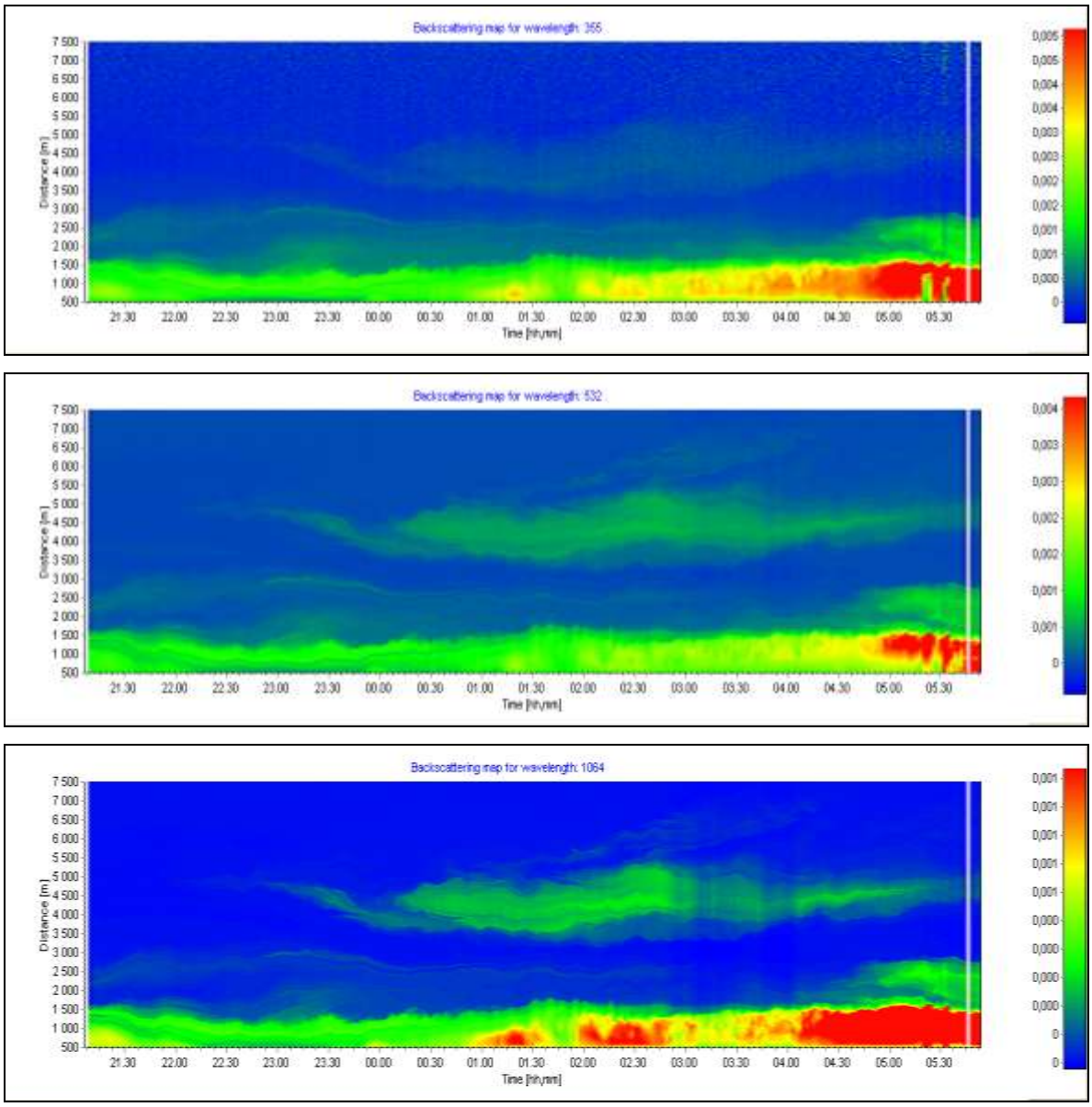

Figure 4.8. The backscattering colormaps at 355, 532 and 1064 nm, 23 August 2009.

Strong intensity at low altitude starting at 1 am with increasing intensity until the morning hours, suggests the existence of a partial clouds or dense aerosol layers in the telescope FOV. Another weak layer is present at around 4500 m in this Figure 4.8.

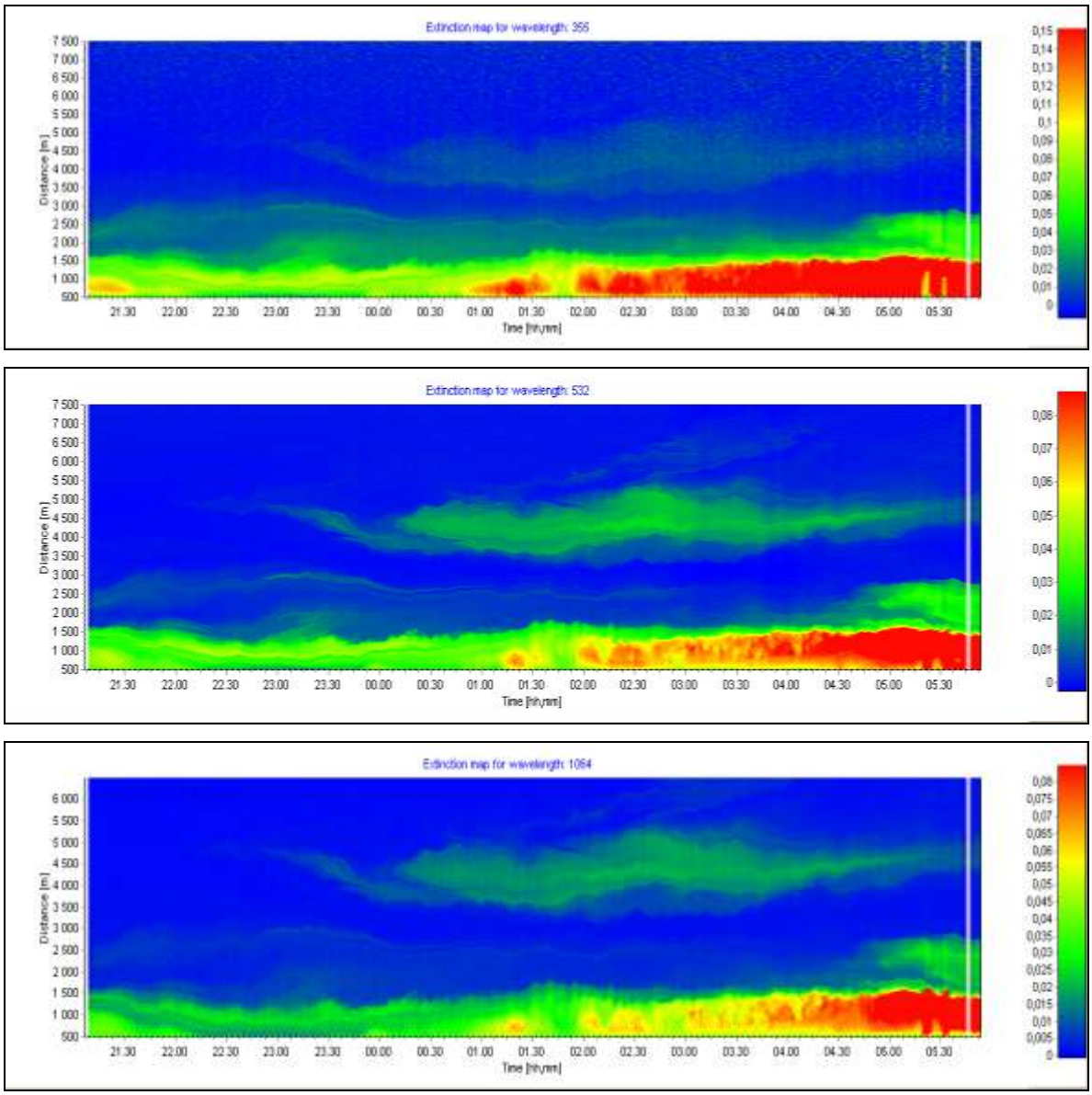

Figure 4.9. The extinction colormaps at 355, 532 and 1064 nm, 23 August 2009.

Figure 4.9 depicts the evolution of extinction in a lidar measurement on 23 August 2009. Starting at 2 am, there is a dense layer of aerosols or some partitional clouds in the lower atmosphere at 1500 m. There is also another weak layer between 3500 - 5000 m starting at 23:30.

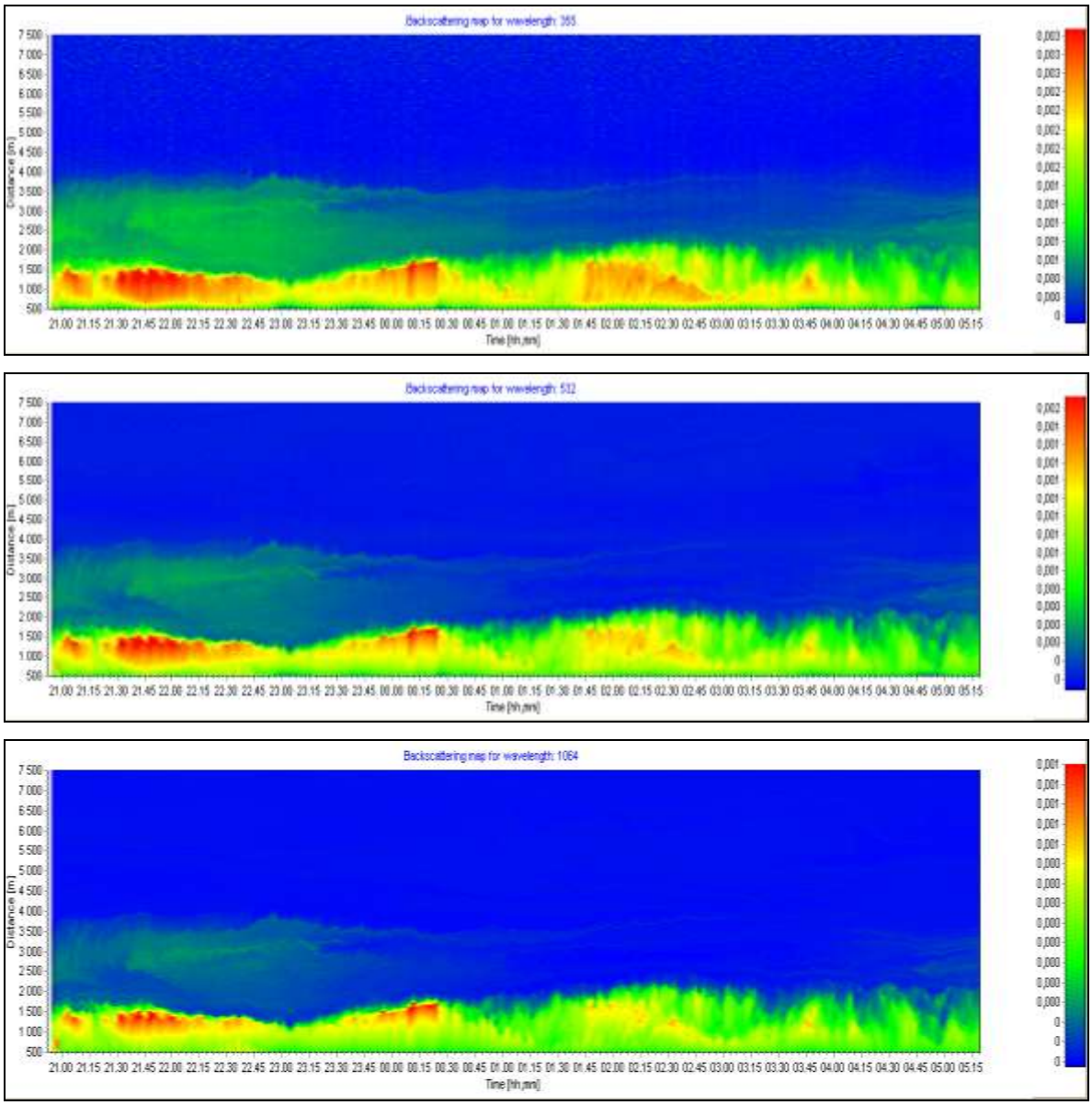

Figure 4.10. The backscatter colormaps 355, 532 and 1064 nm, 29 September 2009.

Aerosol layer is within the PBL in Figure 4.10. Aerosol load is much less than the summer measurements and mainly in the lower atmosphere.

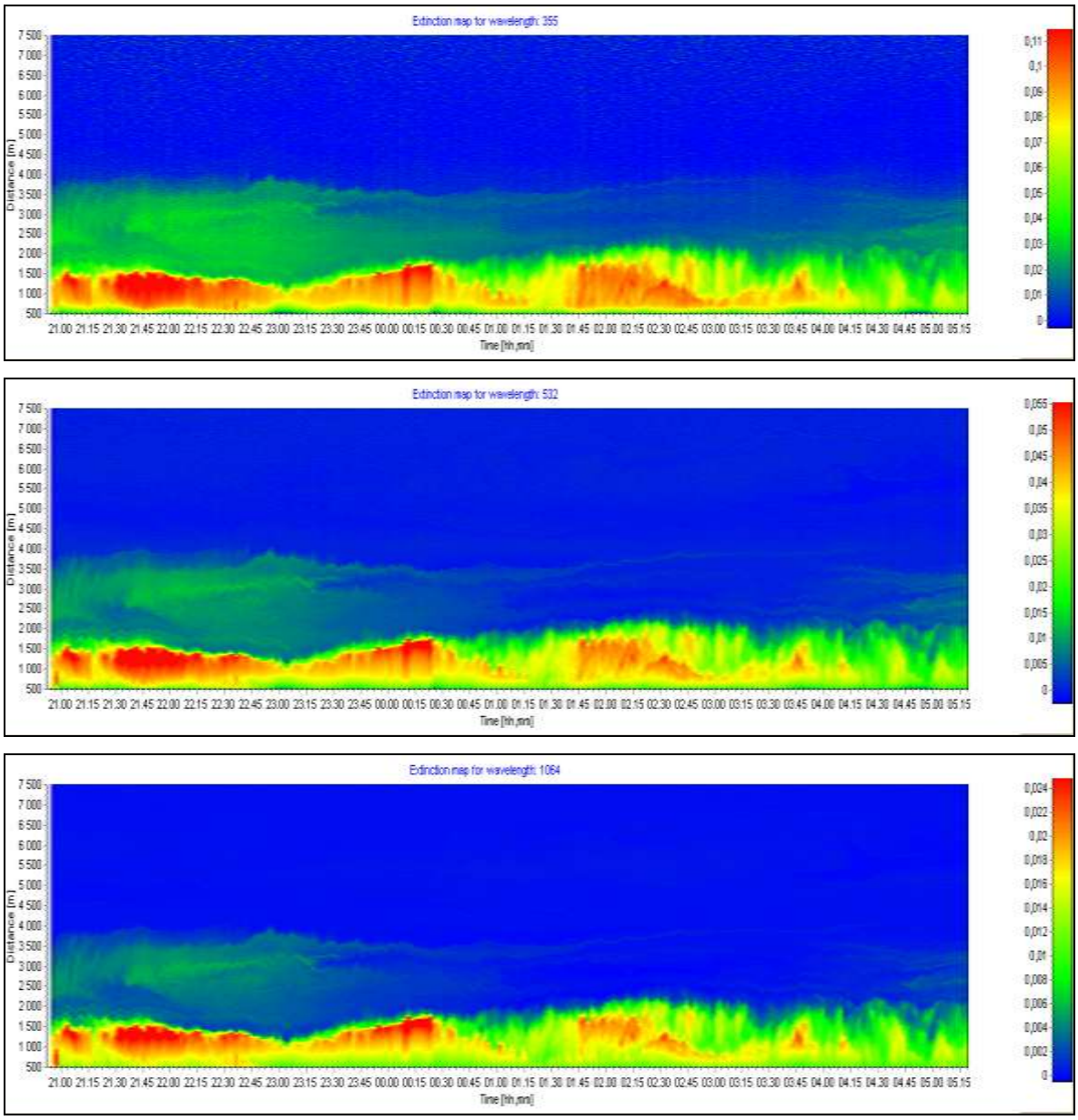

Figure 4.11. The extinction colormaps at 355, 532 and 1064 nm, 29 September 2009.

Figure 4.11 depicts the extinction profiles of Autumn aerosols. Aerosols are mainly inside the PBL.

4.2. Retrieval of Particle Microphysical Properties

As it was stated earlier, the multiwavelength Mie-Raman lidar at TUBITAK MRC, measures three backscattering and two extinction coefficients, which can also be referred as $3\beta + 2\alpha$. Aerosol scattering coefficients have been well studied in literature, however, the number of instutions or research groups and centers which are able to successfully calculate the particle microphysical properties is quite low. Through the inversion of these two variables which was explained in the methodology chapter in Equations (3.14) to (3.30), particle microphysical parameters of complex refractive index, surface density, volume density, surface area density, mean radius and effective radius can be retrieved by inversion with regularization.

Particle size distribution (PSD) and polarization can also be depicted in graphics. In the next following figures (4.12 to 4.22), these parameters are presented and discussed along with graphics of averaged aerosol scattering coefficients and PSD. This section contains representative examples of selected days which shows the comparison of averaged backscattering coefficients and volume depolarization which are in well accordance, and averaged backscattering and extinction coefficients and particle size distribution graphics, under which aerosol microphysical parameters are calculated by custom programmed computer software for a selected layer of aerosols in the column.

Determination of the shape of aerosols gives information about the water content of the aerosols, because aerosols with higher water content have spherical shapes (Veselovskii et al., 2009). When the incident light scatters from the surface of spherical aerosols, the incident light scatters with parallel polarization, in other words, the polarization state of the incident laser light does not change. However, if the particles have irregular shapes, there will be a change in the polarization (depolarization). Figures 4.12 and 4.13 are an example to show how to determine the approximate particle shape by comparing the total backscatter with depolarization.

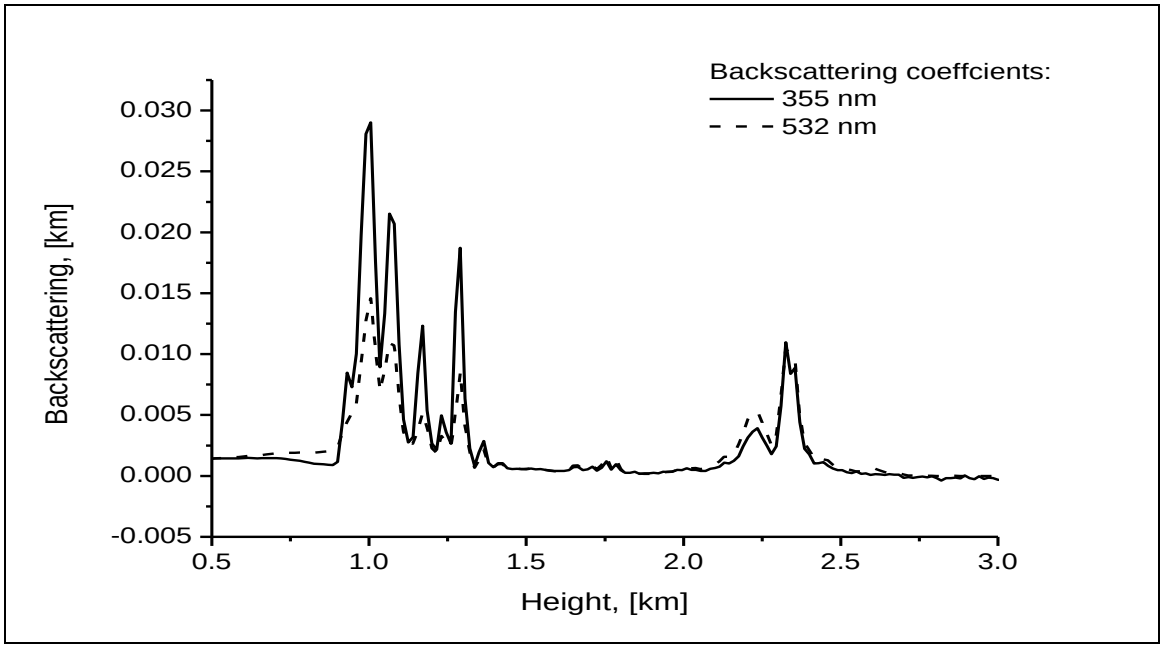

Figure 4.12. Averaged backscattering coefficients, 16 March 2010.

Figure 4.12 demonstrates the averaged backscattering coefficients. There are two layers of aerosols at 1000 to 1300 meters height and at 2300 m.

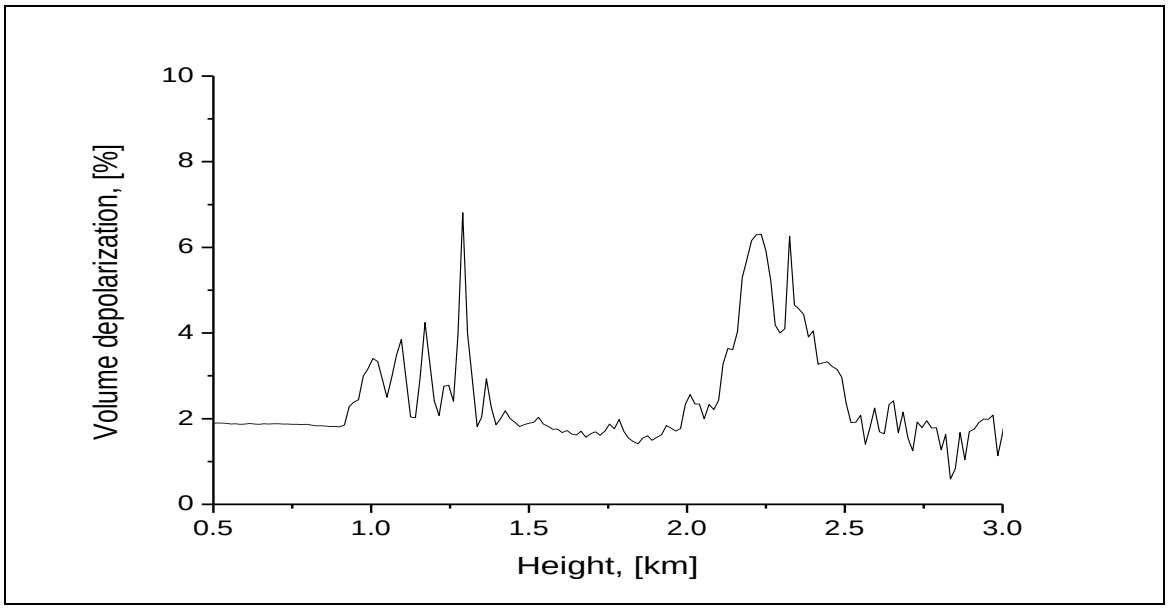

Figure 4.13. Volume depolarization, 16 March 2010.

Figure 4.13 shows the volume depolarization. Comparing with Figure 4.12, it can be seen that backscattering and depolarization are in accordance. 4-6% volume depolarization values suggest that the particles have irregular shapes. Here it can be stated that the aerosols in the lower layer carry more water. Figures 4.14 to 4.20 contain representative examples from selected days from Spring to Autumn which include the log normaled vertical profiles of averaged backscattering and extinction, which are followed by PSD graphics with calculated microphysical parameters at selected heights.

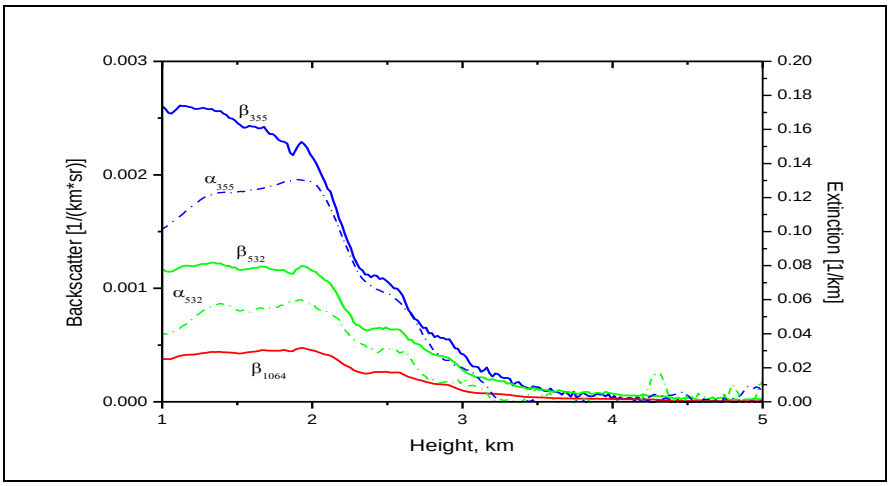

Figure 4.14. Averaged backscattering and extinction coefficients, 20 May 2010.

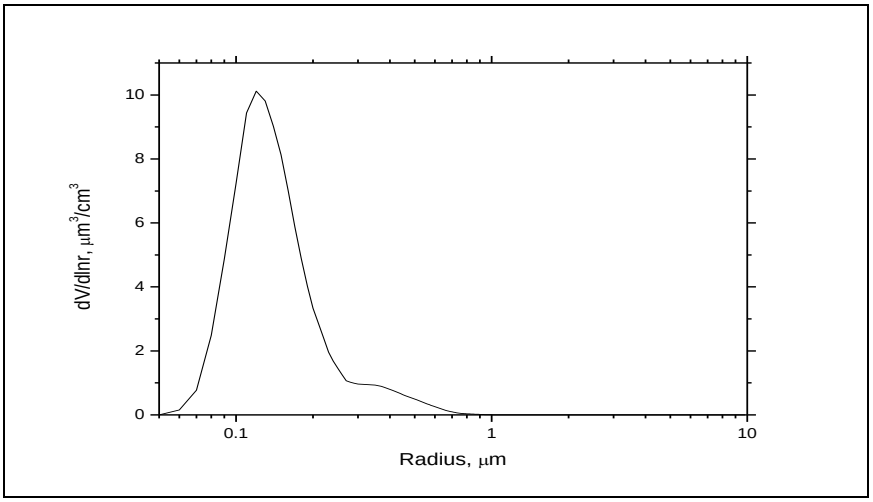

Figure 4.15. Particle size distribution, 20 May 2010.

Figure 4.15 shows the PSD in the layer 1.8 - 2.4 km on 20 May 2010. The fine mode is dominant in the PSD. The particle parameters are calculated as; V = 7.9 $\mu m^3 cm^{-3}$, S = 180 $\mu m^2 cm^{-3}$, N = $1.1*10^{-3}$ cm^{-3}, R_{mean} = 0.1 μm, R_{eff} = 0.13 μm, m = 1.54-i0.003.

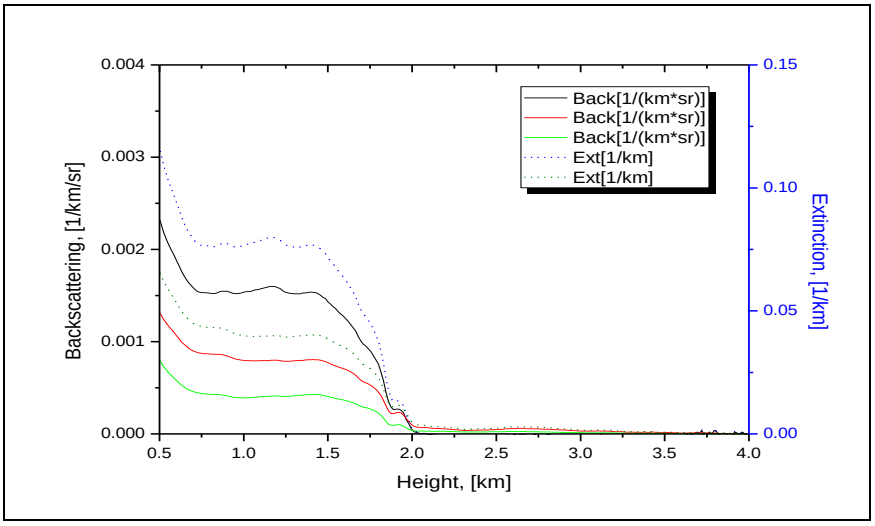

Figure 4.16. Averaged backscattering and extinction coefficients, 22 June 2009.

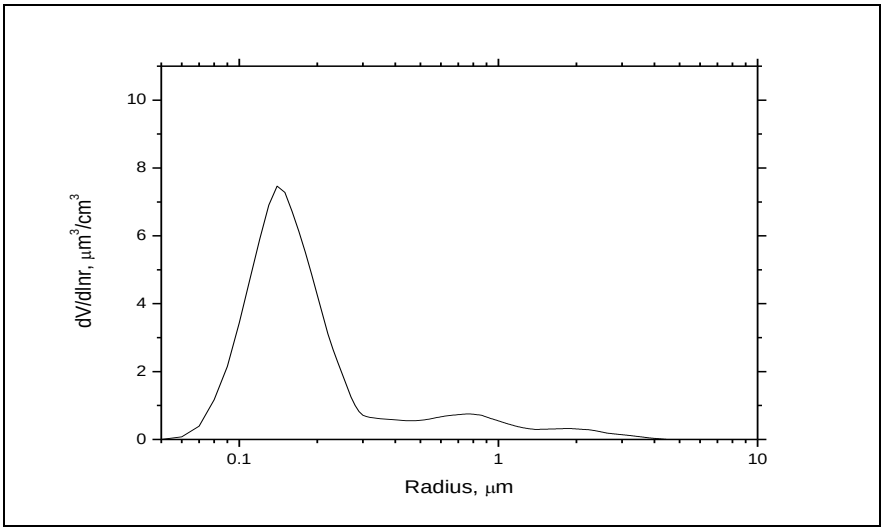

Figure 4.17. Particle size distribution on 22 June 2009.

Figure 4.17 shows the PSD in the layer 1.8 - 2.4 km on 22 June 2009. The fine mode is dominant in the PSD. The particle parameters are V = 6.8 $\mu m^3 cm^{-3}$, S = 130 $\mu m^2 cm^{-3}$, N = 650 cm^{-3}, R_{mean} = 0.12 μm, R_{eff} = 0.16 μm, m = 1.52-i0.002.

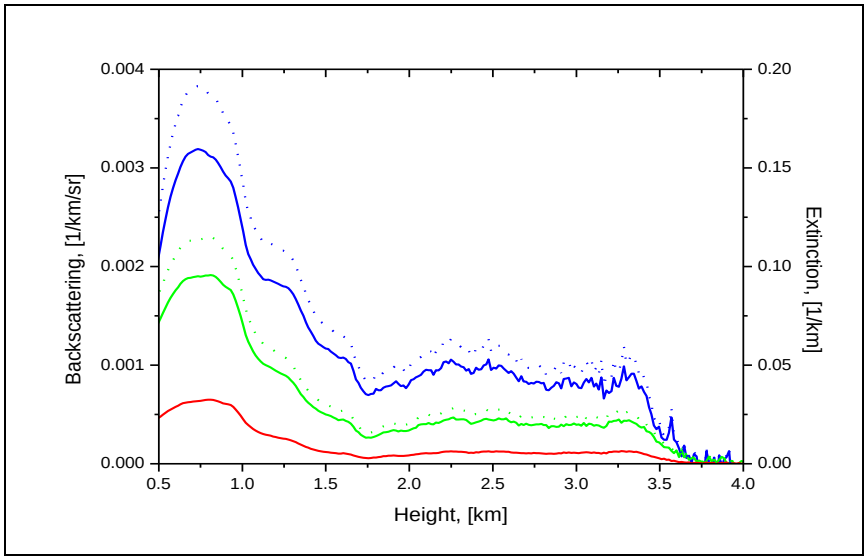

Figure 4.18. Averaged extinction and backscattering coefficients, 30 July 2009.

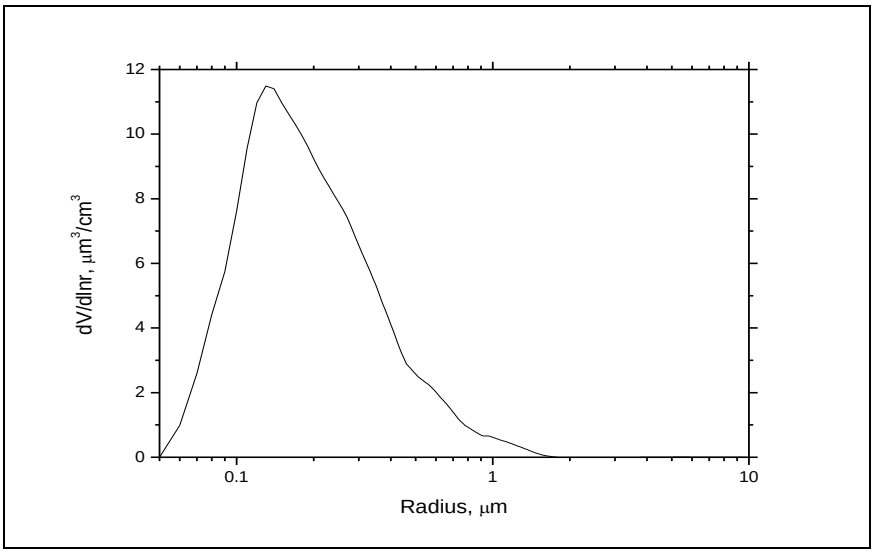

Figure 4.19. Particle size distribution, 30 July 2009.

Figure 4.19 shows the PSD in the layer 0.8 - 1.2 km on 30 July 2009. The fine mode is dominant in the PSD. The values for the particle parameters are V = 16 $\mu m^3 cm^{-3}$, S = 300 $\mu m^2 cm^{-3}$, N = 1.8*10^{-3} cm^{-3}, R_{mean} = 0.12 μm, R_{eff} = 0.17 μm, m = 1.45-i0.003.

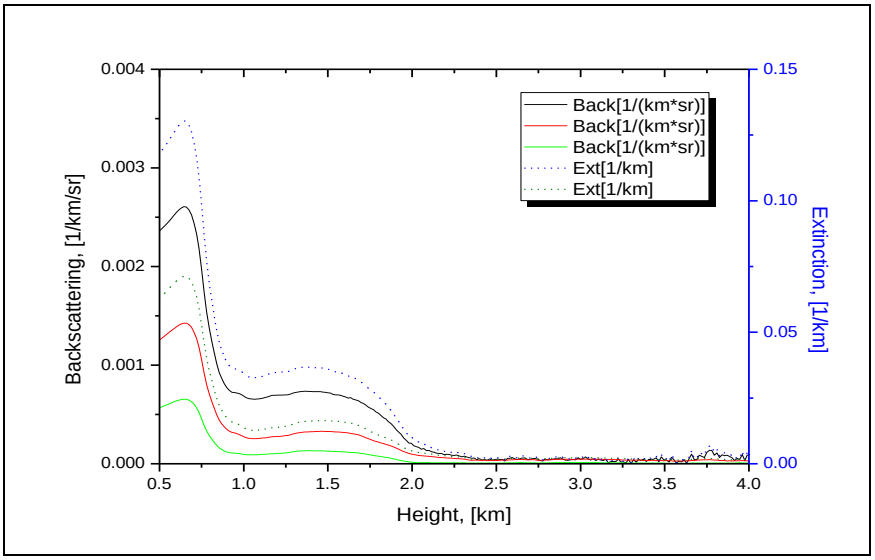

Figure 4.20. Averaged extinction and backscattering coefficients, 21 August 2009.

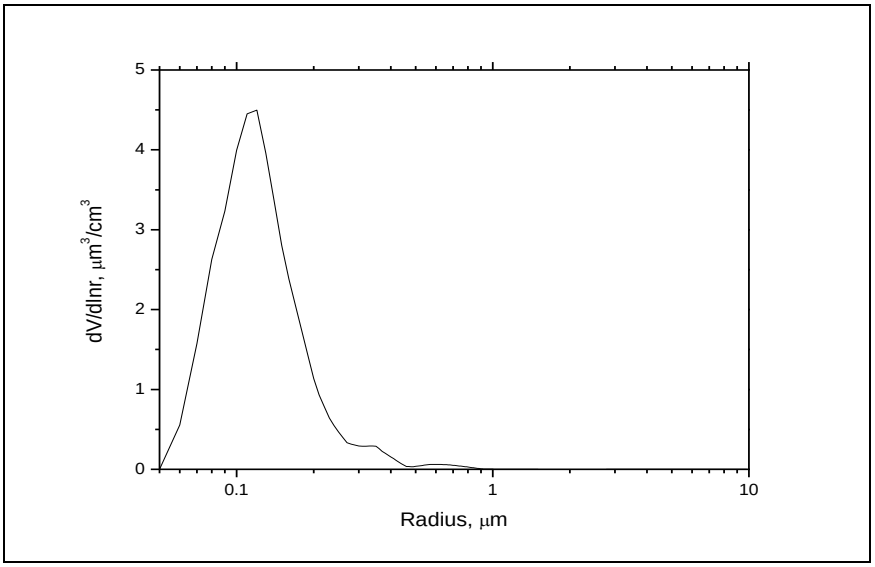

Figure 4.21. Particle size distribution, 21 August 2009.

Figure 4.21 shows the PSD in the layer 1.0 - 1.5 km on 21 August 2009. The fine mode is dominant in the PSD. The particle parameters are V = 3.7 $\mu m^3 cm^{-3}$, S = 100 $\mu m^2 cm^{-3}$, N = 860 cm^{-3}, R_{mean} = 0.09, R_{eff} = 0.15 μm, m = 1.48-i0.002.

4.3. Retrieval of Time-Sequences of Particle Parameters Using Principle Component Analysis

A new approach to retrieve the aerosol microphysical parameters by a new method which uses principle component analysis (PCA) which was explained in the Methodology section in Equations (3.31), (3.32) and (3.33), was developed, tested and used during this research. The results are in accordance with the existing method of inversion with regularization. PCA method proved to be very useful, bacause it is very fast, tolerent to errors in the input data, therefore very efficient to treat large amounts of lidar data. The following sections discusses the comparison of PCA and regularization methods, and application of PCA to lidar data to obtain time-series of aerosol microphysical parameters. This section includes the first colormaps of the temporal variations of particle parameters in literature.

4.3.1. Comparison of the PCA and Regularization Retrievals

To validate the PCA technique, the same set of data was analyzed with both PCA and regularization approaches. Both algorithms were applied to reliable and already validated experimental results obtained at NASA/GSFC in August-September 2006 (Veselovskii et al, 2009).

The Raman lidar based on a tripled Nd:YAG laser provided three backscattering and two extinction coefficients (so called 3β + 2α set). From these data the particle parameters, such as volume (V), surface (S), number (N) densities, effective radius (r_{eff}) and complex refractive index $m = m_R - im_I$ were retrieved Equations (3.31) to (3.33)). The inversion with regularization during that session was validated by comparison with

AERONET column integrated values. The vertical profiles of aerosol scattering coefficients are demonstrated in the figure below:

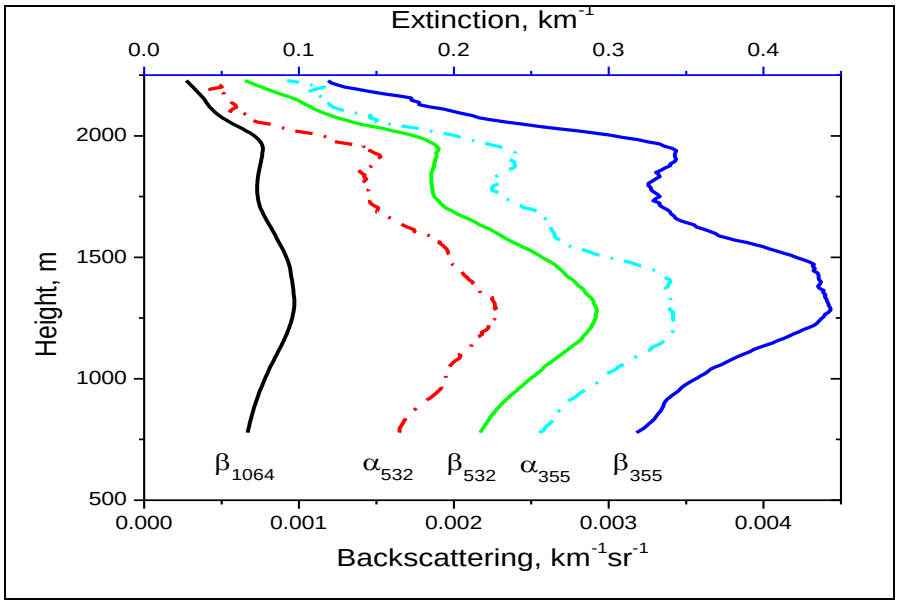

Figure 4.22. Vertical profiles of aerosol backscattering and extinction coefficients at 355, 532 and 1064 nm wavelengths.

The comparison of PCA and regularization approaches was performed for several days characterized by different atmospheric conditions. Here, for illustration, the results for the measurements on 15 August 2006 were shown in Figure 4.22. The vertical profiles of backscattering and extinction coefficients at multiple wavelengths are shown. The aerosol is contained inside the PBL with a top at 2.25 km. Because of the lidar overlap issues, data could be processed at minimum height of 750 m, therefore that part of the data is not shown in the figure (Veselovskii et al., 2009).

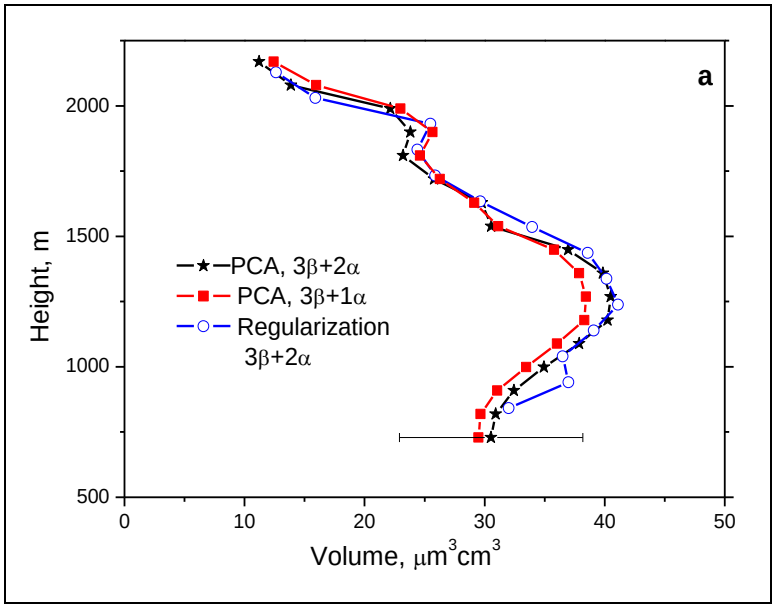

Figure 4.23. Vertical profiles of particle volume density retrieved with regularization and PCA techniques from 3β + 2α and 3β+ 1α data sets.

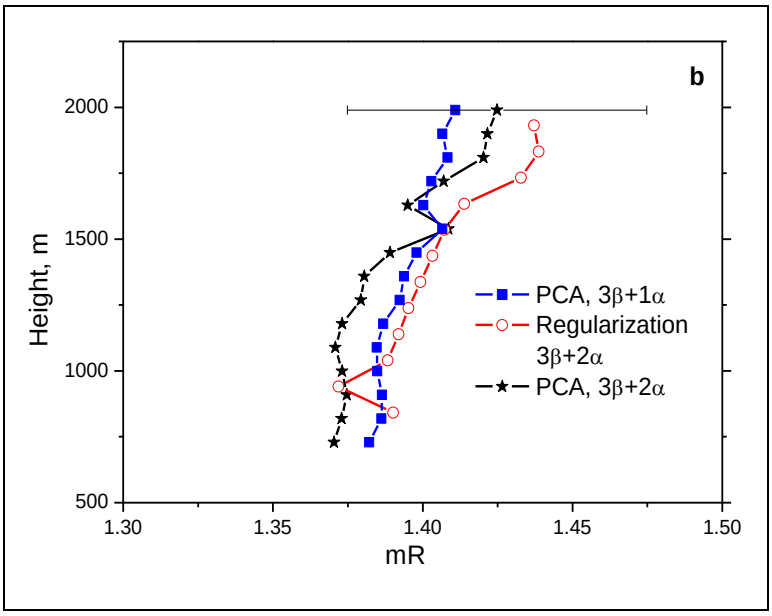

Figure 4.24. Vertical profiles of real part of complex refractive index retrieved with regularization and PCA techniques.

Figure 4.23 and 4.24 show the vertical profiles of volume density and the real part of refractive index retrieved with the PCA and the regularization approaches. The profiles of volume density are very close. It should be mentioned that the uncertainty of the volume retrieval is estimated as approximately 25%, but this number refers to absolute values, while the relative change of the volume with height can be retrieved with better accuracy, so the vertical structure of volume density could be reproduced.

The vertical profiles of the refractive index obtained with both techniques are also in agreement: m_R rises with height from 1.37 to 1.43. The accuracy of m_R retrieval is estimated as ± 0.05, but again, the relative changes can be evaluated with better precision, so the vertical trend can be estimated. It is shown that, the PCA approach can be used even with reduced data set. The same figure shows the results obtained from 3β + 1α set (α_{532} is removed). As it can be seen in the figure, the retrievals from 3β + 2α and 3β + 1α sets are in reasonable agreement. The analysis of other retrieved parameters demonstrates that the vertical profiles obtained with the PCA technique in general are less oscillating thus can provide better height resolution. This is illustrated in Figure 4.25, showing the effective radius retrieved with the PCA and regularization techniques.

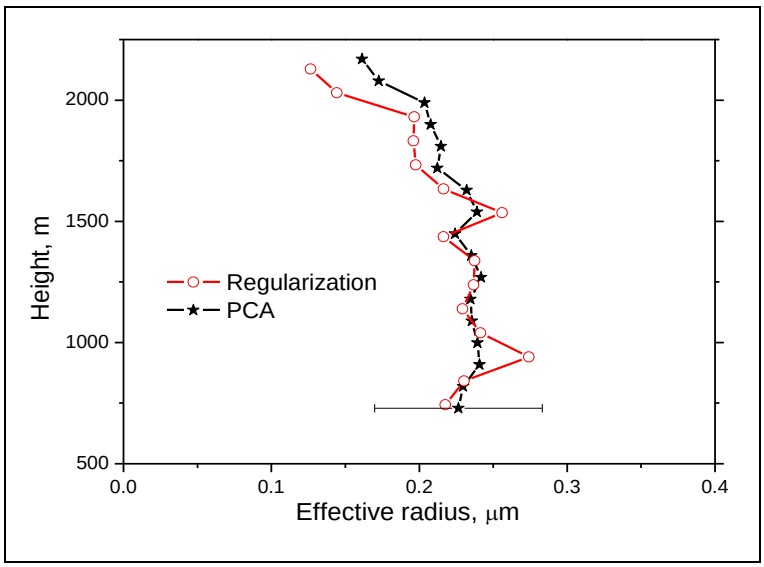

Figure 4.25. Vertical profiles of effective radius retrieved with regularization and PCA techniques from 3β + 2α data set.

From the results presented in this section, it can be concluded that retrievals done by the principle analysis method, are in reasonably good agreement with those of the inversion with regularization approach. At the same time PCA is much faster to treat large amounts of lidar data, thus can be used for processing of time-series of lidar measurements which require considerably very fast data processors. One other advantage of principle component analysis is its tolerance to errors in the input data.

4.3.2. Application of the PCA Algorithm to the Time-Series of Lidar Data

The PCA algorithm was applied to process the results of measurements performed in May-July 2009. The results are shown in Figures 4.26, 4.27 and 4.28.

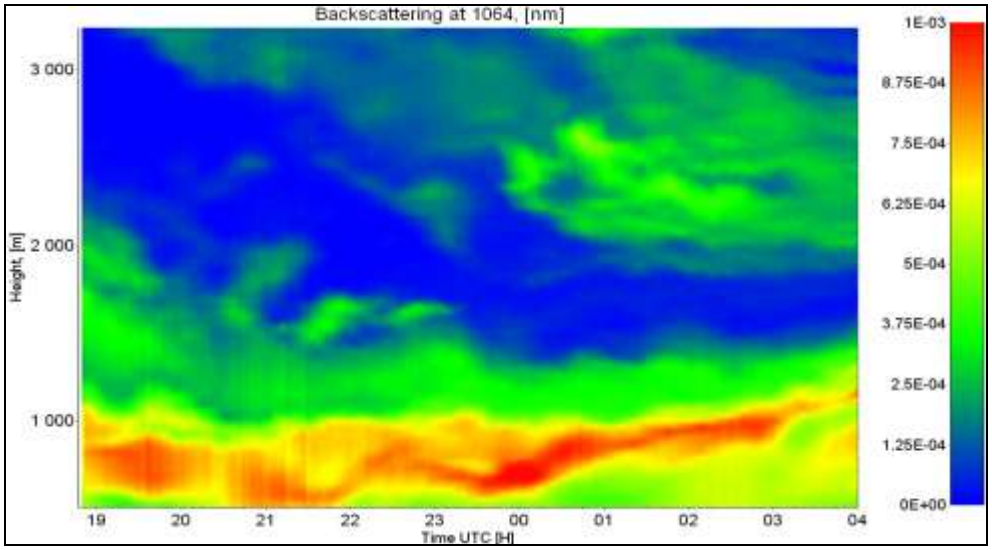

Figure 4.26. Vertical profiles of particle backscattering coefficients at 1064 nm.

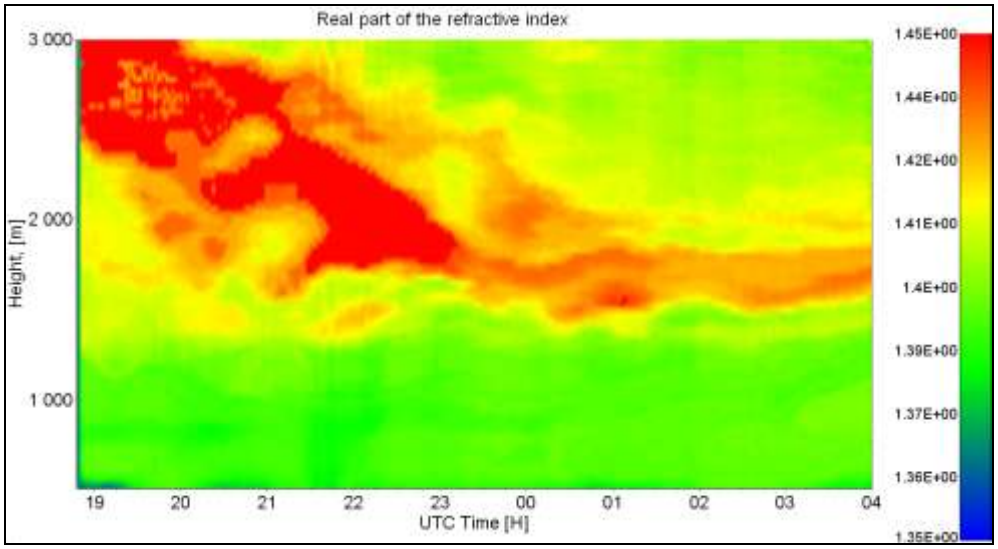

Figure 4.27. Vertical profiles of real part of complex refractive index at 1064 nm.

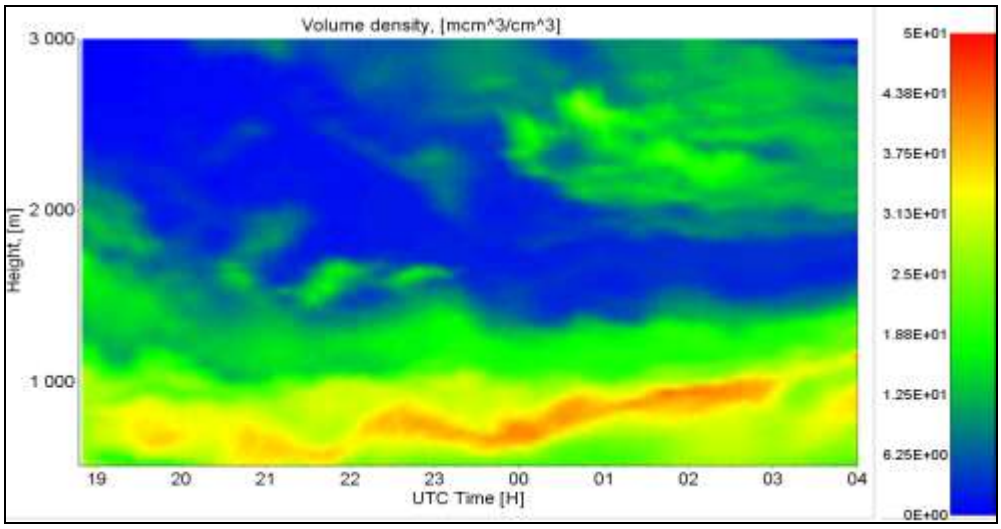

Figure 4.28. Vertical profiles of volume density at 1064 nm.

Temporal variation of aerosol vertical distribution is illustrated in Figure 4.26, showing the time-series of the measured particle backscattering coefficient at 1064 nm. The time series of 3β + 1α data were used to retrieve the particle parameters, as discussed in the previous section. Figures 4.27 and 4.28 show the temporal evolution of the vertical distribution of the real part of refractive index and the volume density. The main part of aerosol is concentrated below 1.5 km. There is a secondary layer above 2 km, and between

these layers the particle concentration is quite low. The refractive index inside these layers is $m_R \approx 1.39$, so the aerosols likely contain significant amounts of water. In the gap between the layers the refractive index increases up to $m_R \approx 1.45$. The height-temporal distribution of the volume density resembles the distribution of β_{1064}: the main aerosol volume is concentrated inside the PBL and in the layer at ~2.5 km.

This is the first attempt to invert the time-series of the multiwavelength lidar data and the obtained results should be considered as preliminary. Further research aimed to reduce uncertainty of retrieval by using interdependence of particle parameters in adjacent layers and time-series is in progress. Additional meteorological information is also demanded to analyze the spatio-temporal distribution of the particle parameters. The PCA approach was tested for ability to retrieve particle parameters from the MW lidar measurements. A comparison with previously developed regularization algorithm demonstrates that the approaches provide similar results. At the same time PCA is much faster and can be used for analyzing large amounts of lidar data. The application of this approach to the time series of MW lidar data allowed for the first time in literature to provide height-temporal distribution of the particle parameters.

4.3.3. Measurement of Water Vapor Mixing Ratio

Water vapor mixing ratio can be defined as the volume of water vapor in 1 cubic meter of air. It is very important to be able to measure water vapor mixing ratio because water vapor determines the energy balance of the atmosphere. Condensation of the water vapor provides a large amount of heat into the atmosphere. Also, the water vapor content of the atmosphere influences the particle size, therefore with the abundance of larger particles, total scattering will as well be higher. Hygroscopy can be defined as the tendency of a substance to attract water molecules from the surrounding media by absorption and adsorption. Many aerosol species are known to attract water molecules and swell, and their sizes increase.

In this section the results from vertical profiles of aerosol physical parameters in the PBL from multi-wavelength lidar measurements under varying relative humidity conditions is presented. To demonstrate the potential of the multi-wavelength technique to study aerosol hygroscopic growth, data selection techniques are used to determine the mixing of aerosols in the PBL and hygroscopic growth factors are calculated for the best of these cases. The main intention of this section is to demonstrate the ability of the multi-wavelength Raman lidar technique to profile the vertical distribution within the planetary boundary layer of critical aerosol parameters such as mean and effective radius, complex refractive index, number, surface and volume densities under varying relative humidity conditions. A multi-wavelength Mie-Raman lidar and upgraded inversion algorithm permits the simultaneous retrieval of microphysical particle parameters at all heights in the profile (Veselovskii et al, 2009). Figure 4.29 illustrates the variation of water vapor mixing ratio with height.

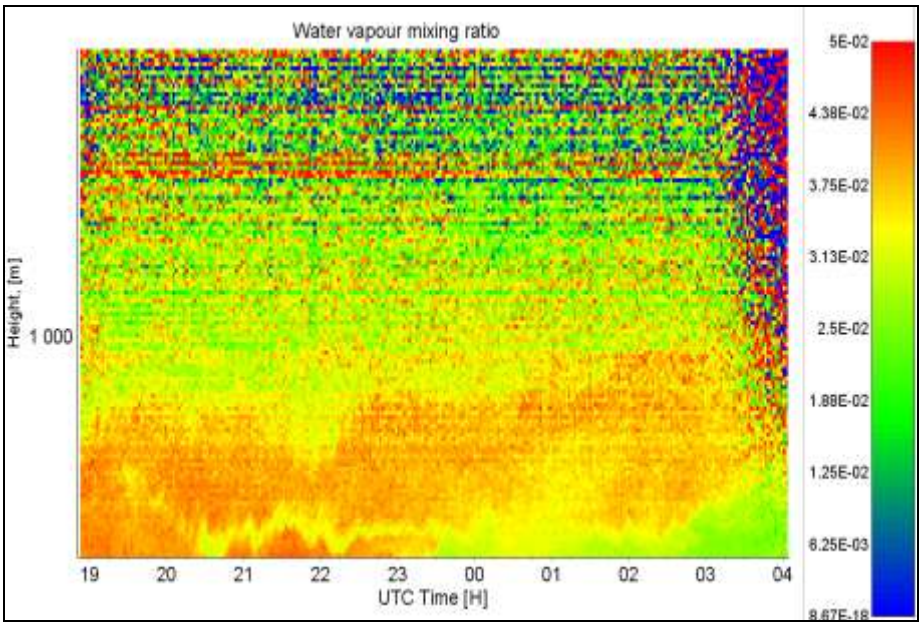

Figure 4.29. Colormap of water vapor mixing ratio, 30 June 2009.

The results presented here demonstrate the potential of the multi-wavelength lidar technique for the study of aerosol hygroscopic growth in the atmosphere. Figure 4.29 shows the variation of water vapor mixing ratio. Although the derived hygroscopic growth

parameters agree well with modeling, they must be considered preliminary due to the lack of temperature data at the lidar site and the inability of fully resolve the coarse mode of the PSD. In a future study with the rotational Raman lidar technique, temperature of the atmosphere can be measured at range resolved altitudes (Veselovskii et al, 2009).

4.4. Preliminary Results from the Volcanic Ash Plumes of Eyjafjallaöküll Eruption

This section is the application of the PCA method to study a real time episode of an intrusion of the ash particles from a volcano eruption. The eruption of the Iceland volcano Eyjafjallaöküll undoubtedly affected whole Europe. The ash particles in the first weeks was so dense that air traffic was affected, leaving thousands of people. The ash was being followed and monitored by EARLINET lidars and arrived to Turkey after a few weeks. The measurements to investigate the event, started at TUBITAK MRC, and the results proved that these kinds of particle intrusions can be detected, monitored and interpreted by the help of multiwavelength Mie-Raman lidar technology.

Volcanoes represent one of the most important natural sources of pollutants to the atmosphere, both during and between eruptions. A good understanding of volcanic volatile emissions in space and time, and of their atmospheric chemistry, and physical and radiative effects, is essential for various branches of atmospheric science. Eruptions of El Chichón, Mexico in 1982 and Mt. Pinatubo in 1991 highlighted the radiative and chemical significance of stratospheric aerosol veils associated with large explosive volcanic eruptions, and contributed to understanding of the composition and evolution of volcanic clouds, and their wider impacts (Robock, 2002). In contrast the atmospheric and environmental impacts of volatile emissions into the troposphere by smaller eruptions and sustained magmatic and hydrothermal degassing are poorly understood, even though the time-averaged magnitude of such emissions exceeds that due to the rare, large events (Mather et al., 2003).

Tropospheric volcanic aerosol plays an important role in atmospheric radiation, both directly by backscattering and absorbing short-wave radiation, and modifying cloud cover and cloud radiative properties (Kaufman, 2002). Despite the lower source strength of

volcanic emissions compared with anthropogenic sources, volcanogenic sulfur species may have at least as large an effect on the Earth's radiative budget as anthropogenic sulfur (Graf et al., 1998). This is due basically to the comparative altitude of these sources: many volcanoes degas into the free troposphere, whereas anthropogenic emissions are generally entrained in the planetary boundary layer where species lifetimes are reduced. Tropospheric volcanic aerosol can also affect terrestrial ecosystems and human health on local to regional scales (Delmelle et al., 2001; Grattan et al., 2003). Coarse particles (2.5–10 μm) are primarily associated with the aggravation of respiratory conditions, such as asthma, in humans. Fine particles (< 2.5 μm) are implicated in increased heart, lung and respiratory disease, and symptoms such as asthma, decreased lung function, and premature death.

While volcanic emissions have contributed to atmospheric evolution throughout the history of the Earth, the increases in anthropogenic emissions since the Industrial Revolution mean that the environmental impacts of natural emissions may now be modified. It is important to understand the character and chemistry of natural tropospheric emissions in order to identify and interpret the possible effects of their interactions with anthropogenic pollutants. In addition to their impacts on the Earth's climate and global chemical cycles, there are more directly volcanological motives for studying volcanic particle emissions. Studies of volcanic gas, aerosol and condensates may provide valuable information about sub-surface magmatic conditions, Monitoring of particle emissions can support volcano monitoring efforts, tracking of volcanic plumes, and evaluation of their potential health impacts (Oppenheimer, 2003).

Earlier, it was stated that volcanic eruptions which can penetrate the stratosphere are not common. However, on a single occasion large amounts can be released into the atmosphere, which can be monitored after many days. The seismic activity in the small ice cap, Eyjafjallaöküll (island-mountain glacier in Iceland) started as early as 26 February 2010 and on 14 April 2010, it erupted. After 2 days the plume reached Europe causing optically the strongest volcanic ash plumes. For the first time since World War II, the air traffic over Europe was disrupted and many countries closed their air traffic due to the failure of jet engines and low visibility. This single event can be regarded as a natural

experiment for the investigation of volcanic ash on climate and local and regional weather, especially on cloud and ice formations and atmospheric radiative transfer. European Aerosol Research Lidar Network (EARLINET) has been following the event since the beginning, making lidar measurements on several stations on a daily basis and publishing their findings on their web site (EARLINET website, 2010). Ash concentrations of record values have been measured over central Europe at EARLINET stations at Hamburg and Cabauw two days after the eruption on 16 April 2010. The ash continued to spread over Germany to Leipzig and Munich, then to all around Europe by atmospheric winds and moved downward with gravity and downwinds.

The volcanic ash reached Turkey in late May, and on 19 May 2010, several measurements were made until 22 May 2010, to be able to understand the vertical distributions and microphysical parameters of volcanic ash over Turkey. The developed lidar system proved to be very useful in detecting the ash plumes and distinguishing them from other aerosols and in determining the time-series of the microphysical parameters of the ash particles. A case study was realized during this episode and the following figures (4.30 to 4.37) shows the results obtained by those measurements.

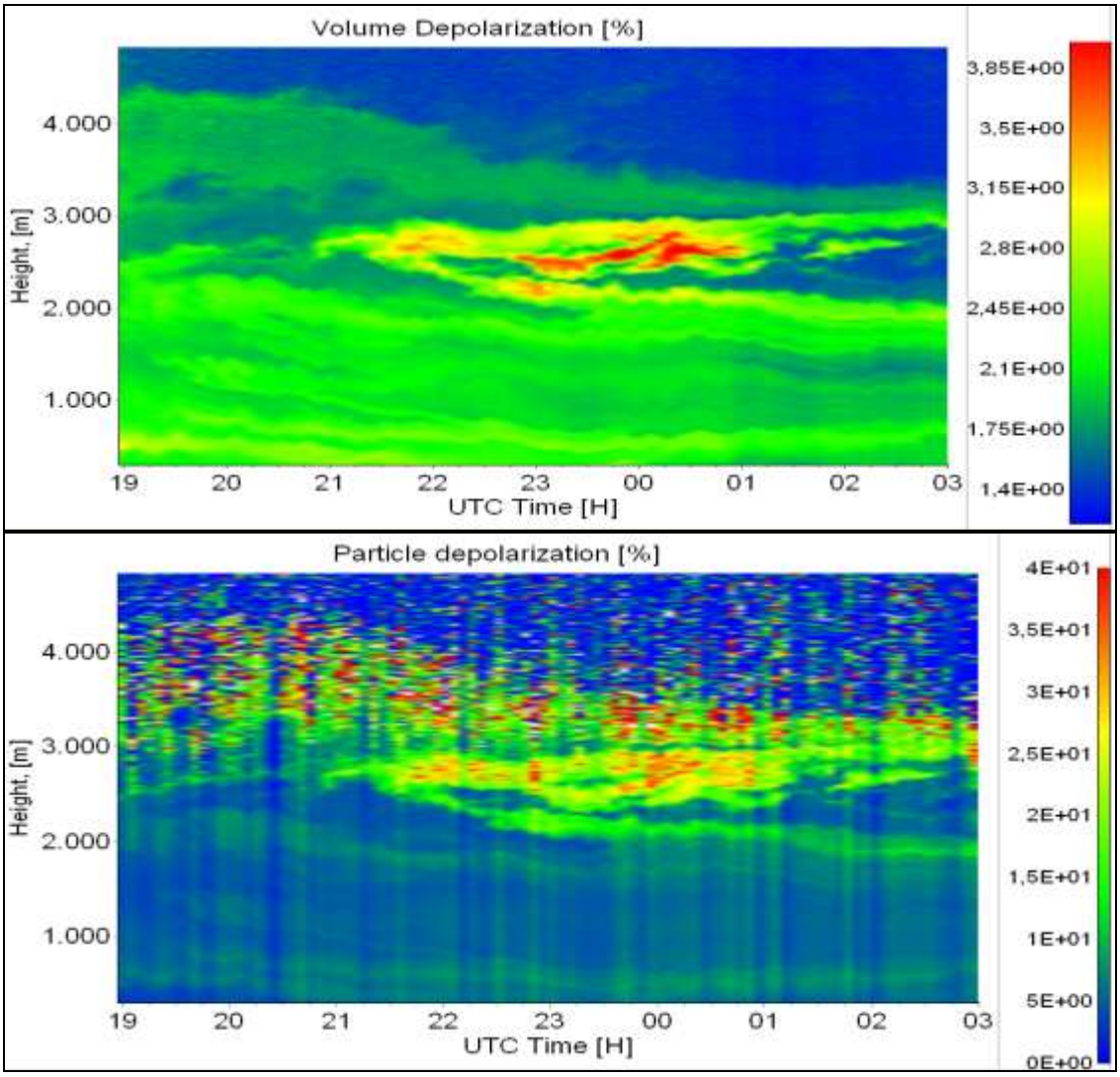

Figure 4.30. Volume and particle polarization of the ash plumes.

Figure 4.30 shows the variation of polarization approximately 35 days after the eruption. Here, particle polarization is the polarization from the atmospheric particles and volume depolarization is the total polarization which includes polarization by molecules additionally. By measuring the strong increase of particle polarization, the ash plumes were detected at around 2500 meters. These pictures show the temporal evolution of volume and particle depolarization. Polarization ratio is about 25% which is a typical value for volcano ash particles. These results are in agreement with the results obtained by EARLINET and published in the website of the lidar network.

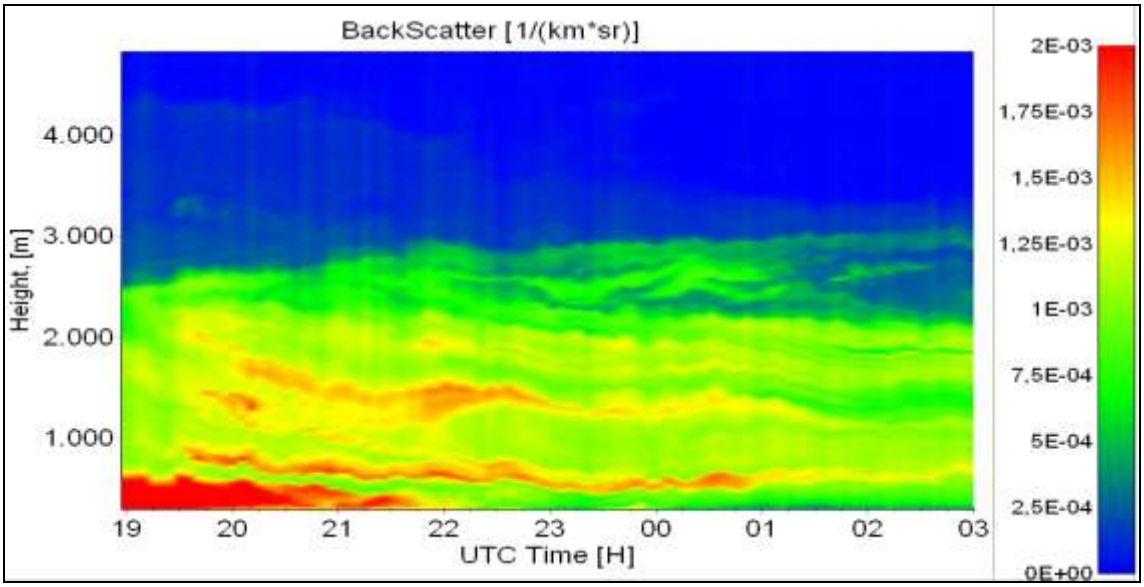

Figure 4.31. The spatial and temporal evolution of total backscattering.

In Figure 4.31, ash layer is indistinguishable, which is due to volume fraction of ash is compared with the volume density of ambient aerosol, thus, this example demonstrates that depolarization technique is very useful for the detection of the intrusions of such layers with low density.

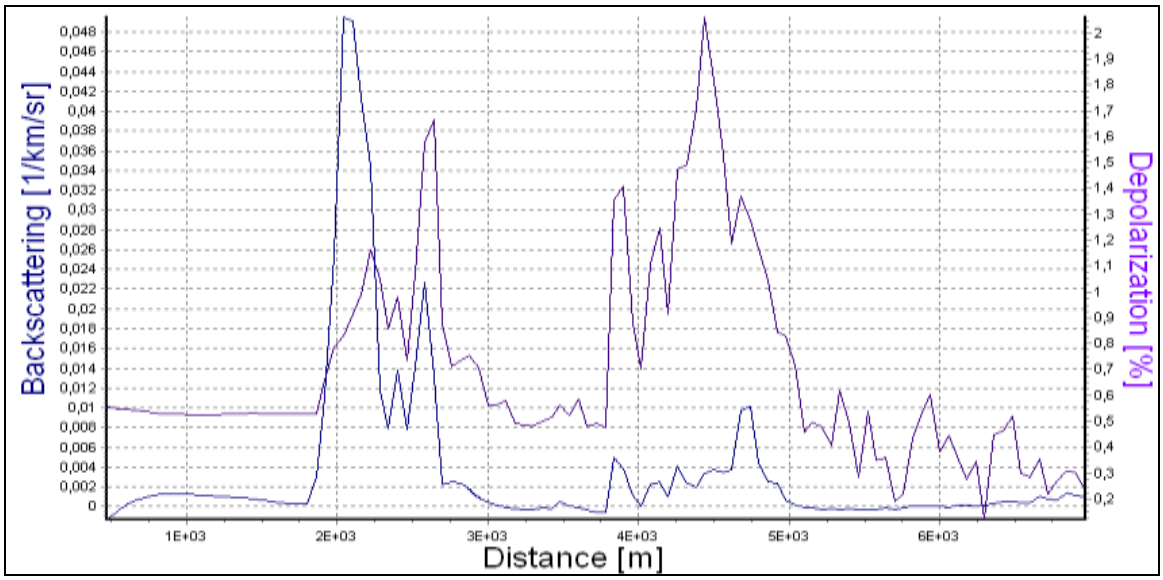

Figure 4.32. Depolarization and backscattering comparison.

In Figure 4.32, backscattering coefficients and polarization values are compared. At the distance between 4000 - 5000 m (2000 - 2500 m height), although there is a small density of aerosols with low backscattering, there is a large value for polarization that suggests the presence of a layer with different properties.

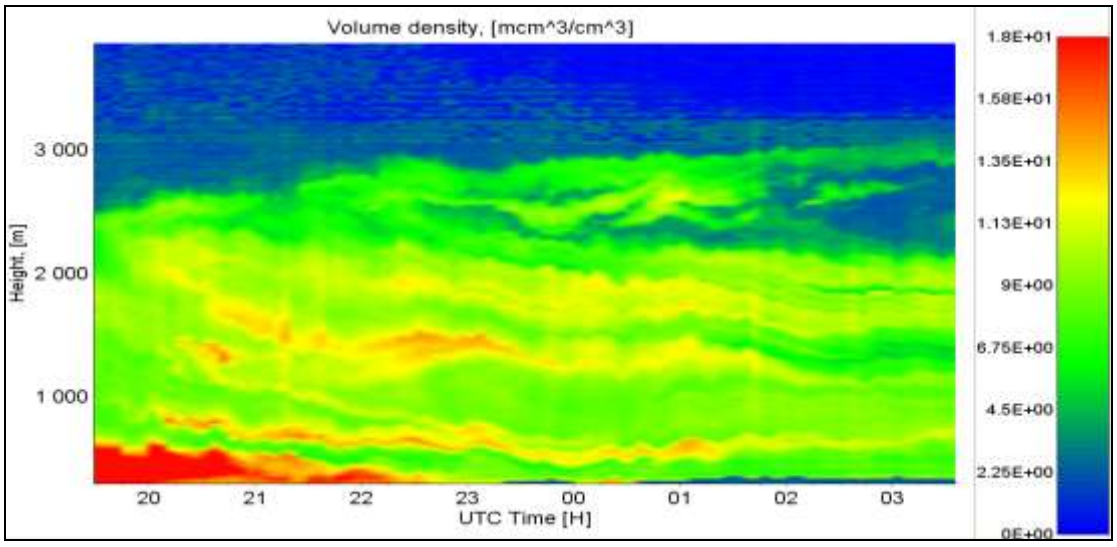

Figure 4.33. Volume density colormap of the ash particles.

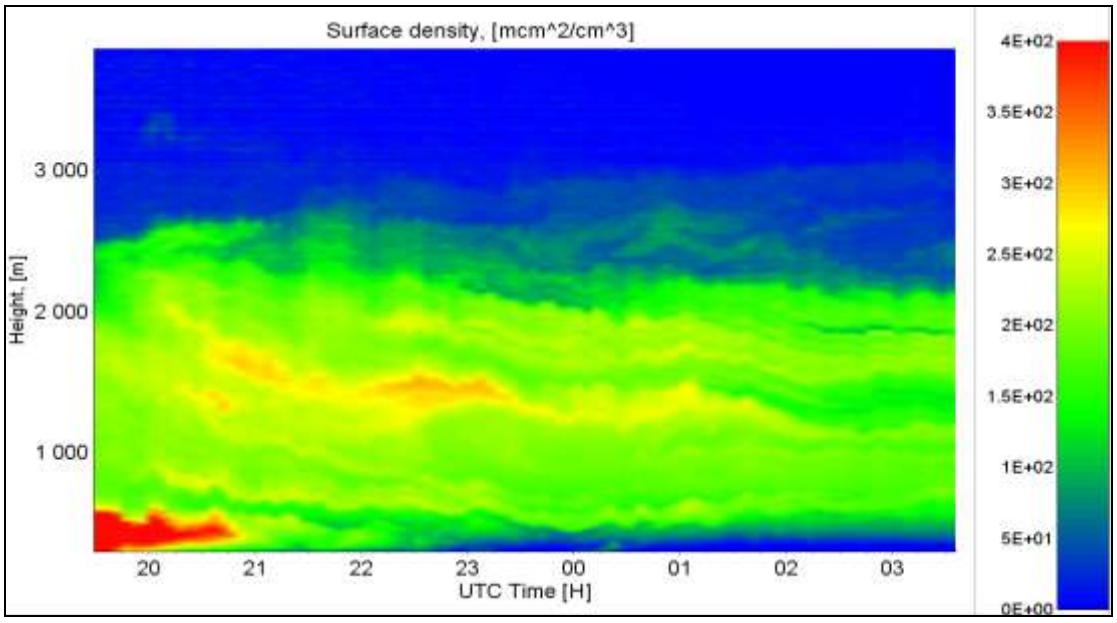

Figure 4.34. Surface density colormap of the ash particles.

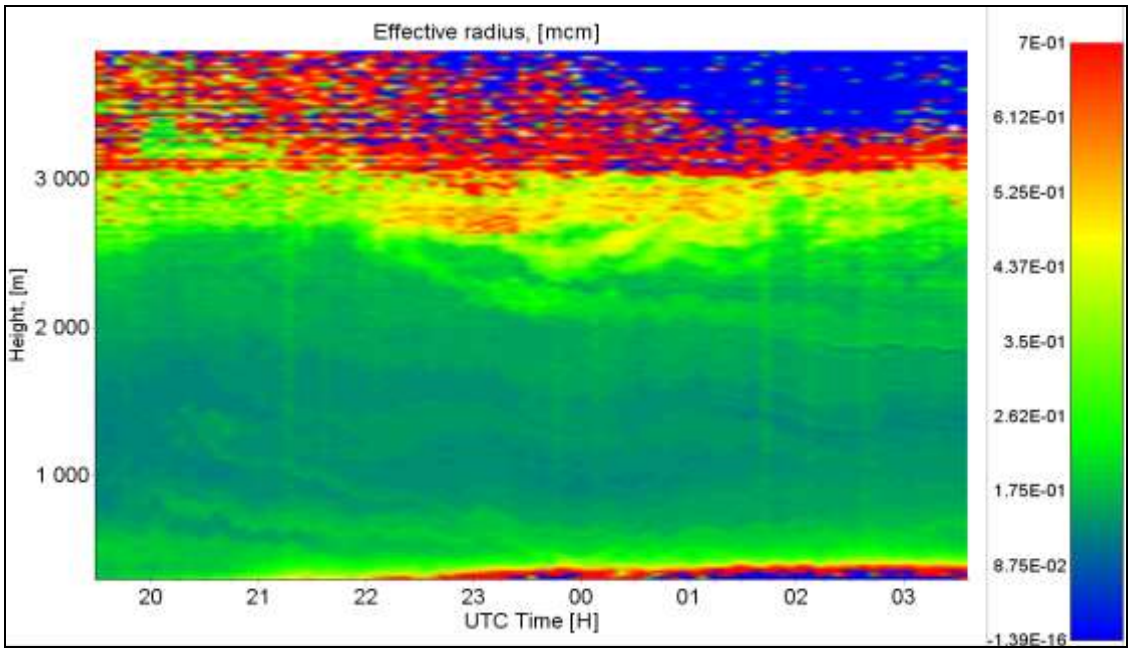

Figure 4.35. Effective radius colormap of the ash particles.

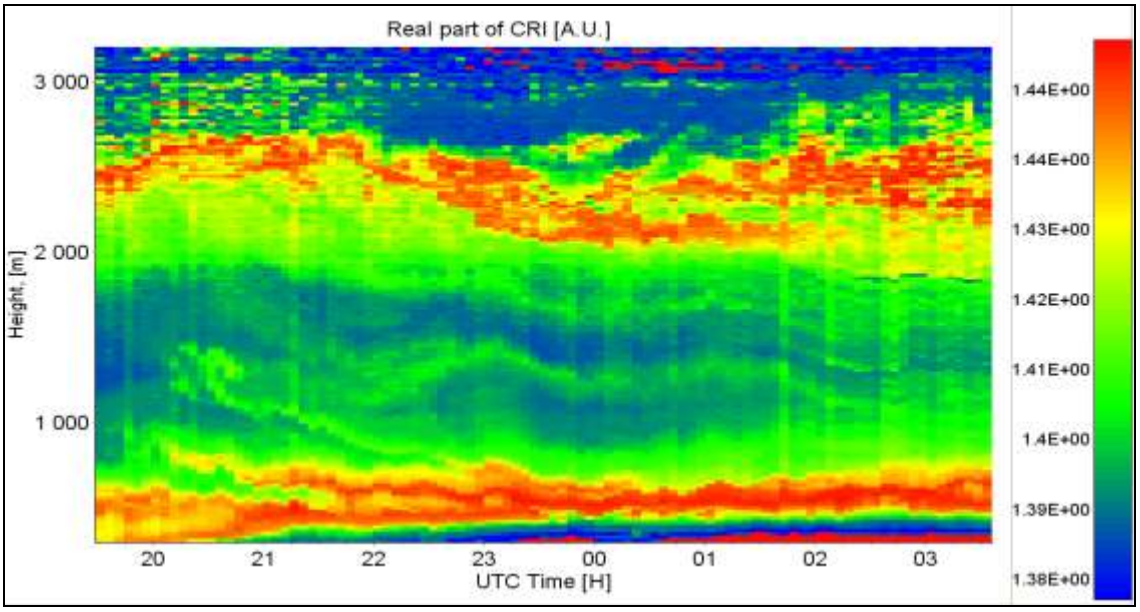

Figure 4.36. Colormap of the real part of complex refractive index of the ash particles.

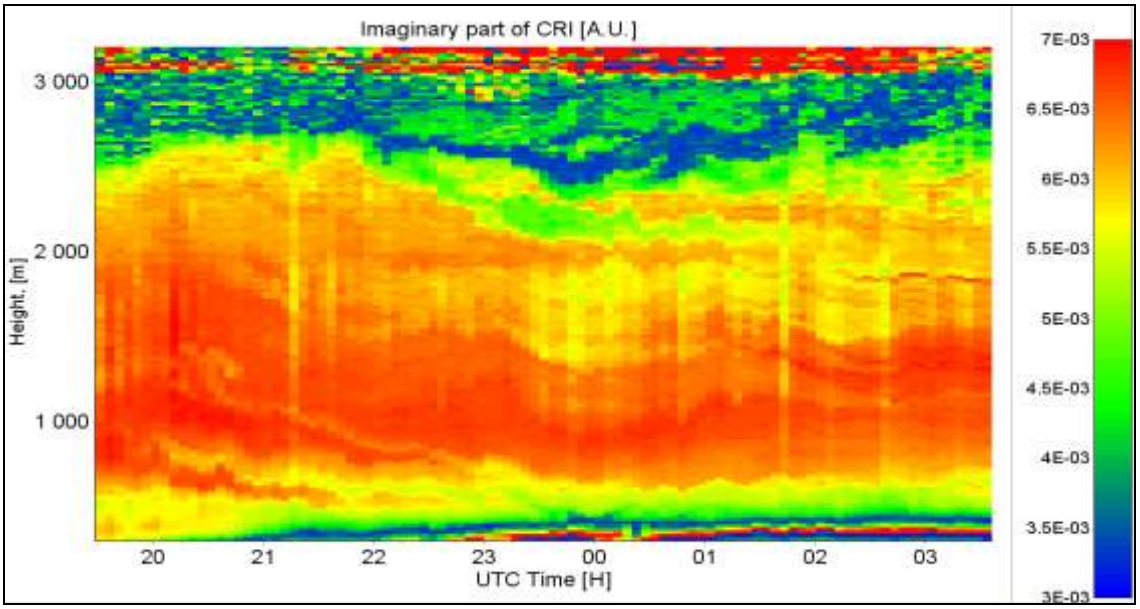

Figure 4.37. Colormap of the imaginary part of complex refractive index of the ash particles.

The microphysical parameters of volcanic ash plumes are demonstrated as colormaps in Figures 4.33 to 4.37. The PCA method was applied to retrieve the particle parameters which proved to be very useful in obtaining the variation of the parameters in a time-series.

4.5. Discussion

One year operation of lidar system demonstrated that the technical decisions used in a multiwavelength Mie-Raman lidar for the measurements of atmospheric aerosol parameters were correct. The maximum distance of measurements of elastic scattering was up to 15 kilometers for all 3 wavelengths, and for Raman signals this distance was about 3 km. Polarization measurements at 355 nm, were carried out for different atmospherical and meterological conditions. In the daytime, only elastic scattering could be recorded, because for Raman channels, the sky background was too high to obtain reliable results. In the future, using the interference filters with lower bandwidth and a telescope with a smaller field-of-view, more reliable results in the day time can be obtained. Due to the high sensitivity, during day time the detector for 608 nm usually shuts down itself, therefore it may be replaced with a more robust detector in the future. Measurements could be done with variable angles with the horizontal, which proved to be a useful option, because it allowed to get the aerosol backscattering and extinction profiles closer to the ground level.

In the framework of this research, a set of new algorithms was developed, adapted and tested. These were:

- Algorithms for calculation of aerosol backscattering and extinction coefficients based on Klett and Raman methods. These algorithms were used to calculate variations of verticle distributions of parameters of aerosols in different seasons. The long term observations allowed to evaluate the temporal variations of of the aerosols scattering coefficients. Presentation of the results as color or 3D maps allowed to visualize such processes as variations of the height of the PBL and intrusions of aerosol layers during the night.

- Algorithms for inversion with regularization for retrieval of particle microphysical parameters from the multiwavelength lidar measurements. These algorithms were used to retrieve PSD. Obtained results allowed to seperate fine and coarse modes of the distribution, which is an important parameter for the

identification of different types of aerosols, for example biomass burning aerosols and desert dust.

- Algorithm for the retrieval of bulk particle properties using principal component analysis approach. This algorithm was based on the principal component analysis, and alloweed to speed up the computations. As a result, for the first time, the temporal evolution of not only backscattering and extinction coefficients, but also particle bulk parameters was evaluated.

The main goal of this research was to develop a system and technology for monitoring atmospheric aerosol parameters. Developed technology allowed to study the seasonal variations of aerosols. The study of seasonal variation is a very complex task and to have complete data about seasonal variations, long term measurements during several years are required. The first steps to achieve this task have been made in this research. Measurements were performed for all key seasons and the main conclusions obtained are as follows:

- In the Spring, the desert aerosols from Sahara arrived to Turkey from the South. Dust intrusions were normally observed at 2 - 3 km height and and these layers were characterized by strong particle depolarization. The typical extinction coefficient in the dust layer was 0.5 km^{-1}.

- Summer was characterized by high aerosol load. The rise of temperature and relative humidity lead to the hygroscopic growth of the particles. Typical values of extinction coefficient at 355 nm inside PBL was around 0.15-0.2 km^{-1}. Also, due to the increased concentrations of biogenic aerosols like pollens and plant debris, the aerosol concentrations were highest in this season.

- In Autumn, it was more or less the same situation with Summer with a decreasing trend in aerosol backscattering and extinction coefficients.

- In the Winter months the aerosol loading was low. Typical aerosol extinction at 355 nm inside PBL in Winter was around 0.05 - 0.07 km^{-1}. The top of PBL varied between 1.0 - 1.5 km. It should be noted, that the measurements in Winter were difficult due to the atmospheric and meteorological conditions: rain and low clouds occurred quite often which effect to obtain reasonable data for long periods to show the variation of scattering coefficients and to retrieve the particle microphysical parameters.

Obtained results allowed to derive the quantitative characteristics of aerosol parameters for these seasons. Results and Discussion chapter, includes representative figures from each season, displaying different trends, however, selected results were presented to be able to emphisize the similarities and differences of the seasonal variations.

The knowledge of the water vapor mixing ratio is important for the study of aerosol hygroscopic growth, because it governs the aerosol radiative forcing effects. Application of Raman technique allowed to measure water vapor mixing ratio with high spatial resolution. In this research, the measurements were performed at 408 nm which is the Raman signal for water vapor. The analysis of the experimental results showed that in the Summer, reliable measurements at 50 m resolution could be performed.

In the Spring of 2010, the volcano eruption at Iceland effected the air traffic over Europe and caused a big chaos at the airports and great losses to airline companies, by erupting high amounts of ash in the atmosphere. This ash was transported over whole Europe and finally reached to Turkey after a month. Developed lidar system was able to detect the intrusion episodes and estimate the main characteristics the ash layers. The use of polarization measurements allowed to detect intrusions of volcanic plumes at 5 km height. It should be mentioned that ash layers were detected through Europe by EARLINET lidars, and the results were included in the special Eyjafyallaöküll section. Results obtained over Gebze were were in accordance with their results. Thus, developed system becames an important part of this global network which allowed to provide information about the global transfer of aerosols over Europe and Asia. In the future, cooperating with the meteorological groups in Turkey and in the world like EARLINET

and AERONET, would promise a better understanding of the atmospheric aerosols for modelling the global climate changes, would provide a oppurtinity for the greater understanding of the atmosphere and the changes within. For this purpose, an invitation from EARLINET to participate in their network was received in Spring 2010 and lidar at TUBITAK MRC will soon be a part of it.

Finally, investigation of atmospheric aerosols by developed multiwavelength Mie-Raman lidar proved to be a very promising tool for the study of the microphyscial properties of aerosols. This research has been a very useful beginning for a different branch or aerosol science in Turkey, and with more regular measurements, and with further develeopments with the system, lidar technology will provide valuable information about the atmosphere and its constituents. The aerosol science in Turkey is mainly centered in the chemistry of in situ samples, however in the future, with an integrated approach, this aerosol portion of the atmosphere can be comprehended further by combining lidar data which measures the physical properties and the existing aerosol science which investigates the chemical properties. The combination of the physical and chemical properties of aerosols will be a significant contribution to aerosol science in Turkey. The lidar system can be modified to measure fluoescence and thus, can make remote speciation. If a specific trace constituent is being searched, the system can work with differential absorption method by transmitting two wavelengths one of which is in the absorbing portion of the constituent and the other not. The difference between the absorption can be measured to detect the selected atmospheric constituent. Another future goal is to use the lidar methodology with a scanning head to obtain data from all directions and integrate the results to a geographical map of the area of lidar measurement to show the spatial and temporal variation of aerosol scattering coefficients and microphysical properties on a map.

The results of this research was published as a poster presentation at the International Conference of Advanced Laser Technologies, ALT'09, Antalya, Turkey, 26 September - 1 October 2009 (Allakhverdiev et al., 2009) and as a paper in Fizika (Allakhverdiev et al., 2010).

REFERENCES

Ackermann, A., Toon, O.B., Taylor, J.P., Johnson, D.W., Hobbs, P.V., Ferek, R.J., 2000. Effects of aerosols on cloud albedo: Evaluation of Twomey's parameterization of cloud susceptibility using measurements of ship tracks. Journal of the Atmospheric Sciences, 57, 2684-2695.

Albrecht, B., 1989. Aerosols, cloud microphysics and fractional cloudiness. Science, 245, 1227-1230.

Allakhverdiev, K., Baykara, T., Bekbolet, M., Huseyinoglu, M.F., Ozbek, S., Salaeva, Z., Secgin, A., Vartapeov, S, Veselovskii, I. 2009. A new multiwavelength Mie-Raman lidar in Turkey, Proceedings of the 17th International Conference on Advanced Laser Technologies, Antalya, Turkey, 26 September - 1 October 2009, 139.

Allakhverdiev, K., Baykara, T., Bekbolet, M., Huseyinoglu, M.F., Ozbek, S., Salaeva, Z., Secgin, A., Vartapeov, S, Veselovskii, I.A., Korenskii, M., 2010. Preliminary results from the new multiwavelength lidar in Turkey. Fizika, 16, 22-25.

Amiridis, V., Melas, D., Balis D.S., Papayannis, A., Founda, D., Katragkou, E., Giannakaki, E., Mamouri R.E., Gerasopoulos, E., Zerefos, C., 2007. Aerosol Lidar observations and model calculations of the Planetary Boundary Layer evolution over Greece, during the March 2006 Total Solar Eclipse. Atmospheric Chemistry and Physics, 7, 6181–6189.

Ansmann, A., Riebesell, M., Wandinger, U., Weitkamp, C., Voss, E. Lahmann, W., Michaelis, W., 1992. Combined Raman elastic-backscatter lidar for vertical profiling of moisture, aerosols extinction, backscatter, and lidar ratio. Applied Physics, B55, 18-28.

Ansmann, A., Wagner, F., Müller, D., Althausen, D., Herber, A., von Hoyningen-Huene, W., Wandinger, U., 2002. European pollution outbreaks during ACE 2: Optical particle properties inferred from multi-wavelength lidar and star-sun photometry. Journal of Geophysical Research, 107, 1109-1111.

Ansmann A., Tesche, M., Knippertz, P., Bierwirth, E., Althausen, D., Muller, D., Schultz, D., 2009. Vertical profiling of convective dust plumes in southern Morocco during SAMUM. Tellus, 61B, 340-353.

Athanasopoulou, E., Tombrou, M., Pandis, S.N., Russell, A. G., 2008. The role of sea-salt emissions and heterogenous chemistry in the air quality of polluted coastal areas. Atmospheric Chemistry and Physics Discussions, 8, 3807-3841.

Bayraktar, H., Turalioglu, S., Tuncel, G., 2010. Average mass concentrations of TSP, PM_{10} and $PM_{2.5}$ in Erzurum urban atmosphere Turkey. Stoch Environmental Risk Assessment, 24, 57-65

Bernstein, J.A., Alexis, N., Barnes, C., Bernstein, I.L., Nel, A., Peden, D., Diaz-Sanchez, D., Tarlo, S.M., Williams, P. B., 2004. Health effects of air pollution. Journal of Allergy and Clinical Immunology, 114, 1116-1123.

Bohren, F.B., Huffman, D., 1983. Absorption and Scattering of Light by Small Particles, John Wiley, New York, 530-531.

Bohren, F.B., Clothiaux, E.E., 2006. Fundamentals of Atmospheric Radiation: An Introduction with 400 Problems, Wiley-VCH Verlag GmbH and Co. KGaA, Weinheim, Germany.

Bösenberg, J., Hoff, R.M., 2008. The GAW Aerosol Lidar Observation Network (GALION), WMO GAW Report, WMO, Geneva, Switzerland.

Cane, M.A., 2005. The evolution of El Niño, past and future. Earth and Planetary Science Letters, 230, 227-240.

Carrico, C.M., Kus, P., Rood, M.J., Quinn, P.K., Bates, T.S., 2003. Mixtures of pollution, dust, sea salt, and volcanic aerosol during ACE-Asia: Radiative properties as a function of relative humidity. Journal of Geophysical Research, 108, 8650-8651.

Cindoruk, S.S., Tasdemir, Y., 2007. Deposition of atmospheric particle PCBs in suburban site of Turkey. Atmospheric Research, 85, 300-309.

Cuesta J., Flamant, P.H., Flamant, C., 2008. Synergetic technique combining elastic backscatter lidar data and sun photometer AERONET inversion for retrieval by layer of aerosol optical and microphysical properties. Applied Optics, 47, 4598- 4611.

De Graaf, M., Donovan, D., Apituley, A., 2008. Refractive index and integral aerosol properties retrieval from Raman lidar data using principle component analysis, Proceedings of ILRC 24, 11-14, 23-27 June 2008, Boulder, USA, 45-49.

De Graaf, M., Donovan, D., Apituley, A., 2009. Aerosol microphysical properties from inversion of tropospheric optical Raman lidar data, Proceedings of 8th ISTP, S06-O08, 19-23 October 2009, Delft, The Netherlands, 237-240.

De Tomasi, F., Bianco, A., Perrone, M.R., 2003. Raman lidar monitoring of extinction and backscattering of African dust layers and dust characterization. Applied Optics, 42, 1699-1709.

Delmelle, P., Stix, J., Bourque, C.P.-A., Baxter, P.J., Garcia-Alvarez J., Barquero, J., 2001. Dry deposition and heavy acid loading in the vicinity of Masaya Volcano, a major sulfur and chlorine source in Nicaragua. Environmental Science and Technology, 35, 1289-1293.

Donovan, D., Carswell, A., 1997. Principal component analysis applied to multiwavelength lidar aerosol backscatter and extinction measurements, Applied Optics, 36, 9406-9424.

Draine, B.T., Flatau, J.P., 1994. Discrete-dipole approximation for scattering calculations. Journal of the Optical Society of America, 11, 1491–1499.

Dubovik, O., Holben, B.N., Eck, T.F., Smirnov, A., Kaufman, Y.J., King, M.D., Tanré, D., Slutsker, I., 2001. Variability of Absorption and Optical Properties of Key Aerosol Types Observed in Worldwide Locations. Journal of the Atmospheric Sciences, 59, 590-608.

Dubovik, O., Holben, B.N., Eck, T.F., Smirnov, A., Kaufman, Y.J., King, M.D., Tanré, D., Slutsker, I., 2002a. Variability of absorption and optical properties of key aerosol types observed in worldwide locations. Journal of the Atmospheric Sciences, 59, 590-608.

Dubovik, O., Holben, B.N., Lapyonok, T., Sinyuk, A., Mishchenko, M.I., Yang, P., Slutsker, I., 2002b. Non-spherical aerosol retrieval method employing light scattering by spheroids. Geophysical Research Letters, 10, 506-511.

Dubovik, O., Sinyuk, A., Lapyonok, T., Holben, B.N., Mishenko, M., Yang, P., Eck, T.F., Volten, H., Munoz, O., Veihelmann, B., van der Zande, W.J., Leon, J.F., Sorokin, M., Slutsker, I., 2006. Application of spheroid models to account for aerosol particle nonsphericity in remote sensing of desert dust. Journal of Geophysical Research, 111, 6619-6622.

Dubovik, O., Smirnov, A., Holben, B.N., 2000. Accuracy assessments of aerosol optical properties retrieved from AERONET sun and sky radiance measurements. Journal of Geophysical Research, 105, 9791-9806.

Duce, R., 1995. Distributions and fluxes of mineral aerosol. In Charlson, R.J., Heintzenberg, J. (Eds), Aerosol Forcing of Climate, John Wiley, Chichester, UK, 43-72.

EARLINET (European Aerosol Research Lidar Network) web site, www.earlinet.org/index.php?id=earlinet_homepage (accessed May 2009).

Ehrenberg, C.G., 1830. Neue Beobachtungen über blutartige Erscheinungen in Aegypten, Arabien und Sibirien, nebst einer Uebersicht und Kritik der früher bekannten, Annalen der Physik und Chemie, 94, 477–514.

Elbert, A., Taylor, P.E., Andreae, M.O., Pöschl, U., 2007. Contribution of fungi to primary biogenic aerosols in the atmosphere: Wet and dry discharged spored, carbohydrates and inorganic ions. Atmospheric Chemistry and Physics, 7, 4569-4588.

Esselborn, M., Wirth, M., Fix, A., Weinzierl, B., Rasp, K., Tesche, M., Petzold, A., 2009. Spatial distribution and optical properties of Saharan dust observed by airborne high spectral resolution lidar during SAMUM 2006. Tellus 61B, 131-143.

Feingold, G., Cotton, W.R., Kreidenweis, S.M., Davis, J.T., 1999. The impact of giant cloud condensation nuclei on drizzle formation in stratocumulus: Implications for cloud radiative properties. Journal of the Atmospheric Sciences, 56, 4100-4117.

Feingold, G., Grund, C.J., 1994. Feasibility of using multi-wavelength lidar measurements to measure cloud condensation nuclei. Journal of Atmospheric and Oceanic Technology, 11, 1543-1558.

Feingold, G., Morley, B., 2003. Aerosol hygroscopic properties as measured by lidar and comparison with in situ measurements. Journal of Geophysical Research, 108, 2842-2849.

Franze, T., Weller, M.G., Niessner, G., Pöschl, U., 2003. Enzyme immunoassays for the investigation of protein nitration by air pollutants. The Analyst, 128, 824-825.

Franze, T., Weller, M.G., Niessner, G., Pöschl, U., 2004. Comparison of nitrotyrosine antibodies and development of immunoassays for the detection of nitrated proteins. The Analyst, 129, 589-590.

Franze, T., Weller, M.G., Niessner, G., Pöschl, U., 2005. Protein nitration by polluted air. Environmental Science and Technology, 39, 1673-1675.

Freudenthaler V., Essselborn, M., Wiegner, M., Heese, B., Tesche, M., Ansmann, A., Muller, D., Althausen, D., Wirth, M., Fix, A., Ehret, G., Knippertz, P., Toledano, C., Gasteiger, J., Garhammer, M., Seefeldner, M., 2009. Depolarization ratio profiling at several wavelengths in pure Saharan dust during SAMUM 2006. Tellus 61B, 165-179.

Fuentes, E., Coe, H., Green, D., de Leeuw, G., McFiggans, G., 2010. Laboratory generated primary marine aerosol via bubble-bursting and atomization. Atmospheric Measurement Technology, 3, 141-162.

Fiocco, G., Smullin, L.O., 1963. Detection of scattering layers in the upper atmosphere (60-140 Km) by optical radar. Nature, 199, 1275.

Fuzzi, S., Andreae, M.O., Huebert, B.J., Kulmala, M., Bond, T.C., Boy, M., Doherty, S.J., Guenther, A., Kanakidou, M., Kawamura, K., Kerminen, V.M., Lohmann, U., Russell, L.M., Pöschl, U., 2006. Critical assessment of the current state of scientific knowledge, terminology, and research needs concerning the role of organic aerosols in the atmosphere, climate, and global change. Atmospheric Chemistry and Physics, 6, 2017–2038.

Gard, E.E., Kleman, M.J., Gross, D.S., Hughes, L.S., Allen, J.O., Morrical, B.D., Fergenson, D.P., Dienes, T., Galli, M.E., Johnson, R.J., Cass, G.R., Prather, K.A., 1998. Direct observations of heterogenous chemistry in the atmosphere. Science, 279, 1184-1187.

Garrison, V.H., Shinn, E.A., Foreman, W.T., Griffin, D.W., Holmes, C.W., Kellogg, C.A., Majewski, M.S., Richardson, L.L., Ritchie, K.B., Smith, G.W., 2003. African and Asian dust: From desert soils to coral reefs. BioScience, 53, 469-480.

Geron, C., 2009. Carbonaceous aerosol over a Pinus taeda forest in Central North Carolina, USA. Atmospheric Environment, 43, 959–969.

Gill, S., Lobenberg, R., Ku, T., Azarmi, S., Roa, W. Prenner, E.J., 2007. Nanoparticles: characteristics and mechanisms of action, and toxicity in pulmonary drug delivery: A review. Journal of Biomedical Nanotechnology, 3, 107-119.

Ginoux, P., Prospero, J.M., Torres, O., Chin, M., 2004. Long term simulation of global dust distribution with the GOCART model: Correlation with North Atlantic Oscillation. Environmental Modelling and Software, 19, 113-128.

Goudie, A.S., Middleton, N.J., 1992. The changing frequency of dust storms through time. Climate Change, 20, 197-225.

Graf, H.-F., Langmann, B., Feichter, J., 1998. The contribution of Earth degassing to the atmospheric sulfur budget. Chemical Geology, 147, 131-145.

Grattan, J., Durand, M., Taylor, S., 2003. Illness and elevated human mortality in Europe coincident with the Lake Fissure eruption. In Oppenheimer, C., Pyle, D.M., Barclay, J. (Eds), Volcanic Degassing, 401-414, Geological Society of London, Special Publication.

Gronenberg, D.A., Witt, C., Wagner, U., Chung, K.F., Fischer, A., 2003. Fundamentals of pulmonary drug delivary. Respiration Medicine, 97, 79-89.

Havers, N., Burba, P., Lambert, J., Klockow, D., 1998. Spectroscopic characterization of humic-like substances in airborne particulate matter. Journal of Atmospheric Chemistry, 29, 45-54.

Haywood, J., Boucher, O., 2000. Estimates of the direct and indirect radiative forcing due to tropospheric aerosols: A review. Reviews of Geophysics, 38, 513-543.

Haywood J., Francis, P., Osborne, S., Glew, M., Loeb, N., Highwood, E., Tanré, D., Myhre, G., Formenti, P., Hirst, E., 2003. Radiative properties and direct radiative effect of Saharan dust measured by the C-130 aircraft during SHADE: 1. Solar spectrum. Journal of Geophysical Research, 108, 8577-8579.

Heighton, J.T., Ding, Y., Griggs, D.J., Noguer, M., van der Linden, P.J., Dai, X., Maskell, K., Johnson, C.A., (Eds) 2001. Climate Change 2001: The Scientific Basis, Cambridge University Press, Cambridge, United Kingdom and New York, NY, USA.

Heintzenberg J., 2009. The SAMUM-1 experiment over Southern Marocco: Overview and introduction. Tellus 61B, 2-11.

Holben, B.N., Eck, T.F., Slutsker, I., Tanre, D., Buis, J.P., Setzer, A., Vermote, E., Reagan, J.A., Kaufman, Y.J., Nakajima, T., Lavenu, F., Jankowiak, I., Smirnov, A., 1998. AERONET - A federated instrument network and data archive for aerosol characterization. Remote Sensing of Environment, 66, 1-16.

International Panel on Climate Change 2001 web site, The IPCC Assessment Reports, www.ipcc.ch/publications_and_data/publications_ipcc_fourth_assessment_report_wg1_report_the_physical_science_basis.htm (accessed January 2010).

International Panel on Climate Change 2007 web site. Chapter 1: Historical Overview of Climate Change Science. IPCC WG1 AR4 Report, www.ipcc.ch/publications_and_data/ar4/wg1/en/contents.html (accessed January 2009).

International Panel on Climate Change 2001 web site. Working Group I, www.grida.no/publications/other/ipcc_tar/?src=/climate/ipcc_tar/wg1/160.htm (accessed August 2008).

Janhall, S., Andreae, M.O., Pöschl, U., 2010. Biomass burning aerosol emissions from vegetation fires: Particle number and mass emission factors and size distributions. Atmospheric Chemistry and Physics, 10, 1427–1439.

Jickells, T.D., An, Z.S., Andersen, K.K., Baker, A.R., Bergametti, G., Brooks, N., Cao, J.J., Boyd, P.W., Duce, R.A., Hunter, K.A., Kawahata, H., Kubilay, N., laRoche, J., Liss, P.S., Mahowald, N., Prospero, J.M., Rigdewell, A.J., Tegen, I., Torres, R., 2005. Global iron connections between desert dust, ocean biogeochemistry, and climate. Science, 308, No: 5718, 67-71.

Karaca, F., Al-Agha, O., Erturk, F., 2005. Statistical characterization of atmospheric PM_{10} and $PM_{2.5}$ concentrations at a non-impacted suburban site of Istanbul, Turkey. Chemosphere, 59, 1183-1190.

Karakas, S.Y., Tuncel, S. G., 1998. Chemical characteristics of atmospheric aerosols in a rural site of northwestern Anatolia. Atmospheric Environment, 31, 2933-2943.

Kaufman, Y.J., Tanra, D., Boucher, O., 2002. A satellite view of aerosols in the climate system. Nature, 419, 215-223.

Kiehl, J.T., Trenberth, K.E., 1997. Earth's Annual Global Mean Energy Budget. Bulletin of the American Meteorological Society, 78, 197–208.

Kindap, T., Unal, A., Chen, S-C., Hu, Y., Odman, M.T., Karaca, M., 2006. Long-range aerosol transport from Europe to Istanbul, Turkey. Atmospheric Environment, 40, 3536-3547.

Klett, J.D., 1981. Stable analytical inversion solution for processing lidar returns. Applied Optics, 20, 211-220.

Kocak, M., Theodosi, C., Zarmpas, P., Im, U., Bougiatioti, A., Yenigun, O., Mihalapoulos, N., 2010. Particulate matter (PM_{10}) in Istanbul: Origin, source areas and potential impact on surrounding regions. Atmospheric Environment, accepted manuscript.

Kreidenweis, S.M., Petters, M.D., DeMott, P.J., 2006. Deliquescence-controlled activation of organic aerosols. Geophysical Research Letters, 33, 863-866.

Kreyling, W.G., Semmler-Behnke, M., Moller, W., 2006. Ultrafine particle-lung interactions: Does size matter?. Journal of Aerosol Medicine, 19, 74-83.

Kumar, P.P., Broekhuizen, K., Abbatt, J.P.D., 2003. Organic acids as cloud condensation nuclei: Laboratory studies of highly soluble and insoluble species. Atmospheric Chemistry and Physics, 3, 509-520.

Ligda, M.G.H., 1963. Proceedings of the 1st Conference on Laser Technology, San Diego, CA, U.S.Navy ONR, 63-72.

Li-Jones, X., Prospero, J.M., 1998. Variations in the size distribution of non-sea-salt sulfate aerosol in the marine boundary layer at Barbados: Impact of African dust. Journal of Geophysical Research, 103, 73-84.

Liu, Z.Y., Omar, A., Vaughan, M., Hair, J., Kittaka, J., Hu, Y., Powell, K., Trepte, C., Winker, D., Hostetler, C., Ferrare, R., Pierce, R., 2008. CALIPSO lidar observations of the optical properties of Saharan dust: A case study of long-range transport. Journal of Geophysical Research, 113, 72-77.

MacKinnon, D.J., 1969. The effect of hygroscopic particles on the backscattered power from a laser beam. Journal of the Atmospheric Sciences, 26, 500-510.

Mather, T.A., Pyle, D.M., Oppenheimer, C., 2003. Tropospheric volcanic aerosol. Geophysical Monograph, 139, 189-199.

McTainsh, G., Chan, Y., McGowan, H., Leys, J., Tews, K., 2005. The 23rd October 2002 dust storm in eastern Australia: Characteristics and meteorological conditions. Atmospheric Environment, 39, 1227-1236.

Middleton, W.E.K., Spilhaus, A.F., 1953. Meteorological Instruments, University of Toronto Press, Toronto, 156-158.

Mishchenko, M.I., Hovenier, J.W., Travis, L.D. (Eds), 2000. Light Scattering by Nonspherical Particles, Academic Press, San Diego.

Mishchenko, M.I., Lacis, A.A., Carlson, B.E., Travis, L.D., 1995. Nonsphericity of dust-like tropospheric aerosols: Implications for aerosol remote sensing and climate modeling. Geophysical Research Letters, 22, 1077-1080.

Mishchenko, M.I., Travis, L.D., 1994. T-matrix computations of light scattering by large spheroidal particles. Optical Community, 109, 16-21.

Mishchenko, M.I., Travis, L.D., Lacis, A.A. (Eds), 2002. Scattering, Absorption, and Emission of Light by Small Particles, Cambridge University Press, Cambridge.

Mona, L., Amodeo, A., Pandolfi, M., Pappalardo, G., 2006. Saharan dust intrusions in the Mediterranean area: Three years of Raman lidar measurements. Journal of Geophysical Research, 111, 6569-6571.

Moulin, C., Lambert, C.E., Dulac F., Dayan, U., 1997. Control of atmospheric export of dust from North Africa by the North Atlantic Oscillation. Nature, 387, 691-694.

Müller, D., Ansmann, A., Wagner, F., Franke, K., Althausen, D., 2002. European pollution outbreaks during ACE 2: Microphysical particle properties and single-scattering albedo inferred from multi-wavelength lidar observations. Journal of Geophysical Research, 107, 1110-1114.

Müller, D., Wandinger, U., Ansmann, A., 1999. Microphysical particle parameters from extinction and backscatter lidar data by inversion with regularization: Theory. Applied Optics, 38, 2346-2357.

NASA Goddard Space Flight Center web site.
svs.gsfc.nasa.gov/vis/a000000/a002800/a002842/ (accessed November 2008).

Ning, Z., Sioutas, C., 2009. Atmospheric processes influencing aerosols generated by combustion and the inference of their impact on public exposure: A review. Aerosol and Air Quality Research, 10, 43-58.

Nobel Foundation Official web site, 2007 Nobel Leurates.
nobelprize.org/nobel_prizes/lists/2007.html (accessed September 2008).

Oberdorster, G., 2003. Effects and Fate of Inhaled Ultrafine Particles. Nanotechnology and the Environment, 7, 37-59.

O'Dowd, C.D., Facchini, M.C., Cavalli, F., Ceburnis, D., Mircea, M., Decesari, S., Fuzzi, S., Yoon, Y.J., Putaud, J.P., 2004. Biogenically driven organic contribution to marine aerosol. Nature, 431, 676-680.

Oppenheimer, C., Pyle, D.M., Barclay, J. (Eds), 2003. Volcanic Degassing, The Geological Society of London, Special Publication, 213-218.

Pahlow, M., Feingold, G., Jefferson, A., Andrews, E., Ogren, J.A., Wang, J., Lee, Y.-N., Ferrare, R.A., Turner, D.D., 2006. Comparison between lidar and nephelometer measurements of aerosol hygroscopicity at the Southern Great Plains Atmospheric Radiation Measurement site. Journal of Geophysical Research, 111, 646-649.

Pasteur, L., 1860. Suite a une precedente communication relative aux generations dites spontanees. Comptes rendus hebdomadaires des seances de l'Academie des sciences, 51, 75–78.

Penner, J.E., Chuang, C.C., Grant, K., 1998. Climate forcing by carbonaceous and sulphate aerosols. Climate Dynamics, 14, 839-851.

Perrone, M.R., Barnaba, F., De Tomasi, F., Gobbi, G.P., Tafuro, A.M., 2004. Imaginary refractive-index effects on desert-aerosol extinction versus backscatter relationships at 351 nm: Numerical computations and comparison with Raman lidar measurements. Applied Optics, 43, 531-541.

Peters, A. Pope, C.A., 2002. Cardiopulmonary mortality and air pollution. Lancet, 360, 1184-1185.

Pincus, R., Baker, M.B., 1994. Effect of precipitation on the albedo susceptibility of clouds in the marine boundary layer. Nature, 372, 250-252.

Pöschl, U., 2005. Atmospheric aerosols: Composition, transformation, climate and health effects. Angewandte Chemie International Edition, 44, 7520-7540.

Prospero, J.M., Nees, R.T., 1986. Impact of the North African drought and El Nino on mineral dust in the Barbados trade winds. Nature, 320, 735-738.

Qian, W., Quan, L., Shi, S., 2001. Variations of the dust storm in China and its climatic control. Journal of Climate, 15, 1216-1229.

Raut, J.-C., Chazette, P., 2007. Retrieval of aerosol complex refractive index from a synergy between lidar, sun photometer and in situ measurements during LISAIR experiment. Atmospheric Chemistry and Physics, 7, 2797-2815.

Reid, J.S., Koppmann, R., Eck, T.F., Eleuterio, D.P., 2005a. A review of biomass burning emissions part II: Intensive physical properties of biomass burning particles. Atmospheric Chemistry and Physics, 5, 799– 825.

Reid, J.S., Eck, T.F., Christopher, S.A., Koppmann, R., Dubovik, O., Eleuterio, D.P., Holben, B.N., Reid, E.A., Zhang, J., 2005b. A review of biomass burning emissions part III: Intensive optical properties of biomass burning particles. Atmospheric Chemistry and Physics, 5, 827-849.

Robertson, A.D., Overpeck, J.T., Rind, D., Mosley-Thompson, E., Zielinski, G.A., Lean, J.L., Koch, D., Penner, J.E., Tegen, I., Healy, R., 2001. Hypothesized climate forcing time series for the last 500 years. Journal of Geophysical Research, 106, 14.783-14.803.

Robinson, A.L., Donahue, N.M., Shrivastava, M.K., Weitkamp, E.A., Sage, A.M., Grieshop, A.P., Lane, T.E., Pierce, J.R., Pandis, S.N., 2007. Rethinking organic aerosols: Semivolatile emissions and photochemical aging. Science, 315, 1259–1262.

Robock, A., 2002. Pinatubo eruption: The climatic aftermath. Science, 295, 1242-1244.

Russo, F., 2007. An Investigation of Raman Lidar Aerosol Measurements and Their Application to the Study of the Aerosol Indirect Effect, PhD Thesis, University of Maryland.

Saldiva, P.H.N., Clarke, R.W., Coull, B.A., Stearns, R.C., Lawrence, J., Murthy, G.G.K., Diaz, E., Koutrakis, P., Suh, H., Tsuda, A., Godleski, J.J., 2002. Lung inflammation induced by concentrated ambient air particles is related to particle composition. American Journal of Respiratory and Critical Care Medicine, 165, 1610-1617.

Samura, A., Al-Agha, O., Tuncel, S., 2003. Study of trace and heavy metals in rural and urban aerosols of Uludag and Bursa (Turkey). Water, Air and Soil Pollution: Focus, 3, 111-129.

Scholes, M., Andreae, M.O., 2000. Biogenic and pyrogenic emissions from Africa and their impact on the global atmosphere. Ambio, 29, 23-29.

Schulz, H., Harder, V., Ibald-Mulli, A., Khandoga, A., Koenig, W., Krombach, F., Radykewicz, R., Stampfl, A., Thorand, B., Peters, A., 2005. Cardiovascular effects of fine and ultrafine particles. Journal of Aerosol Medicine, 18, 1-22.

Seinfeld, J., Pandis, S.N., 2006. Atmospheric Chemistry and Physics: From Air Pollution to Climate Change, Second Edition, John Wiley and Sons, Inc.

Sekiguchi, M., Nakajima, T., Suzuki, K., Kawamoto, K., Higurashi, A., Rosenfeld, D., Sano, I., Mukai, S., 2003. A study of the direct and indirect effects of aerosols using global satellite data sets of aerosol and cloud parameters. Journal of Geophysical Research, 108, 4699-4703.

Sokolik, I.N., Winker, D.M., Bergametti, G., Gilette, D.A., Carmichael, G., 2001. Introduction to special section: Outstanding problems in quantifying the radiative impacts of mineral dust. Journal of Geophysical Research, 106, 18.015-18.027.

Solomon, S., Qin, D., Manning, M., Chen, Z., Marquis, M., Averyt, K.B., Tignor, M., Miller, H.L. (Eds), 2007. Contribution of Working Group I to the Fourth Assessment Report of the Intergovernmental Panel on Climate Change, Cambridge University Press, Cambridge, United Kingdom and New York, NY, USA.

Stevenson, D.S., Johnson, C.E., Collins, W.J., Derwent, R.G., 2003. The tropospheric sulphur cycle and the role of volcanic SO_2. In Oppenheimer, C., Pyle, D.M., Barclay, J. (Eds), Volcanic Degassing, The Geological Society of London, Special Publication, 295-305.

Swietlicki, E., Hansson, H.C., Hameri, K., Svenningsson, B., Massling, A., McFiggans, G., McMurray, P.H., Petaja, T., Tunved, P., Gysel, M., Topping, D., Weingartner, E., Baltensperger, U., Rissler, J., Wiedensohler, A., Kulmala, M., 2008. Hygroscopic properties of submicrometer atmospheric aerosol particles measured with H-TDMA instruments in various environments: A review. Tellus 60B, 432-469.

Svenningsson, B., Rissler, J., Swietlicki, E., Mircea, M., Bilde, M., Facchini, M.C., Decesari, S., Fuzzi, S., Zhou, J., Monster, J., Rosenorn, T., 2006. Hygroscopic growth and critical super saturations for mixed aerosol particles of inorganic and organic compounds of atmospheric relevance. Atmospheric Chemistry and Physics, 6, 1937-1952.

Tanré, D., Haywood, J., Pelon, J., Leon, J.F., Chatenet, B., Formenti, P., Francis, P., Goloub, P., Highwood, E.J., Myhre, G., 2003. Measurement and modeling of the Saharan dust radiative impact: Overview of the Saharan Dust Experiment (SHADE). Journal of Geophysical Research, 108, 8574.

Tasdemir, Y., Kural, C., 2005. Atmospheric dry deposition fluxes of trace elements measured in Bursa, Turkey. Environmental Pollution, 138, 462-472.

Tegen, I., Fung, I., 1995. Contribution to the atmospheric mineral aerosol load from land surface modification. Journal of Geophysical Research, 100, 707-726.

Tegen, I., Hollrigl, P., Chin, M., Fung, I., Jacob, D., Penner, J., 1997. Contribution of different aerosol species to the global aerosol extinction optical thickness: Estimates from model results. Journal of Geophysical Research, 102, 895-915.

Tegen, I., Werner, M., Harrison, S.P., Kohfeld, K.E., 2004. Relative importance of climate and land use in determining present and future global soil dust emission. Geophysical Research Letters, 31, 9216-9219.

Tesche M., Ansmann, A., Muller, D., Althausen, D., Mattis, I., Heese, B., Freudenthaler, V., Wiegner, M., Esselborn, M., Pisani, G., Knippertz, P., 2009. Vertical profiling of Saharan dust with Raman lidars and airborne HSRL in southern Morocco during SAMUM. Tellus 61B, 144-164.

Theodosi, C., Im, U., Bougiatioti, A., Zarmpas, P., Yenigun, O., Mihalapoulos, N., 2010. Aerosol chemical composition over Istanbul. Science of the Total Environment, 408, 2482-2491.

Tikhonov, A.N., Arsenin, V.Y. (Eds), 1977. Solution of Ill-Posed Problems, Wiley, New York.

Turkum, A., Pekey, H., Pekey, B., Tuncel, G., 2008. Investigating relationships between aerosol and rainwater compositions in different locations in Turkey. Atmospheric Research, 89, 315-323.

Twomey, S., 1974. Pollution and the planetary albedo. Atmospheric Environment, 8, 1251-1256.

Twomey, S. (Ed), 1977. Introduction to the Mathematics of Inversion in Remote Sensing and Direct Measurements, Elsevier, New York.

United States Geological Survey web site, volcanoes.usgs.gov/about/edu/dynamicplanet/index.php (accessed, December, 2009).

Weitkamp, C., (Ed), 2002. Lidar: Range-Resolved Optical Remote Sensing of the Atmosphere, Springer, USA.

Wiegner M., Gasteiger, J., Kandler, K., Weinzierl, B., Rasp, K., Esselborn, M., Freudenthaler, V., Heese, B., Toledano, C., Tesche, M., Althausen, D., 2009. Numerical simulations of optical properties of Saharan dust aerosols with emphasis on lidar applications. Tellus 61B, 180-194.

Wulfmeyer, V., Feingold, G., 2000. On the relationship between relative humidity and particle backscattering coefficient in the marine boundary layer determined with differential absorption lidar. Journal of Geophysical Research, 105, 4729-4741.

Xie, C., Nishizawa, T., Sugimoto, N., Matsui, I., Wang, Z., 2008. Characterization of aerosol optical properties in pollution and Asian dust episodes over Beijing, China, Applied Optics, 47, 4945-4951.

Veselovskii, I.A., Kolgotin, A., Griaznov, V., Müller, D., Franke, K., Whiteman, D.N., 2004. Inversion of multi-wavelength Raman lidar data for retrieval of bimodal aerosol size distribution. Applied Optics, 43, 1180-1195.

Veselovskii, I.A., Kolgotin, A., Griaznov, V., Müller, D., Wandinger, U., Whiteman, D.N., 2002. Inversion with regularization for the retrieval of tropospheric aerosol parameters from multiwavelength lidar sounding. Applied Optics, 41, 3685-3699.

Veselovskii, I.A., Korenskii, M., Griaznov, V., Whiteman, D.N., McGill, M., Roy, G., Bissonnette, L., 2006. Information content of data measured with a multiple-field-of-view lidar. Applied Optics, 45, 6839-6848.

Veselovskii, I.A., Whiteman, D.N., Kolgotin, A., Andrews, E., Korenskii, M., 2009. Demonstration of aerosol property profiling by multi-wavelength lidar under varying relative humidity conditions. Journal of Atmospheric and Oceanic Technology, 26, 1543-1557.

Vrekoussis, M., Liakakou, E., Kocak, M., Kubilay, N., Oikonomou, K., Sciare, J., Mihalapoulos, N., 2005. Seasonal variety of optical properties of aerosols in the Eastern Mediterranean. Atmospheric Environment, 39, 7083-7094.

Yang, P., Liou, K.N., Mishchenko, M.I., Gao, B.C., 2000. Efficient finite-difference time-domain scheme for light scattering by dielectric particles: Application to aerosols. Applied Optics, 39, 3727-3737.

Yang, P., Feng, Q., Hong, G., Kattawar, G.W., Wiscombe, W.J., Mishchenko, M.I., Dubovik, O., Laszlo, I, Sokolik, I. N., 2007. Modeling of the scattering and radiative properties of nonspherical dust-like aerosols. Journal of Atmospheric Science, 38, 995-1014.

Yang, W, Peters, J.I., Williams III, R.O., 2008. Inhaled nanoparticles: A current review. International Journal of Pharmaceutics, 356, 239-247.

Yatin, M., Tuncel, S., Aras, N.K., Olmez, I., Aygun, S., Tuncel, G., 2000. Atmospheric trace elements in Ankara, Turkey: 1. Factors effecting chemical composition of particles. Atmospheric Environment, 34, 1305-1318.

Zhang, Q., Jimenez, J.L., Canagaratna, M.R., Allan, J.D., Coe, H., Ulbrich, I., Alfarra, M.R., Takami, A., Middlebrook, A.M., Sun, Y.L., Dzepina, K., Dunlea, E., Docherty, K., De-Carlo, P.F., Salcedo, D., Onasch, T., Jayne, J.T., Miyoshi, T., Shimono, A., Hatakeyama, S., Takegawa, N., Kondo, Y., Schneider, J., Drewnick, F., Borrmann, S., Weimer, S., Demerjian, K., Williams, P., Bower, K., Bahreini, R., Cottrell, L., Griffin, R. J., Rautiainen, J., Sun, J.Y., Zhang, Y.M., Worsnop, D.R., 2007. Ubiquity and dominance of oxygenated species in organic aerosols in anthropogenically-influenced Northern Hemisphere midlatitudes. Geophysical Research Letters, 34, 9979-9984.

REFERENCES NOT CITED

Asian Dust Network (AD-Net) web site, www-lidar.nies.go.jp/AD-Net (accessed February 2010).

Commonwealth of Independent States Lidar Network (CIS-LINET) web site, www.cis-linet.basnet.by (accessed January 2010).

Dubovik, O., King, M., 2000. A flexible inversion algorithm for retrieval of aerosol optical properties from sun and sky radiance measurements. Journal of Geophysical Research, 105, 20.673-20.696.

Garcia, M.A., Sanchez, M.L., de Torre, B., Perez, I.A., 2007. Characterisation of the mixing height temporal evolution by means of a laser dial system in an urban area: Intercomparison results with a model application. Annales Geophysicae, 25, 2119–2124.

Georgoussis, G., Chourdakis G., Landulfo E., Hondidiadis K., Ikonomou A., 2006. Monitoring of air pollution and atmospheric parameters using a mobile backscatter lidar system. Óptica Pura Y Aplicada, 39, 35-36.

Griaznov, V., Veselovskii, I.A., Di Girolamo, P., Demoz, B., Whiteman, D., 2004. Numerical simulation of light backscattering by spheres with off-center inclusion: Application to the lidar case. Applied Optics, 43, 5512-5522.

Guillot, P., 1983. Optical methods of remote sensing of atmospheric pollution. Spectrochimica Acta, 38B, 1457-1464.

Hanel, G., 1976. The properties of atmospheric aerosol particles as functions of the relative humidity at thermodynamic equilibrium with the surrounding moist air. Advanced Geophysics, 19, 74-188.

Heese, B., Freudenthaler, V., Kosmale, M., Seefeldner, M., Wiegner, M., 2004. First results from the portable Lidar system POLIS, Proceedings of the 22nd International Laser Radar Conference, Matera, Italy, July 12-16, 2004.

Hinkley, E.D. (Ed),1976. Laser Monitoring of the Atmosphere, Springer-Verlag, USA.

Kolev, N., Iliev. I., Evgenieva, T., Kaprielov, B., Kolev, I., Devara, P., Raj, P.E., Dani, K.K., 2009. Lidar, sunphotometer and spectroradiometer measurements of the atmospheric aerosol characteristics. International Journal of Remote Sensing, 30, 6381- 6401.

Kolev, N., Tatarov, B., Iliev, I., Kaprielov, B., Kolev, I., 2005. Lidar and spectrophotometer investigation of the air quality over Sofia (Bulgaria): Preliminary results. Geophysical Research Abstracts, 7, 85-87.

Lohmann, U., Feichter, J., 2005. Global indirect aerosol effects: A review. Atmospheric Chemistry and Pyhsics, 5, 715–737.

Mayor, S.D., Spuler S.M., 2004. Raman-shifted eye-safe aerosol lidar. Applied Optics, 43, 3915-3924.

Mayor, S.D., Spuler, S.M., Morley, B.M., Loew, E., 2007. Polarization lidar at 1.54 μm and observations of plumes from aerosol generators. Optical Engineering 46, 096201.

Mishchenko, M.I., Travis, L.D., Kahn, R.A., West, R.A., 1997. Modeling phase functions for dustlike tropospheric aerosols using a mixture of randomly oriented polydisperse spheroids. Journal of Geophysical Research, 102, 16831-16847.

Network for the Detection of Atmospheric Composition Change (NDACC) www.ndsc.ncep.noaa.gov (accessed January 2010).

Okada, K., Naruse, H., Tanaka, T., Nemato, O., Iwasaka, Y., Wu, P. Ono, A., Duce, R.A., Uematsu, M., Merrill, J.T., Arao, K., 1990. X-ray spectrometry of Individual Asian Dust-storm particles over the Japanese Islands And the North Pacific Ocean. Atmospheric Environment, 24, 1369-1378.

Pappalardo, G., 2005. Aerosol lidar ratio measurements in the framework of EARLINET. Geophysical Research Abstracts, 7, 8329.

Pappalardo, G., 2010. EARLINET correlative measurements for CALIPSO: First intercomparison results. Journal of Geophysical Research, 115, 2147-2149.

Raman, C.V., 1928. A new radiation. Indian Journal of Physics, 2, 387-398.

Ristoria, P., Oteroa L., Fochesattoa, J., Flamantb, P.H., Wolframa, E., Quela, E., Piacentinic, R., Holben B., 2003. Aerosol optical properties measured in Argentina: wavelength dependence and variability based on sun photometer measurements. Optics and Lasers in Engineering 40, 91–104.

The International Network for the Detection of Atmospheric Composition Change (NDACC) web site ndacc-lidar.org (accessed January 2010).

The NASA Micro-Pulse Lidar Network (MPLNET) web site mplnet.gsfc.nasa.gov (accessed February 2010).

U.S. Environmental Protection Agency (EPA) web site, Terms of Environment, www.epa.gov/OCEPAterms/aterms.html (accessed February 2009).

U.S. National Center Center For Biotechnology Information web site. www.ncbi.nlm.nih.gov/pmc/articles/PMC1240740/pdf/ehp0110-a00080.pdf (accessed June 2007).

University of Colorado at Boulder web site, Lidar Lectures, 2008. superlidar.colorado.edu/Classes/Lidar2007 (accessed January 2008).

Wagner, T., Beirle, S., Deutschmann, T., Grzegorski, M., Platt, U., 2008. Dependence of cloud properties derived from spectrally resolved satellite observations on surface temperature. Atmospheric Chemistry and Physics, 8, 2299-2312.

Whiteman, D.N., Demoz, B., Di Girolamo, P., Comer, J., Veselovskii, I.A., Evans, K., Wang, Z., Cadirola, M., Rush, K., Schwemmer, G., Gentry, B., Melfi, S.H., Mielke, S., Venable, D., Van Hove, T., 2006. Raman water vapor lidar measurements during the international H2O project: I. Instrumentation and analysis techniques. Journal of Atmospheric and Oceanic Technology, 23, 157-169.

Veselovskii I.A., Barchunov, B., 1999. Excimer laser based lidar for tropospheric ozone monitoring. Applied Physics, 68, 1131-1137.

Veselovskii, I.A., Cha, H.K., Kim, D.H., Choi, S.C., Lee, J. M., 2000. Raman lidar for the study of liquid water and water vapor in troposphere. Applied Physics, 71, 113-117.

Veselovskii, I.A., Dubovik, O., Kolgotin, A., Lapyonok, T., Di Girolamo, P., Summa, D.N., Whiteman, D., Tanré, D., 2009. Application of randomly oriented spheroids for retrieval of dust particle parameters from multi-wavelength lidar measurements, Proceedings of ISTP 8, S04-O10, 19-23 October 2009, Delft, The Netherlands.

Zhang, Y., Wu, S.-Y., Krishnan, S., Wang, K., Queen. A., Aneja, V.P., Arya, P., 2008. Modeling agricultural air quality: Current status, major challenges, and outlook. Atmospheric Environment, 42, 3218-3237.

APPENDIX A: REPRESENTATIVE AEROSOL PICTURES

Figure A.1. Satellite image shows the massive dust transport from Northwest Africa over Canary Islands to Northeast America.

Source: http://www.ncbi.nlm.nih.gov/pmc/articles/PMC1240740/pdf/ehp0110-a00080.pdf

Figure A.2. A red tide off the coast of Florida that killed thousands of fish and other organisms, may have been the result of a combination of waters full of the iron-loving bacterium *Trichodesmium* (right) and iron-rich dust from African deserts.
Source: http://celebrating200years.noaa.gov/transformations/habs/image1.html

Figure A.3. Satellite images of grassland wildfires in South California and the amount of aerosols emitted to the atmosphere.

Source: http://svs.gsfc.nasa.gov/vis/a000000/a002800/a002842

Figure A.4. Dust covered roads and cars after a rain including significant amounts of desert dust from Sahara, April 2010, South Eastern Turkey.

APPENDIX B: TECHNICAL DRAWINGS

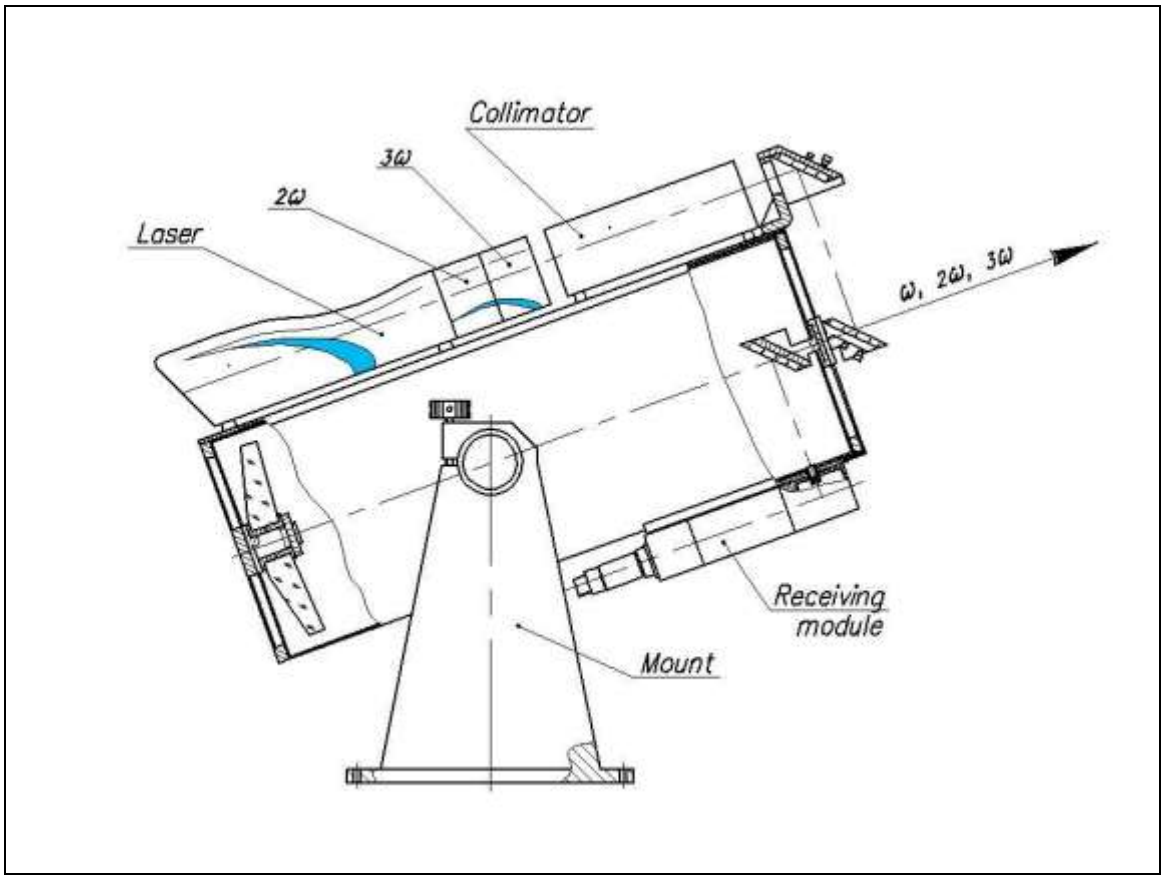

Figure B.1. Scheme of the transmitting and the receiving unit: Laser transmitter mounted on the receiver telescope.

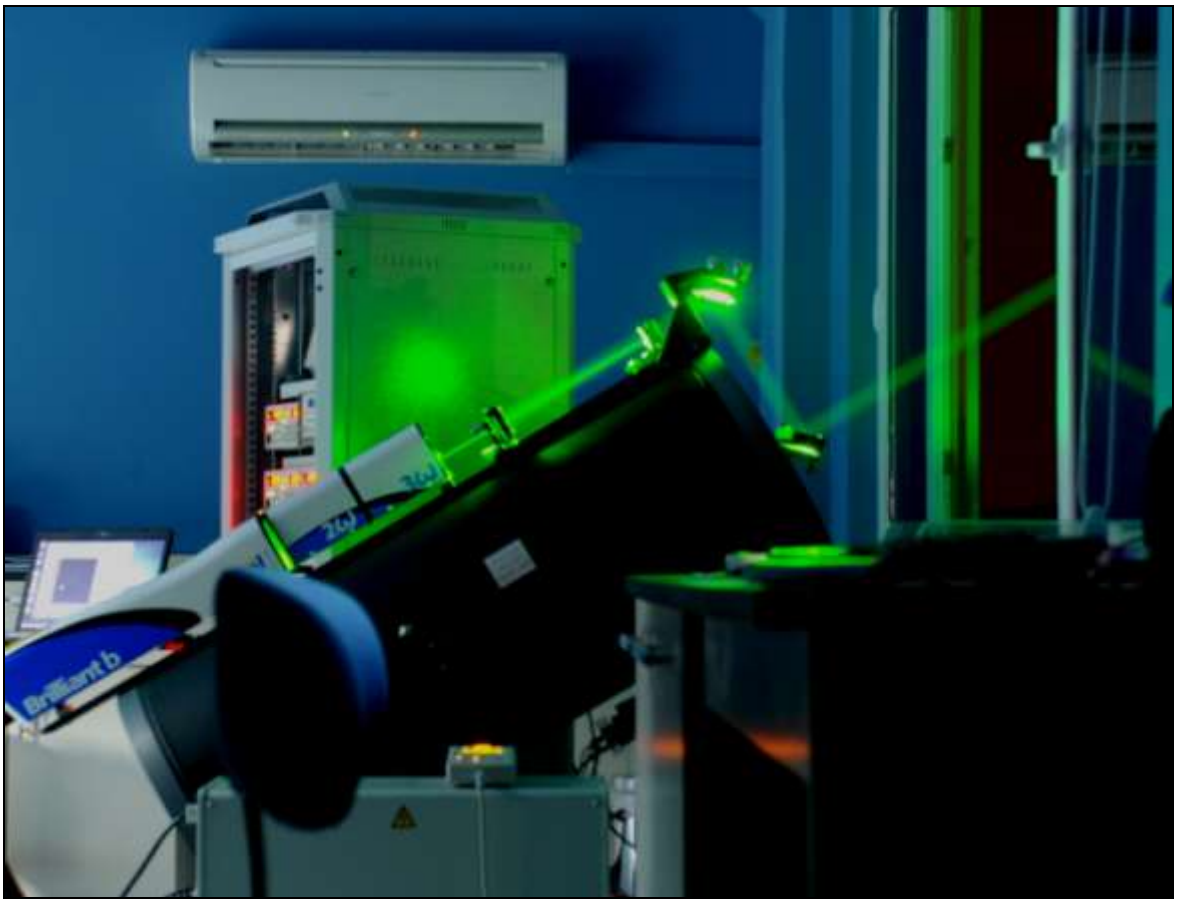

Figure B.2. The Multiwavelength Mie-Raman lidar system at TUBITAK MRC, Laser Spectroscopy Laboratory.

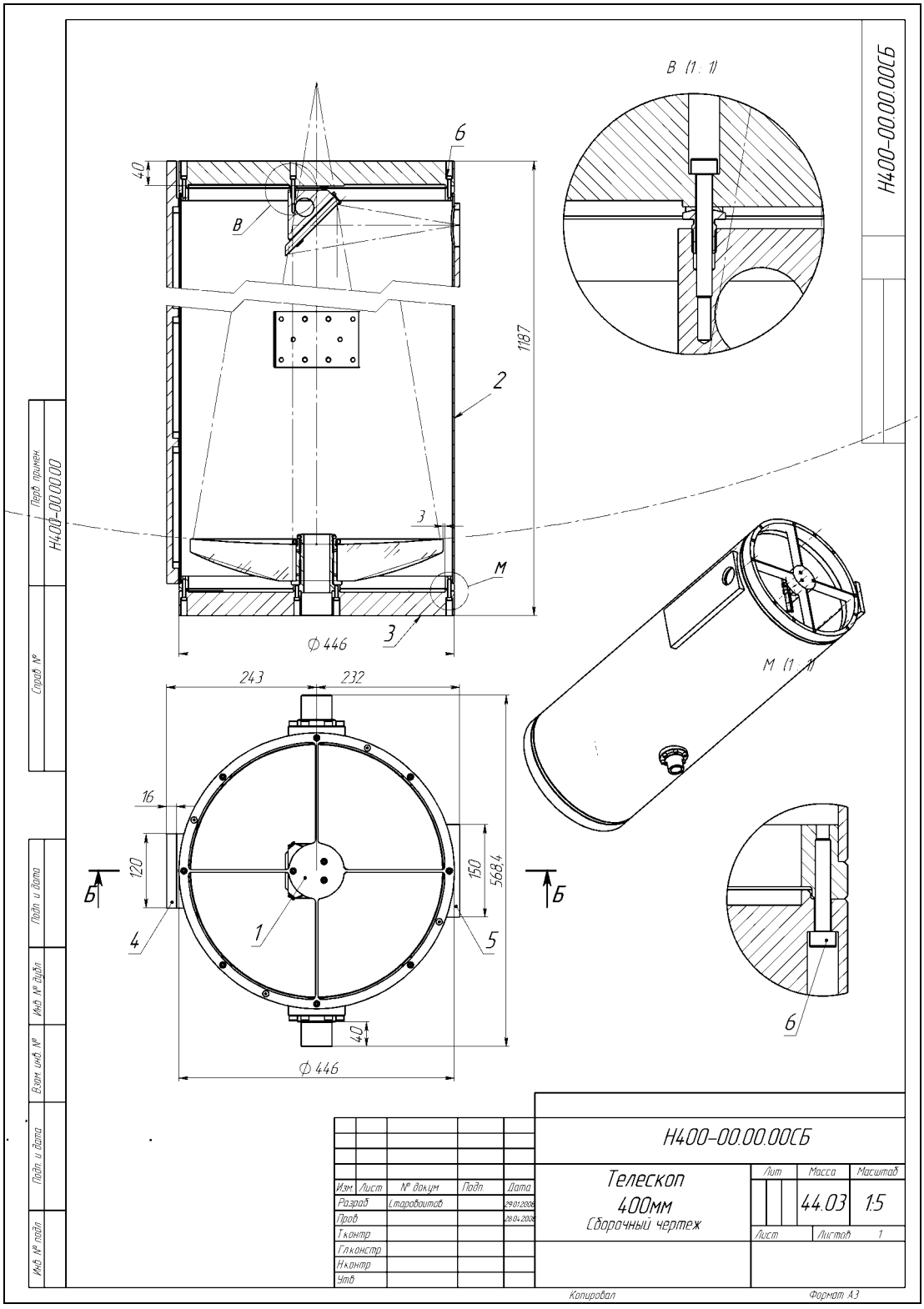

Figure B.3. Scheme of the telescope

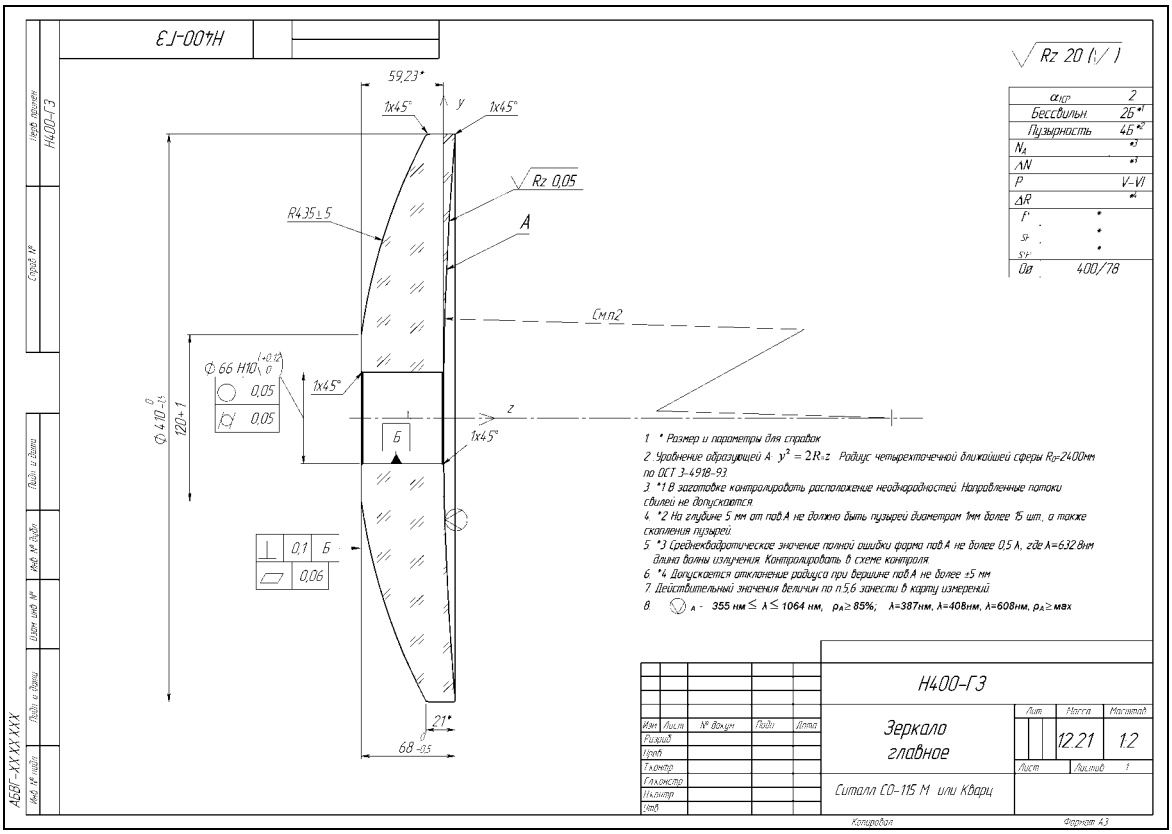

Figure B.4. Scheme of the main mirror of the telescope

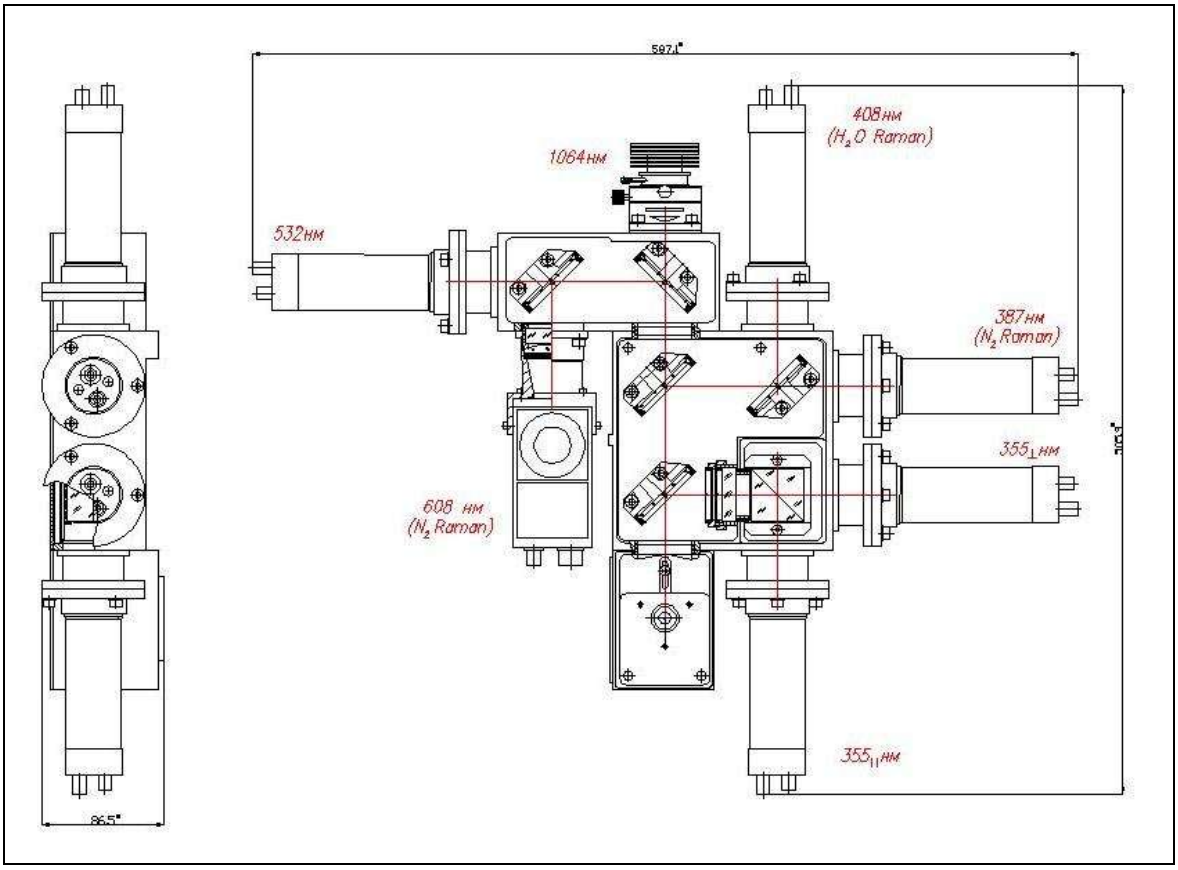

Figure B.5. Scheme of the spectrum analyzer

APPENDIX C : INSTALLATION PROCESS

Figure C.1. Assembling of laser harmonics

Figure C.2. Mounting the telescope

Figure C.3. Assembling the off axis collimator

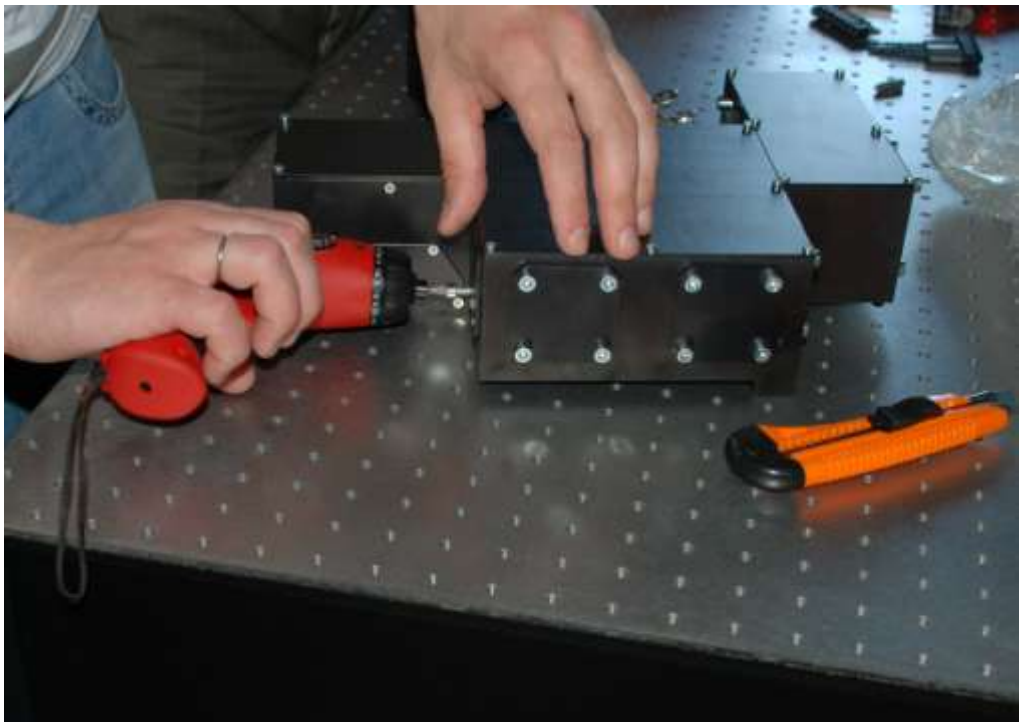

Figure C.4. Assembling the spectrum analyzer

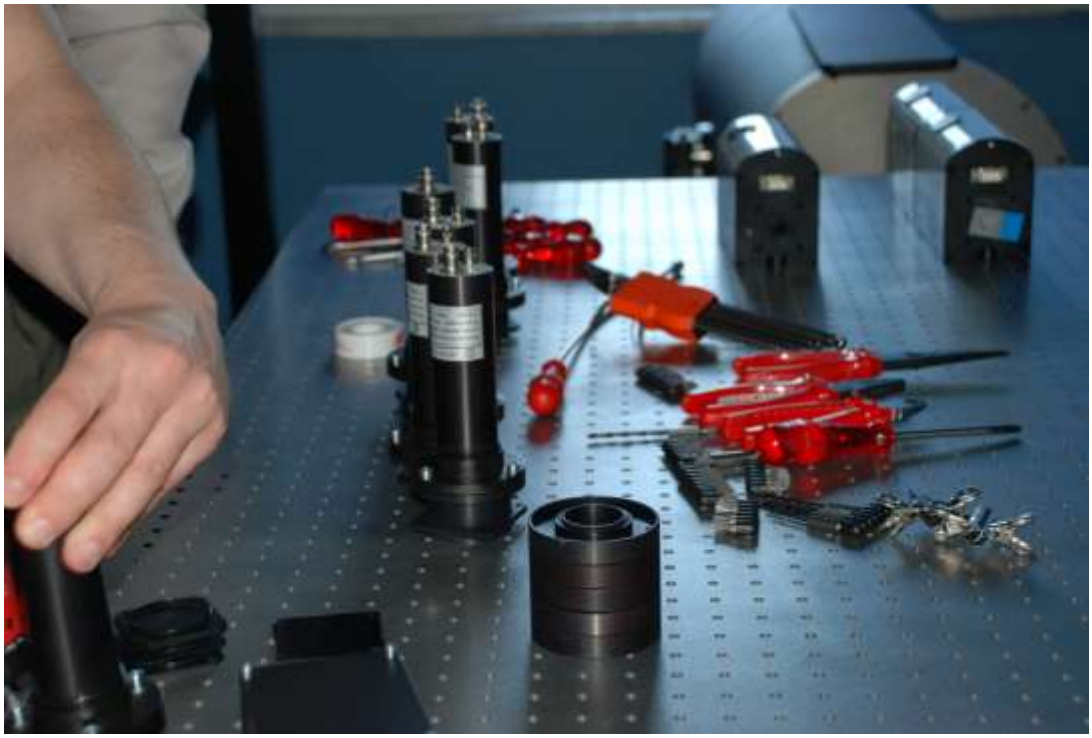

Figure C.5. Assembling the PMT's

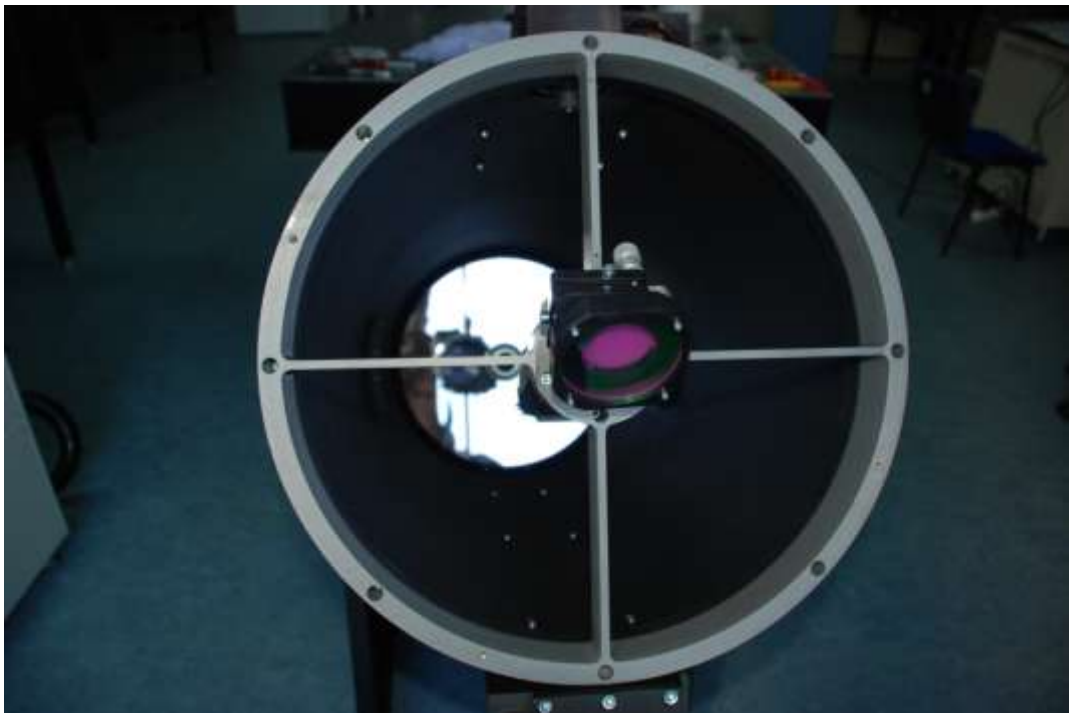

Figure C.6. Inside view of the the telescope

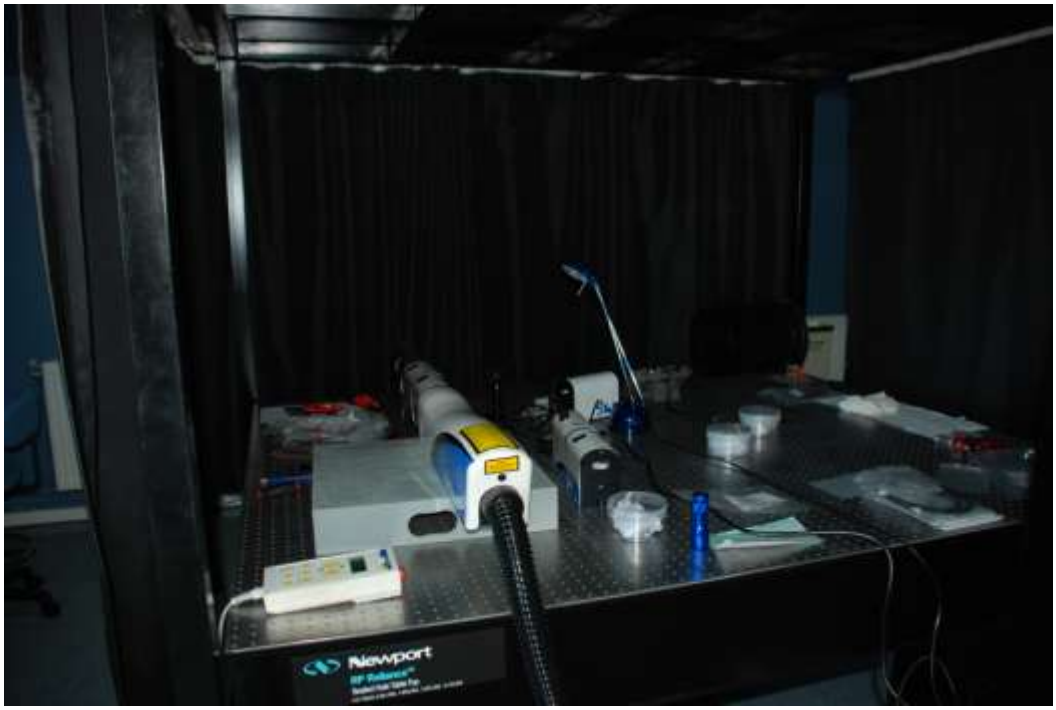

Figure C.7. Testing the laser alignment

Figure C.8. Testing the laser power

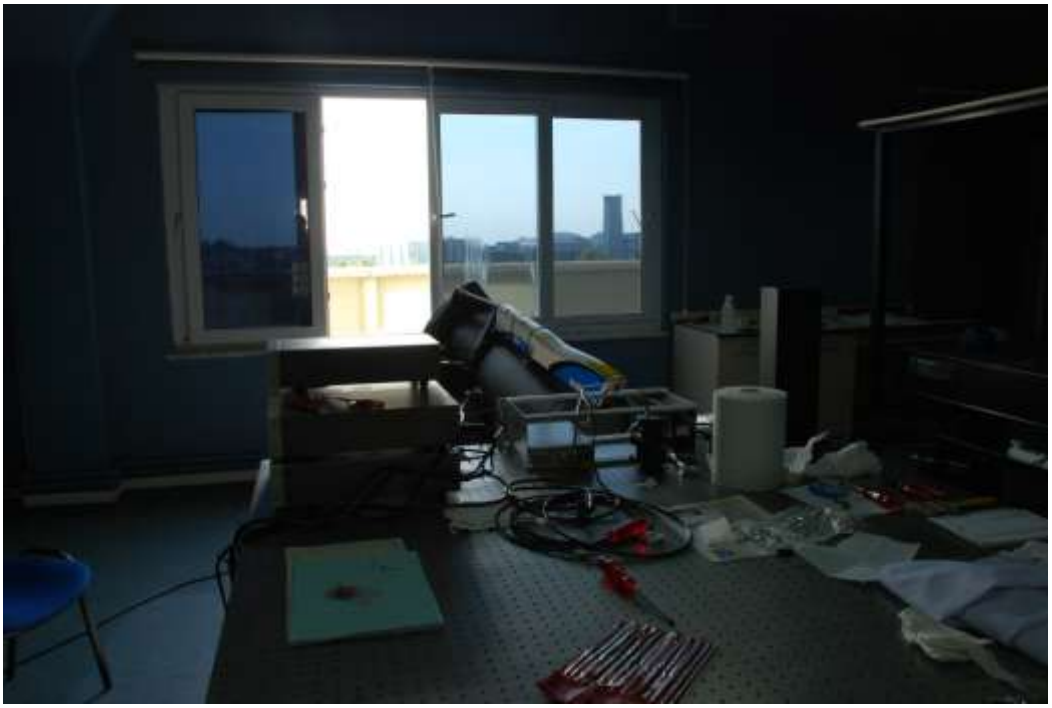

Figure C.9. Mounting the laser on the telescope

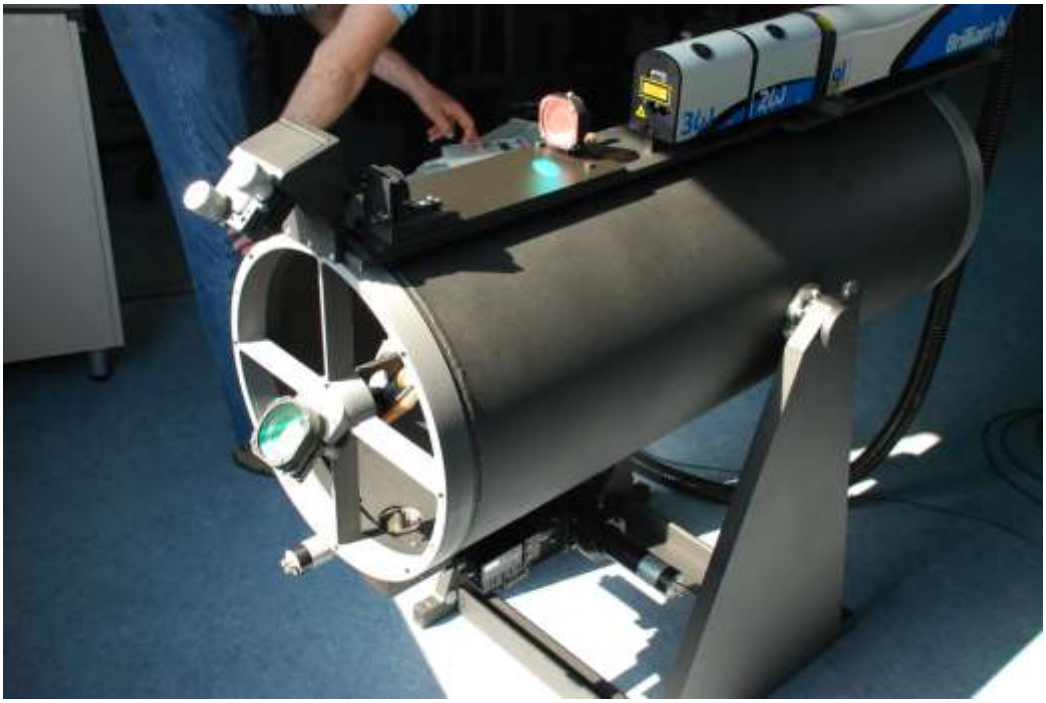

Figure C.10. Aligning the laser and the telescope

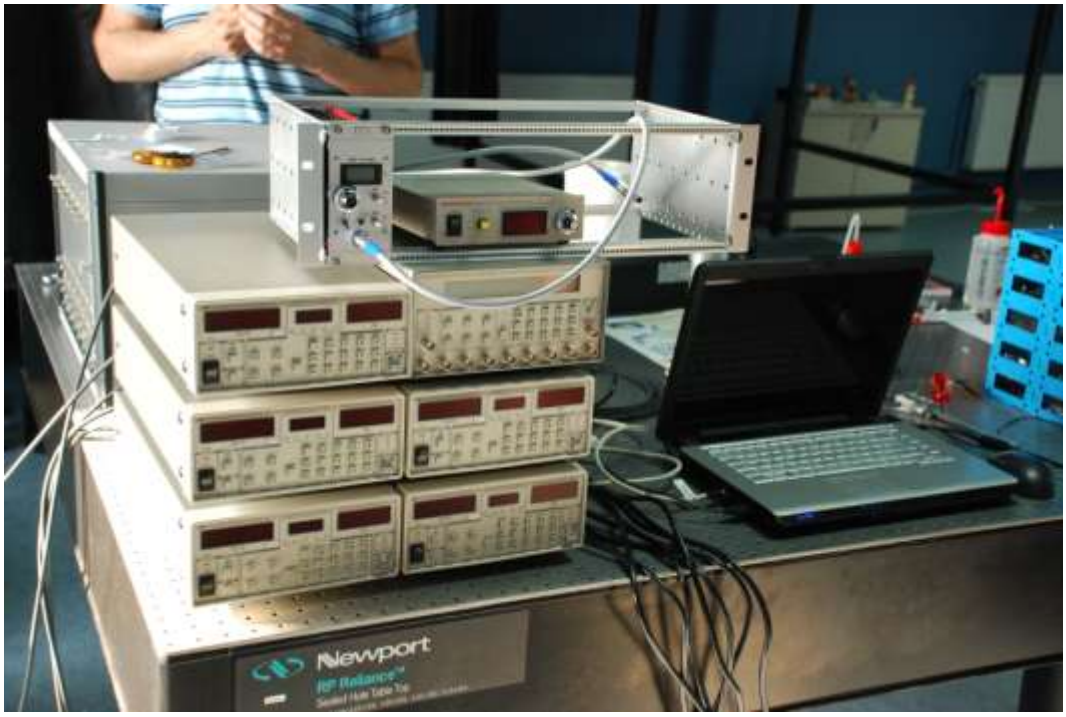

Figure C.11. Setting up the electronics

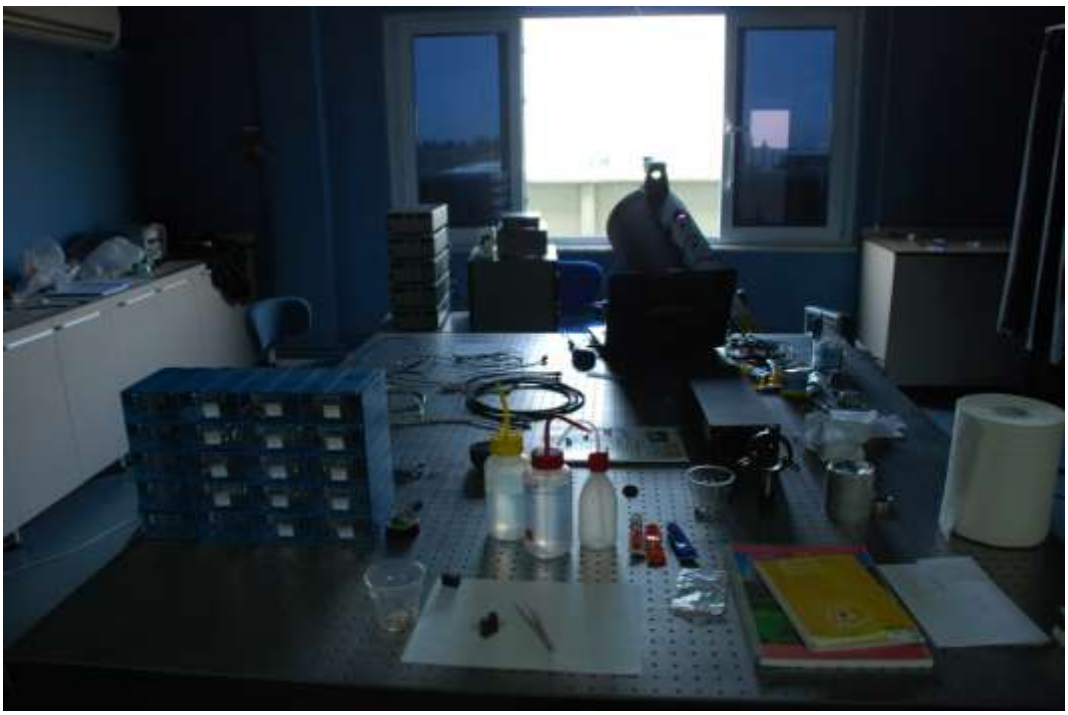

Figure C.12. First tests

Figure C.13. Testing the electronics

Figure C.14. First night tests

Figure C.15. Light of the lidar in operation out of the window

Figure C.16. The lidar system and the operator